Applications of embedded metamaterial-based electromagnetic-bandgap structures for dual-band devices and compact tunable bandstop filtering

by

Jacob A. Brown

A thesis submitted in partial fulfillment of the requirements for the degree of

Master of Science

in

Electromagnetics and Microwaves

Department of Electrical and Computer Engineering

University of Alberta

Abstract

While dual-band devices and filters are used for different applications, they each rely on a resonance mechanism. At high frequencies, where discrete lumped elements becomes unreliable, these resonances are introduced through electrical long transmission line (TL) segments. Metamaterials (MTMs), such as the negative-refractive-index transmission line (NRI-TL), can realize the same behavior while being directly embedded in a microstrip (MS) TL, thereby offering a high degree of miniaturization. A recently proposed MTM-based structure, known as the metamaterial-based electromagnetic bandgap structure (MTM-EBG), can realize many of the same dual-band and filtering properties, while being realized in a fully planar, fully printable and highly compact manner. The MTM-EBG relies on the interaction between a conventional right-handed MS-like mode and a left-handed coplanar waveguide (CPW)-like mode to realize a strong bandgap. This bandgap is predictable using multi-conductor transmission line (MTL) theory, and has consistent results with full-wave simulations. Here the MTM-EBG is analyzed for use in a fully embedded manner; this means that it can be directly inserted into an existing trace of MS, without occupying substantially more, if any, area. This fully embedded, uniplanar and printed device is used to develop a host of dual-band devices, including impedance transformers and power dividers. These are extended into the development of a dual-band corporate feed network, which can be easily augmented with dual-band radiating elements for a full dual-band antenna array. While developing these dual-band devices, it was identified that the MTM-EBG displayed a substantial amount of rejection given its diminutive footprint. These properties led to the development of a fully planar MTM-EBG-based MS bandstop filter, and the development of a new tuning mechanism perfectly suited to the MTM-EBG. By varying the position of a dielectric plate placed flush to the interdigitated capacitors of a fully printed MTM-EBG, the rejection band may be shifted by an amount proportional to the permittivity of the plate.

Preface

Parts of Chapter 3 have been published as Stuart Barth, Braden P. Smyth, **Jacob A. Brown** and Ashwin K. Iyer, "Theory and Design of Dual-Band Microstrip Networks Using Embedded Metamaterial-Based Electromagnetic Bandgap Structures (MTM-EBGs)," in press for the Special Issue on Recent Advancements in Metamaterials and Metasurfaces, *IEEE Trans. Antennas Propag.*, 2020 and **Jacob A. Brown**, Stuart Barth, Braden P. Smyth and Ashwin K. Iyer, "Dual-Band Microstrip Corporate Feed Network Using an Embedded Metamaterial-Based EBG," *IEEE Trans. Antennas Propag.*, vol. 67, no. 11, pp. 7031–7039, 2019. In the former, the concept of using the MTM-EBG as an impedance transformer was suggested by my supervisor, Dr. Ashwin K. Iyer, while I was responsible for the design, simulation and fabrication of the dual-band impedance transformer. In the latter, the concept of using the MTM-EBG as a constituent element of an N:1 corporate feed network was suggested by my supervisor, Dr. Ashwin K. Iyer, my co-authors acted in a purely supervisory role and I was responsible for all the design, simulation and fabrication discussed in the paper. Parts of Chapter 4 are currently under review in the *IEEE Trans. Microw. Theory Techn.*.

Acknowledgements

First I would like to thank my supervisor, Dr. Ashwin K. Iyer, for his aid and guidance in my research. It was through him that I first stepped into the academic world, where I started researching applications of transmission line metamaterials for miniaturzation of broadband antennas. It would later shift to applications in dual-band devices and embedded filters. Without Dr. Iyer's recommendations, I do not know where my research would have ended up. He has always provided meaningful direction, and through insightful questions has never failed to lead me to the answers I didn't know I was looking for.

I would next like to thank my colleagues and fellow researchers Stuart Barth, Braden Smyth, and Mitchell Semple for stimulating discussions leading to the realization of many of the devices presented in this work and the aid they have provided. I would also like to recognize Dr. Sanghamitro Das, Chris Barker, Elham Baladi and David Sawyer for their assistance.

My parents, Robert and Anita Brown, have been supportive of me during this entire process. Even though they didn't entirely understand the scope or nature of my research, they always offered their support and were always eager to brag about me.

Finally, I would like to thank my wonderful and supportive partner, Kelsey Lonergan, for her endless patience in this process. When I was starting my masters under Dr. Iyer, she was starting a new job as a nurse and had all the anxiety of starting this new job. In spite of this, she has been understanding of the commitment and has always been willing to listen to rants as I endeavored to solve the various challenges that arose during this academic process. Without her, I do not think I would have had the success I did in my masters.

Contents

List of Tables

List of Figures

List of Symbols

BW_m Average ABW over the tuning range.

C Shunt Capacitance of the MTM-EBG.

L Series inductance of the MTM-EBG.

L_p Length of the dielectric plate.

L_t Taper length.

L_{int} Length of MS TL between two T-junctions.

N Filter-order.

R_1 Return-loss level on the lower bandedge of a finite number of MTM-EBGs.

R_2 Return-loss level on the upper bandedge of a finite number of MTM-EBGs.

W Total width of a CBCPW or MTM-EBG.

W_p Width of the dielectric plate.

X Displacement of the dielectric plate.

Z_B Bloch Impedance of the MTM-EBG.

$[A]$ Top-left block matrix of the full MTM-EBG chain matrix.

$[Y]$ Per-unit admittance matrix.

$[Z]$ Per-unit impedance matrix.

$[Z_c]$ Terminal-domain characteristic impedance matrix.

$[\gamma]$ Terminal-domain propagation matrix.

$\%T_r$ Percent tuning range.

$\%\Delta$ Variation in the ABW over the tuning range.

$\Delta\phi_{ij}$ Phase error between ports i and j.

αd Attenuation.

$\bar{I}(z)$ Terminal-domain Current vector.

$\bar{V}(z)$ Terminal-domain Voltage vector.

βd Dispersion Phase.

ϵ Permittivity.

ϵ_p Permittivity of the dielectric plate.

λ_0 Free-space wavelength.

λ_g Guided wavelength.

μ Permeability.

θ Angle of a T-junction notch.

a Largest dimension of a T-junction notch.

d Length of the MTM-EBG.

d_p Antenna Array Spacing.

d_y, d_{y1}, d_{y2} Perforation offsets of the dielectric plate perforations.

f_1 First 90° frequency.

f_X X-point frequency.

f_2 Second 90° frequency.

f_Γ Γ-point frequency.

g Gap width of a CBCPW.

h Substrate thickness of the MTM-EBG host medium.

h_p Thickness of the dielectric plate.

l_c Total length of an interdigitated capacitor.

l_f Input length of MS TL.

l_i, l_1, l_2, l_3 Intermediate lengths of MS TL.

l_m Asymmetric taper at the input of an MTM-EBG.

l_n Length of the dielectric plate notch.

l_p Short taper at the input of an MTM-EBG.

l_t Interdigitated finger length.

p, p_1, p_2, p_3 Periods of the dielectric plate perforations.

r Diameter of dielectric perforations.

r_b Radius of bend.

s, s_1, s_2 Strip width of a CBCPW.

t Minimum feature size. Generally, interdigitated capacitor width.

t_g Wider capacitor gap width.

w_n Width of the dielectric plate notch.

w_t Interdigitated finger width.

w_{100} Width of a 100 Ω MS TL.

w_{50} Width of a 50 Ω MS TL.

w_i Strip Inductor width.

x_h, x_{h1}, x_{h2}, x_{l1}, x_{l2}, x_1, x_2, x_3 Insets of the dielectric plate perforation.

List of Abbreviations

ABW Absolute Bandwidth.

CBCPW Conductor-backed Coplanar Waveguide.

CPW Coplanar Waveguide.

CSL Coupled Slotline.

EBG Electromagnetic Bandgap Structure.

FBW Fractional Bandwidth.

MEMS Micro-Electro-Mechanical System.

MS Microstrip.

MTL Multi-Conductor Transmission Line.

MTM Metamaterial.

MTM-EBG Metamaterial-based Electromagnetic Bandgap Structure.

NRI-TL Negative-Refractive-Index Transmission Line.

PIM Passive intermodulation.

PPW Parallel Plate Waveguide.

RLGC Per-Unit-Length Resistance-Inductance-Conductance-Capacitance.

SIW Substate Integrated Waveguide.

TEM Transverse Electromagnetic.

TL Transmission Line.

Chapter 1

Introduction

1.1 Motivation

Dual-band devices and filters rely on resonant features to realize their properties. With the exception of discrete lumped-element designs, these resonances are typically introduced through electrically large features, such as quarter-wavelength segments. As necessary components for these devices, they increase the footprint and make them difficult to integrate into devices demanding compactness. Metamaterials (MTMs) are periodic arrangements of reactive elements that have properties not easily found in natural materials. While these are not always characterized on the basis of resonances, the dispersive properties they exhibit may be engineered for both dual-band and filtering applications. Additionally, due to their particular operating mechanism, they may be directly embedded within the host transmission line (TL) offering additional compactness [1]. These do have a drawback in that many TL MTM implementations require multiple layers or vias, which necessitate a more complicated fabrication procedure.

The metamaterial-based electromagnetic bandgap structure (MTM-EBG) is a device that was recently proposed as a uni-planar technology to suppress parallel-plate noise introduced by vias in multi-layer circuits [2,3]. Modelled as a multi-conductor transmission line (MTL),

this device combines the compact nature of TL MTM with the ability of electromagnetic bandgap structures (EBGs) to create predictable bandgaps. Since the initial development of the MTM-EBG it was identified that the MTM-EBG has certain properties well suited for dual-/multi-band operation and has been used in the development of a host of dual-band devices. One method exploits the presence of the bandgap to suppress signal flow on a given path, while permitting it to flow on another [4–8]. This technique has been demonstrated to be both flexible, reliable and relatively easy to implement; devices employing this mechanism require additional area to incorporate these additional paths and require a larger footprint.

It was demonstrated in [8, 9] that the phase properties of the MTM-EBG could also be exploited when embedded within a microstrip (MS) TL, effectively rendering the MS dual-band with highly predictable properties. This application was expanded to incorporate the embedded MTM-EBG into a standard impedance transformer allowing compact dual-band operation with performance comparable to conventional single frequency transformers. Further investigation revealed that the embedded MTM-EBG has a highly predictable and flexible rejection band, suggesting it is well suited to compact bandstop filtering applications [10].

This thesis represents a contribution to the development of dual-band MTM devices and compact MTM filters through the analysis and application of embedded MTM-EBG, which occupies no more area than a conventional MS TL. These components are modelled with relative ease by employing a combination of MTL theory and periodic analysis, and display behavior that is well captured with only a single unit cell in full-wave simulations. Due to impedance and coupling effects between individual connected cells, additional unit cells can be employed to improve the bandstop rejection and modified to enhance the passband performance. These components can then be made tunable through a novel mechanical planar tuning system, which is only possible due to the planar and fully printed nature of

the MTM-EBG.

1.2 Background

1.2.1 Theory

Conventional TL theory is limited in that it can only model the propagation of a single transverse electromagnetic (TEM) mode confined between two conductors. When an additional conductor is in close proximity, this model begins to break down as the field distribution is disturbed from that of the assumed propagating mode [11]. MTL theory bridges this gap by permitting a wide spectrum of modes to exist within a system with an arbitrary number of conductors. This extension shares a number of similarities with conventional TL theory: first, only TEM modes are modelled; second, the propagation can again be modelled as discretized per-unit-length resistance-inductance-conductance-capacitance (RLGC) components. In a MTL these RLGC components are incorporated in the model as *matrices* instead of *scalar* values [12].

This distinction introduces a number of complications related to MTL devices, the most prominent of which is the necessity for two transformation matrices. These matrices are introduced due to the general non-commutability and non-diagonality of the per-unit impedance ($[Z]$) and admittance ($[Y]$) matrices; this is shown in (1.1) and (1.2), which are the MTL voltage and current forms of the well known telegrapher's equation.

$$\frac{\partial^2}{\partial z^2}\vec{V}(z) = [Z][Y]\vec{V}(z) \qquad (1.1) \qquad\qquad \frac{\partial^2}{\partial z^2}\vec{I}(z) = [Y][Z]\vec{I}(z) \qquad (1.2)$$

These equations can be solved simultaneously by applying diagonalization matrices to each of (1.1) and (1.2). This transforms $[Z][Y]$ and $[Y][Z]$ into an identical and *diagonal* matrix γ^2; alternatively, this may be viewed as transforming (1.1) and (1.2) from the **terminal** domain, where the voltage and current vectors are defined for each unique *conductor*, to the **modal** domain, where the voltage and current vectors are instead defined for each unique *propagating mode*. It is a widely accepted fact that all of the terminal domain properties are unique while only the modal domain propagation constant is accepted as unique. The modal characteristic impedance, on the other hand, is generally considered to be non-unique [13]. This arises from the requirement of these diagonalization matrices, which differ in (1.1) and (1.2). These diagonalization matrices cancel out when solving for the propagation matrix, but carry over when solving for the characteristic impedance of the MTL. Due to an arbitrary scale factor that may be incorporated in these transformation matrices, it will generally result in a modal characteristic impedance that is not unique. In spite of the challenges associated with characterizing the modal domain characteristics of MTLs, they remain a helpful tool to characterize and analyze more complicated TL devices.

Similar to the transmission matrix of a two-conductor TL circuit element, the chain matrix exists for MTL circuits with two ports but an arbitrary number of conductors. For an arbitrary length l of MTL, the corresponding chain matrix is provided in (1.3) [12].

$$[T] = \begin{bmatrix} \cosh\left([\gamma]l\right) & \sinh\left([\gamma]l\right)[Z_c] \\ [Z_c]^{-1}\sinh\left([\gamma]l\right) & [Z_c]^{-1}\cosh\left([\gamma]l\right)[Z_c] \end{bmatrix} \qquad (1.3)$$

An alternate form of this matrix may be found in [12], but depends on the *current* transformation matrix, instead of the *voltage* transformation matrix. This chain matrix shares a number of the same properties as the transmission matrix. For starters, it can be used to easily model a cascade of arbitrary circuit elements through multiplication of their constituent chain matrices.

Periodic Structures

The analysis of periodic structures is critical to modern understanding of both MTMs and EBGs. Some early research and applications into periodic structures focused on miniaturizing antennas, or enhancing other antenna properties with periodic dielectric arrangements [14–16]. The host media in these designs were filled with periodic arrangements of holes or metallic regions, allowing for precise control over the effective permittivity and permeability, and to suppress the propagation of certain modes. This extends itself naturally to TL structures as they are more easily modelled and realized on conventional substrates [1].

The properties of an infinitely periodic structure can be determined from the properties of a single period, or unit cell. This is known as Bloch (or *Floquet*) analysis, and is critical in the understanding and analysis of periodic structures. The Bloch analysis technique relies on applying a periodic boundary condition to the terminals of the constituent unit cell; this is provided in (1.4) where n is terminal reference number, γ is the propagation constant of the relevant Bloch mode and d is the period (or length) of the individual unit cells.

$$\begin{bmatrix} V_{n+1} \\ I_{n+1} \end{bmatrix} = \begin{bmatrix} V_n \\ I_n \end{bmatrix} e^{-\gamma d} \tag{1.4}$$

This condition restricts the change in voltage and current across an individual unit cell to a scaled version of the input voltage and current. It is apparent in (1.4) that this condition preserves the voltage and current distribution associated with a given *Bloch* mode of the system, which suggests that $e^{-\gamma d}$ is an eigenmode of the unit cell. By modelling the unit cell of this structure as a transmission matrix, which directly relates the voltage and currents of the input port to the output by definition, the corresponding Bloch modes can be derived with relative ease. For a two conductor TL the dispersion diagram defining the Bloch modes can then be solved using (1.5); the solutions of which can be found with the quadratic equation:

$$\begin{aligned} \det\left|\begin{bmatrix} A & B \\ C & D \end{bmatrix} - \begin{bmatrix} e^{-\gamma d} & 0 \\ 0 & e^{-\gamma d} \end{bmatrix}\right| &= 0 \\ e^{-2\gamma d} + (A-D)e^{-\gamma d} + AD - BC &= 0 \end{aligned} \tag{1.5}$$

The periodic boundary conditions from (1.4) are relatively easy to derive for a MTL by replacing the scalar voltages and currents with column vectors representing terminal voltages and currents. This has been demonstrated in previous works, such as [2, 3, 17–19]. While it is simple to derive the periodic boundary conditions, it is often not practical to derive a closed form solution. In [17, 18], a shielded sievenpiper mushroom was modelled as a MTL supporting multiple parallel plate waveguide (PPW) modes. Since these modes may be modeled as isolated PPW modes, closed form solutions could be derived for the X- ($\beta d = \pi$) and Γ- ($\beta d = 0$) points. More complicated structures, such as the UC-EBG [20], are not so easily modelled.

The Bloch modes supported by periodic structures have a characteristic impedance, known

as a *Bloch impedance*, that typically differs from that of the host media; this is particularly true when the periodic structure has forbidden propagating bands [21–23]. Outside of these bands, the Bloch impedance is usually real and closely approximated by the characteristic impedance of the host, but can vary due the dispersiveness of these passbands and additional loss. Within these stopbands, however, the Bloch impedance becomes large and imaginary as propagation is forbidden.

1.2.2 Technology

Metamaterials

By periodically arranging discrete features, such as electrically thin wires [24], or open-looped resonators [25], the Bloch modes of the structure can display properties that differ substantially from that of the host media. Under the assumption that the period of these arrangements is highly sub-wavelength, these structures can be viewed as an effective material. This distinction makes it appropriate to refer to these periodic structures as MTMs, or artifical materials. One example was discussed previously [16], but MTMs can be designed with more extreme properties such as large permeabilities (μ) without ferrites [25], negative values of μ [26] and negative permittivities (ϵ) [24].

Combining these effects can similarly yield interesting and useful properties; for example, simultaneously negative ϵ and μ are one of the requirements for a *left-handed* medium, as proposed by Veselago [27]. Such a medium supports a *backwards* wave propagation in which the group and phase velocities are contra-directed from one another. For RF and microwave frequencies this effective medium can be realized with sufficiently sub-wavelength periodic arrangements of reactive elements; a periodicity of less than $\lambda/10$ is sufficient to treat the

structure as a microwave material. MTMs have been designed to interact with a variety of 3D structures, such as waveguides and plane waves, which is critical for applications in sub-diffraction imaging [28, 29] or electromagnetic cloaking [30]. Example MTM devices are shown in Figs. 1.1(a) and 1.1(b).

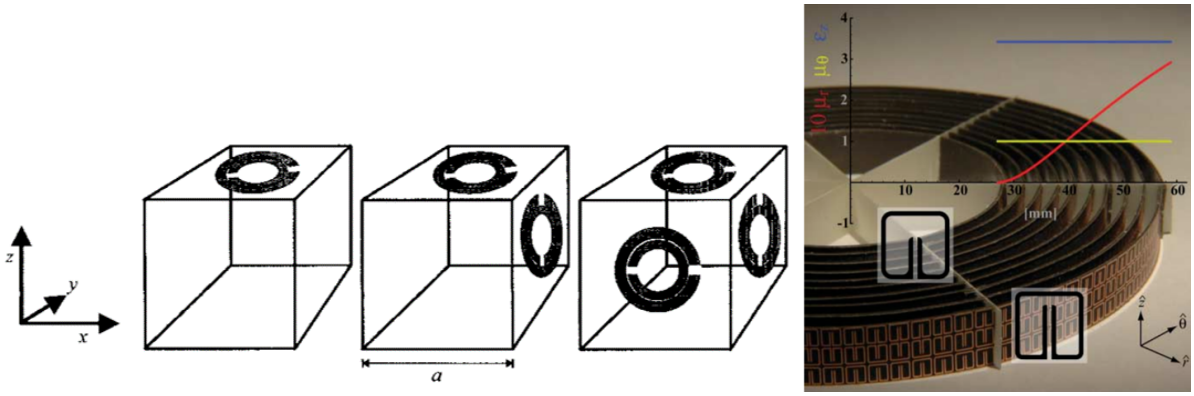

(a) (b)

Figure 1.1: Example MTM realizations: a) Isotropic magnetic material and b) 2D MTM cloak. Taken from [26] and [30] respectively.

MTM concepts can similarly be applied to TL structures, and result in similar properties. One such structure is known as the negative-refractive-index transmission line (NRI-TL), which realizes a simultaneously negative ϵ and μ through a periodic arrangement of shunt inductors and capacitors [1]; this may also be referred to as a composite left/right-handed material [31]. The behavior of the NRI-TL is well modelled on the basis of periodic structures, and as such, has many predictable properties beyond the super-lensing demonstrated in [29]. The backwards propagation region of these TL MTM can be used to design highly miniaturized phase shifters [32] and antennas [33, 34]. Some example TL MTM devices are shown in Figs. 1.2(a) and 1.2(b).

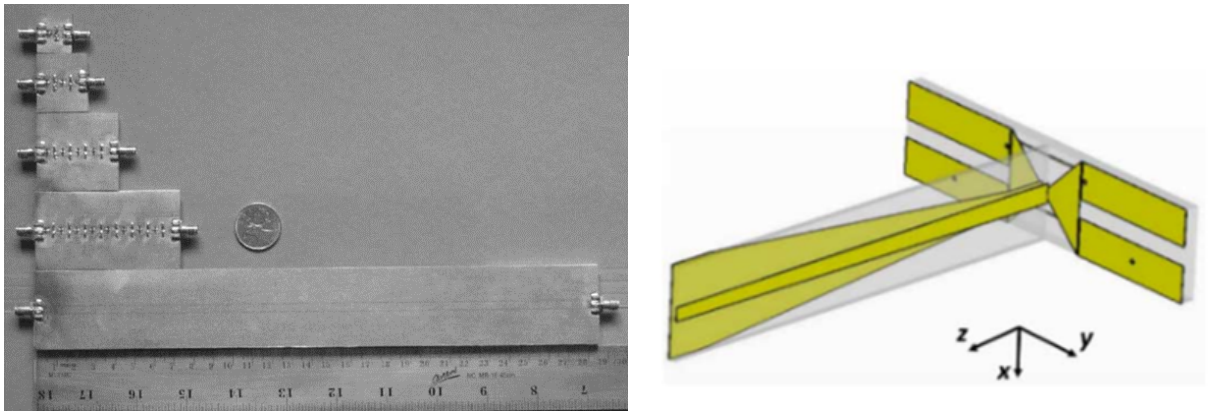

(a) (b)

Figure 1.2: Example TL MTM realizations: a) Compact 0° phase-shifters and b) MTM antenna. Taken from [32, 34] respectively.

Electromagnetic Bandgap Structures

EBGs are another common class of periodic structure. The properties of these structures are similar to that of MTMs and may be viewed as an extension of MTM technology; EBGs are typically more focused towards the suppression of select modes. A number of microwave EBGs have been proposed, such as the Sievenpiper mushroom [35], which was initially modelled as a high impedance surface for a surface wave, or the UC-PBG [20]. Due to their ability to selectively suppress the propagation of certain modes, variations of these structures have been investigated extensively for applications in mutual coupling suppression in closely spaced antenna arrays [20], compact guided wave structures [36,37] and suppression of PPW noise due to via interconnects [38, 39].

Depending on the EBG, they may be accurately modelled as MTL structures. This grants additional insight into the exact mechanism behind their respective bandgaps [17]; this has given rise to a different definition of a bandgap. A bandgap is formally defined as a region in which propagation is forbidden. The propagation characteristics of multi-modal structures make it practical to define the bandgap as a region in which two modes may simultaneously propagate and attenuate (i.e. as *complex* modes), which in some cases implies a rapid transfer

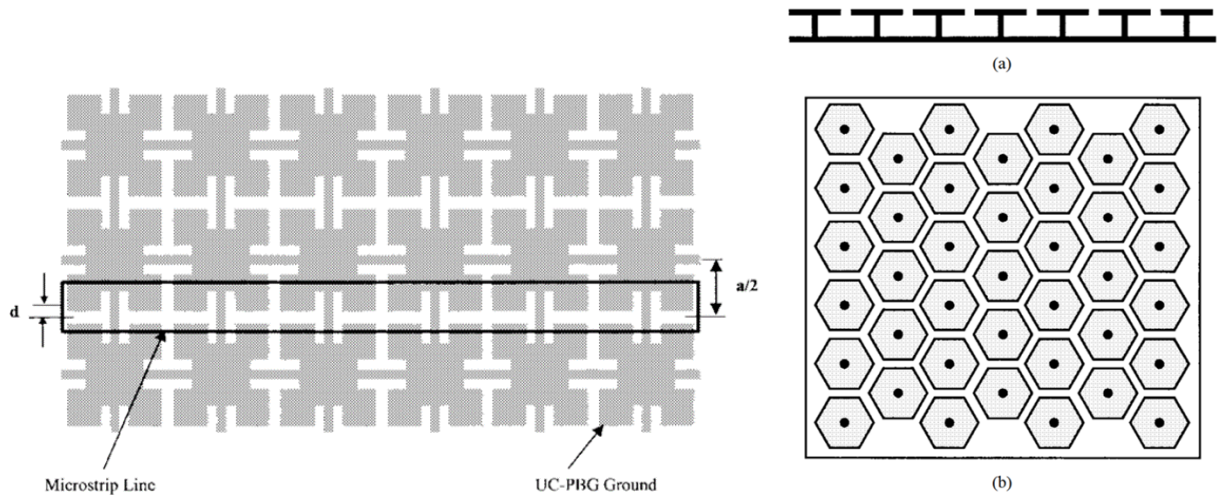

(a) (b)

Figure 1.3: Example EBGs: a) UC-EBG and b) Sievenpiper mushroom. Taken from [20, 35] respectively.

of power from one mode to another. In these multi-modal structures, there may be multiple regions where propagation is forbidden, but these may not be formal bandgaps per the MTL definition.

1.2.3 Applications

Dual-Band Devices

Dual-/multi-band devices are microwave and RF components that are capable of operating simultaneously at two generally arbitrarily spaced frequencies. Due to the increasing saturation of the telecommunication spectrum, dual-/multi-band devices can improve the functionality by permitting simultaneous performance across multiple transmission/receiving bands while minimizing the overall footprint. Under normal conditions at higher frequencies, a device is restricted to a single operating frequency defined. A simple example of the cause of this is a quarter-wavelength TL segment, which with careful selection of the impedance,

can convert one real impedance into another. This relatively simple component is used in T-junction power dividers, Wilkinson power dividers, quadrature hybrid couplers and rat-race couplers. Due to the dependence on a quarter-wavelength response, the impedance transformer is inherently limited to a narrowband response centered around a single frequency and subsequent odd harmonic frequencies. The bandwidth can be improved by cascading additional segments, but contributes additional loss due to the increasing reliance on resonant features [40].

Through a similar modification of additional segments, but under marginally different conditions, multi-section TL components can be viewed as dual-band TL [41]. By cascading two TL segments, which are generally less than a quarter-wavelength, dual-band performance could be achieved at generally arbitrary frequencies. As this is once again reliant on additional length, it introduces additional loss while being electrically large. If the electrical size of the dual-band components is too large, it may be more practical to use multiple single-frequency components. Such a constraint has prompted the development of a number of compact, dual-/multi band devices [42–59].

These devices enable dual-band properties by relying on resonant features to alter the phase response of the constituent TL while maintaining a compact device. Many of these devices also display a stopband filtering response, but the dual-band operating frequencies are typically displaced from this band. LC resonators have been used extensively, particularly at lower frequencies, and are more easily extended to multi-band devices [49, 52, 58, 59]. However, since these devices are ultimately limited to the availability of precise loading values and the low Q values of the lumped elements, fully printed dual-band solutions have also been investigated. TL segments with open or short circuit stubs have been extensively investigated for dual- and multi-band band applications due to their ease of modelling and design [42–45, 48, 50, 54, 56]. Several alternate options for realizing these responses exist, such

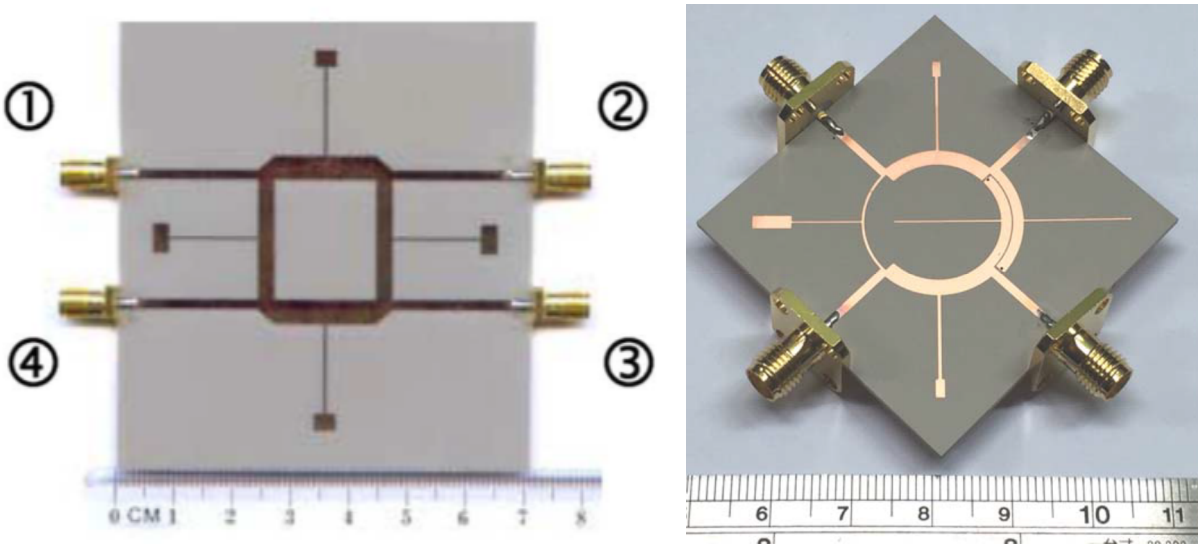

(a) (b)

Figure 1.4: Example devices: a) Dual-band quadrature coupled hybrid and b) Dual-band rat-race coupler. Figures taken from [45, 53] respectively.

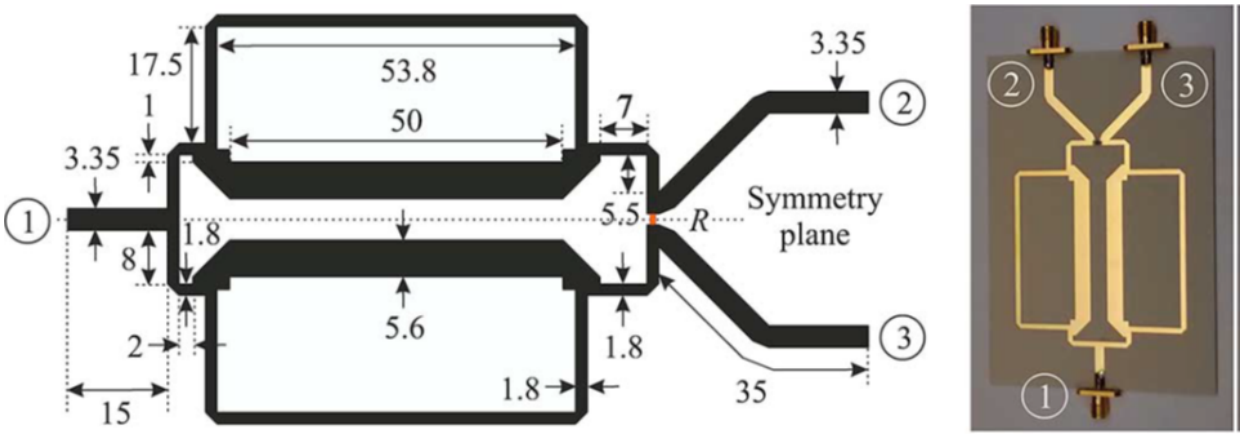

Figure 1.5: Example multi-band Wilkinson power divider. Figure taken from [55].

as open-/short-circuit coupled-line segments with stubs [47, 53], signal interference [55] and port-extension topologies [46, 51]. Some example dual-band devices are provided in Fig. 1.4 and a multi-band device is shown in Fig. 1.5. While these techniques are highly practical and generally easy to realize, many of them suffer from limits in the frequency ratios and impedances they may realize and may require vias to fully realize the desired properties.

Many of the aforementioned dual-band devices rely on resonant features to engineer the phase

response. This same engineering can be realized in a far more compact manner through the usage of TL MTMs. As such, variations of TL MTMs have been extensively investigated to realize strongly miniaturized dual-band devices [60–66]. While these structures are reliant on highly dispersive properties, which implies that the Bloch impedance varies substantially, careful selection and design of the constituent MTMs limits the divergence from the desired impedance values.

Embedded and Compact Filters

Modern bandpass and bandstop filters rely heavily on both resonant elements and coupling effects to exhibit their properties [67]. These resonances may be introduced through lumped elements, waveguide cavities, substate integrated waveguide (SIW) or even MS quarter-wavelength resonators. While they can be highly compact, lumped element resonators are limited to lower frequencies due to self-resonances, and very low quality factors. Higher frequency realizations require large features to meet the necessary resonant conditions; while some miniaturization can be achieved with the usage of high permittivity substrates, this is only an option for planar networks or in applications such as SIW filters. Waveguide filters, by necessity, are typically on the order of a wavelength. This can complicate the integration of such components into telecommunication systems, as well as substantially increase the necessary footprint of the devices.

MTM and EBGs have been used as embedded filters, owing to the highly predictable nature of their rejection bands, their ability to be embedded directly within an existing MS TL and their highly compact nature [68–72]. In [68–70], the filter unit cells are based on the NRI-TL and modified to appear as both a bandpass filter and a bandstop notch filter [1]. In [71], balanced composite right/left-handed line with complementary split-rings resonators placed

in the ground plane are embedded within a MS TL, thereby giving it broadband and compact bandpass behavior. In [72], the ground plane of a MS TL is etched with circular holes, yielding a broad bandstop filtering response. Even though these filters could be considered directly embedded in MS TLs, the resonant features required to achieve the desired response extend, often substantially, beyond the nominal width of the MS TL. Alternatively, these features may be added to the ground plane. The increased footprint of these filters may limit their usefulness in applications demanding compactness.

Tunable Filters

While fixed-frequency filters are practical, the requirements of modern telecommunication systems have made tunable filters more appealing as they can adapt to changing conditions in the frequency spectrum, such as sources of interference [73–77]. These filters are beneficial to such applications as they can substantially reduce the number of filters required by combining multiple individual filters into a single element. To render these devices tunable, they require a tuning mechanism that can not only be easily incorporated into the filter, but can also act on a large portion of the electromagnectic fields. For planar circuits, these tuning elements are typically designed to replace the capacitive element; the tuning may then be realized through either a varactor or a micro-electro-mechanical system (MEMS) capacitor. Both of these elements are tuned using an external electrostatic field and typically have very fast switching times.

Varactors are based on diodes which, as active devices, are inherently non-linear. This can introduce a number of complications at higher power levels, such as intermodulation that can drastically affect the performance of telecommunications system for levels as low as -140 dBc. While MEMS capacitors are viewed as nearly linear, they are much more complicated to

fabricate and realize [78]. A simpler mechanism involves mechanically changing an aspect of the resonator to alter the field profile. Often, 3D cavity resonators rely on mechanical tuning as highly subwavelength varactors or MEMS don't act on a sufficient portion of the electromagnetic fields. Mechanical tuning is slower than electrical tuning, but has none of the linearity issues associated with varactors while being substantially easier to realize.

Filters that can maintain a constant absolute bandwidth (ABW) are of particular interest as these filters have more consistent performance over their tuning ranges and are better suited to telecommunication systems where the operating bands are allocated to fixed frequency channels. Conventional filter theory suggests that full control over the ABW can be accomplished using $2N+1$ tuning elements where N is the filter order [78]. This set-up allows for both the coupling and resonating regions to be tuned, but is usually costly and difficult to implement [78]. In recent years, a significant amount of research has been carried out that aims to develop a filter that can maintain a constant ABW while minimizing the number of tuning elements [79–86]. These devices accomplish this behavior by engineering the coupling coefficient to be inversely proportional to frequency. Fully planar solutions to maintain constant ABW have been proposed, and typically employ electrically long or meandered lines to force the coupling coefficient to be inversely frequency dependent [79–83, 87]. Usually, these filters must be electrically large and have larger variation in ABW than cavity-based constant ABW filters, which have also been proposed [84–86]. These filters are mechanically tuned to more easily affect the electric and magnetic fields contained within the resonant cavity. While these cavity structures can maintain a nearly constant ABW with variations in the experimental ABW on the order of 1-2%, they are physically large, can be difficult to scale to both lower and higher frequency bands, and have complex features that can be challenging to fabricate. Some example tunable filters with constant ABW are shown in Figs. 1.6(a) and 1.6(b).

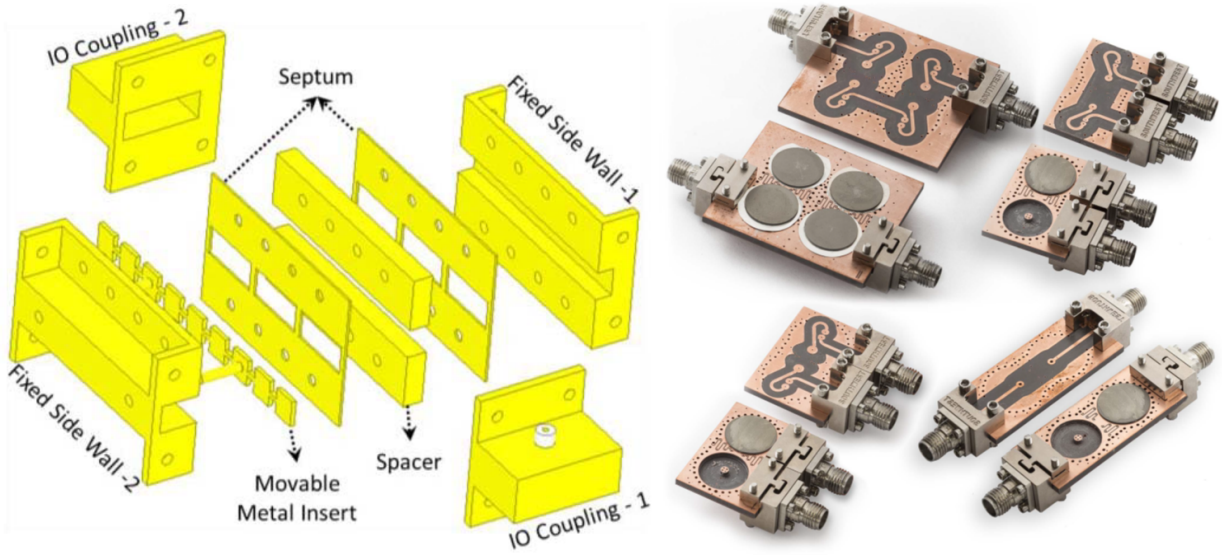

(a) (b)

Figure 1.6: Example filters with constant ABW: a) Waveguide bandpass filter [84] and b) SIW bandstop filter [86].

Several MTM-based frequency tunable filters have been proposed, such as [88, 89] but their properties tend to vary significantly as the loading capacitance is varied. For filters based on the NRI-TL, the stopband properties are related to the $\Gamma-$ and $X-$ point cutoff frequencies, and are dependent on *either* the inductive or capacitive loading of the cell. As such, the performance can change rather drastically as the capacitance is changed and leads to large variations in the bandwidth of the filter.

1.3 Thesis Layout and Contributions

Chapter 2 briefly discusses the theory of operation behind the MTM-EBG, particularly the analysis of modelling the MTM-EBG as a MTL equivalent circuit and briefly discusses the Bloch analysis. A discussion of the different configurations of the MTM-EBG, including suitable applications and advantages, follows the characterization of the MTM-EBG properties. Limitations to these configurations are also presented and a summary is provided

on a host of parametric studies performed using the equivalent circuit model. Properties of the MTM-EBG towards dual-band devices are discussed, and it is demonstrated that a single MTM-EBG is representative of the infinite cascade while having a predictable Bloch impedance. The effect of tuning the MTM-EBG on both the center frequency and bandwidth is discussed and verified using both the equivalent circuit model and closed form expressions. A mechanism to compensate for the change in bandwidth of the MTM-EBG as it is tuned is also presented. The effect of cascading multiple, symmetric unit cells is then examined and it is identified that poor passband performance may occur for a large number of cascaded cells; mechanisms to improve passband performance are then examined through parametric studies.

Chapter 3 discusses the design and implementation of an embedded MTM-EBG for use in designing a dual-band corporate feed network, ideal for exciting dual-band antenna arrays. An initial demonstration of the expected properties is provided in the form of a simple impedance transformer, which is later adapted for use in a T-junction power divider. This dual-band T-junction has improved performance compared to an unloaded network of identical size operating at the intermediate frequency. Comparing the embedded MTM-EBG to alternate dual-band devices found in recent literature reveals several distinct advantages over these devices; notable that the MTM-EBG may be substantially smaller and has a flexible phase response. The dual-band T-junction is then cascaded to form a dual-band corporate feed network suitable for use in dual-band antenna array applications. In this design process, a sensitivity to the MTM-EBG to asymmetric current distributions is identified and solutions to mitigate this are proposed.

Chapter 4 discusses two implementations of the MTM-EBG as a tunable embedded filter with constant ABW. The first is designed to validate the proposed tuning mechanism over a small range, and is tunable from 3.5 to 4.0 GHz. An initial fixed-frequency design is presented that

operates at 4.18 GHz with a 10-dB transmission ABW of 225 MHz. This is then made tunable by affixing a dielectric plate to the surface of the planar MTM-EBG and varying its position. Simulation and experimental results are presented and show generally good agreement. The second variation is a tunable filter designed to operate over the TV Whitespace frequency spectrum; specifically from 470 MHz to 700 MHz with a 10-dB transmission ABW of 35 MHz. Modifications owing to the increased range are discussed, and simulation results for the fixed-frequency design are demonstrated. Complications associated to the larger range are also discussed.

Chapter 5 discusses the major results and conclusions of each chapter. Based on these results, future works appropriate to each application are discussed and presented. These future works include multi-band embedded MTM-EBG unit cells, mm-wave applications, further characterization of the MTM-EBG as a filter element that may be then used in accordance with filter theory, and tunable MTM-EBG-based filters where the bandwidth is maintained by engineering the individual unit cells and not the tunable plate.

Chapter 2

Theory, Analysis and Properties

2.1 MTM-EBG Analysis

2.1.1 MTM-EBG Host Structure

The host medium of the MTM-EBG is formed by periodically loading a conductor-backed coplanar waveguide (CBCPW) (see Fig. 2.1) with shunt inductors and series capacitors as shown in Fig. 2.2. In a conventional coplanar waveguide (CPW) TL, this loading scheme would cause it to display backwards propagation; also know as left-handed propagation, it is reminiscent of the behavior observed for NRI-TL [1]. However, the CBCPW is more accurately modelled as a MTL which supports an pre-defined spectrum of quasi-TEM modes and models their related coupling effects. The modes of concern in this work are the MS-like, CPW-like and the coplanar stripline (CSL)-like modes. The MS- and CPW-like are characterized as being "even"-modes as they are symmetric along the transverse plane of symmetry; the field symmetry between these modes permit them to strongly couple to one another [2]. The CSL-like mode does not strongly couple to either of these modes; it may be excited by discontinuities in the CPW TL and is often suppressed using air bridges or grounding vias [90]. These methods to suppress the CSL may also affect the propagation

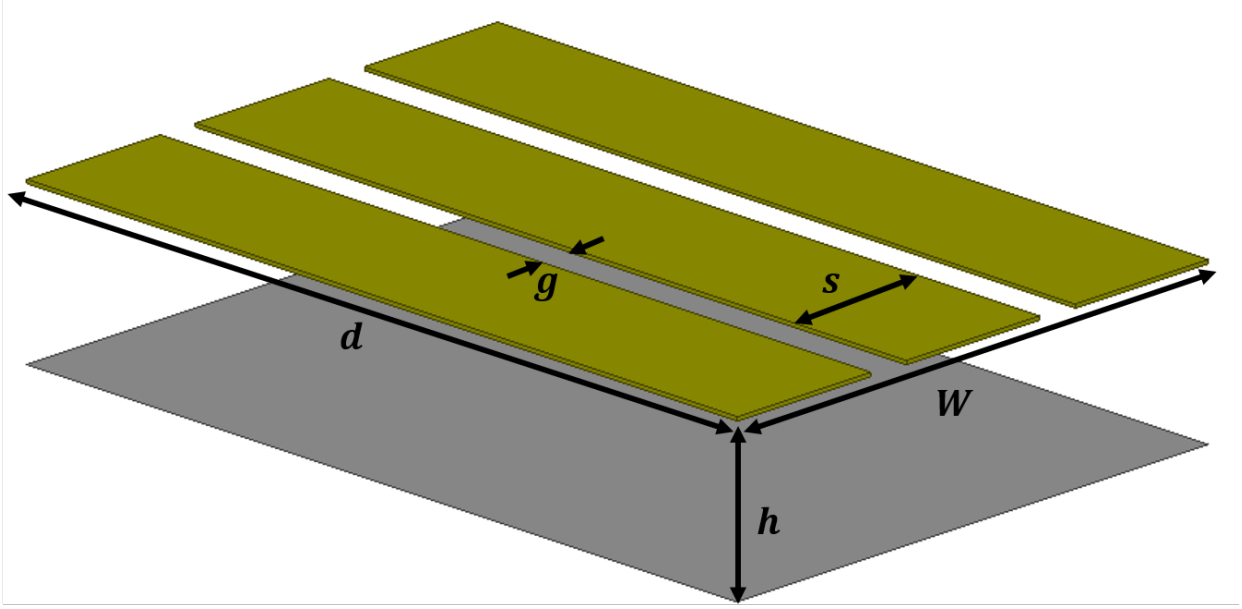

Figure 2.1: 3D layout of the MTM-EBG host conductor network, also known as a CBCPW. Relevant dimensions have been labelled.

of the MS-like mode which is necessary to the operation of the MTM-EBG. Generally, by exciting the MTM-EBG from an input MS TL only the even-modes will be excited; an exception to this is discussed in Chapter 3.

The loading of the MTM-EBG has minimal effect on the isolated MS-like mode of the CBCPW; this mode therefore displays conventional forward wave propagation. It does however cause the CPW-like mode to display backward propagation, similar to that of the NRI-TL [1]. Both of the even modes of the host MTL may be excited simultaneously from a single MS TL. Due to the field similarity of these modes, which is demonstrated in [2, 3, 7], the CPW- and MS-like modes may couple to one another. The contra-directionality of their group velocities causes power to be coupled in opposite directions which suppresses the flow of power through the unit cell and gives rise to the bandgap [17]. A more rigorous discussion of the behavior of this structure can be found in [2, 3].

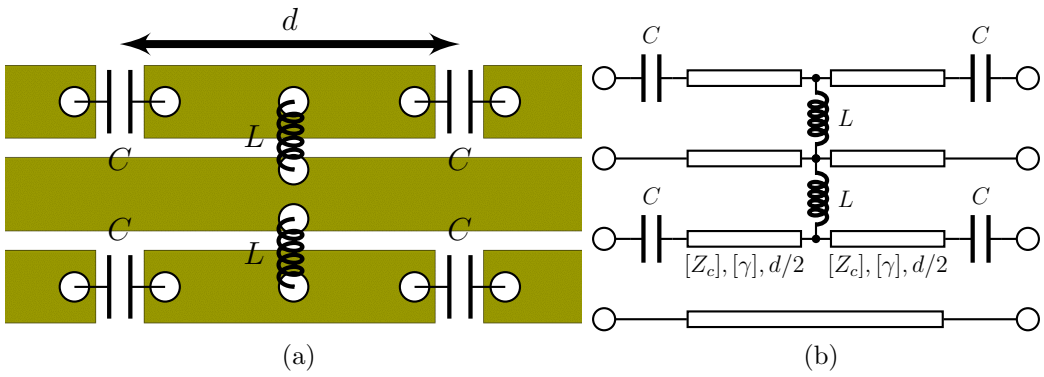

Figure 2.2: MTM-EBG unit cell with the capacitors in the CPW grounds: (a) Top view of MS layout with discrete lumped loading (conductor backing not shown) and (b) MTL equivalent circuit. This equivalent circuit model was modified from [10].

2.1.2 Modelling and Equivalent Circuit Models

The field analysis provides an excellent explanation of the properties of the MTM-EBG, but is not useful to accurately predict the behavior. These can be captured by analyzing the dispersion of the MTM-EBG through Bloch analysis, which evaluates the eigenvalues of the resulting structure. These eigenvalues correspond to propagation constants of the supported Bloch modes (i.e. the dispersion angle), and has been used extensively in several major works [1, 17]. The MTM-EBG is modelled as a MTL that has a defined form for the transmission matrices (1.3); similar transmission matrices can be derived for the shunt inductors and series capacitors [12]. Similar to the analysis of a two conductor TL, the dispersion angle at each frequency can be found by solving the eigenvalues of the net chain matrix. For a general MTL system, this can be simplified to (2.1), where $[A]$ is the top left block matrix of the total chain matrix, $[I]$ is the identity matrix and γ is the propagation constant [2, 3].

$$\det|[A] - [I]\cosh(\gamma d)| = 0 \tag{2.1}$$

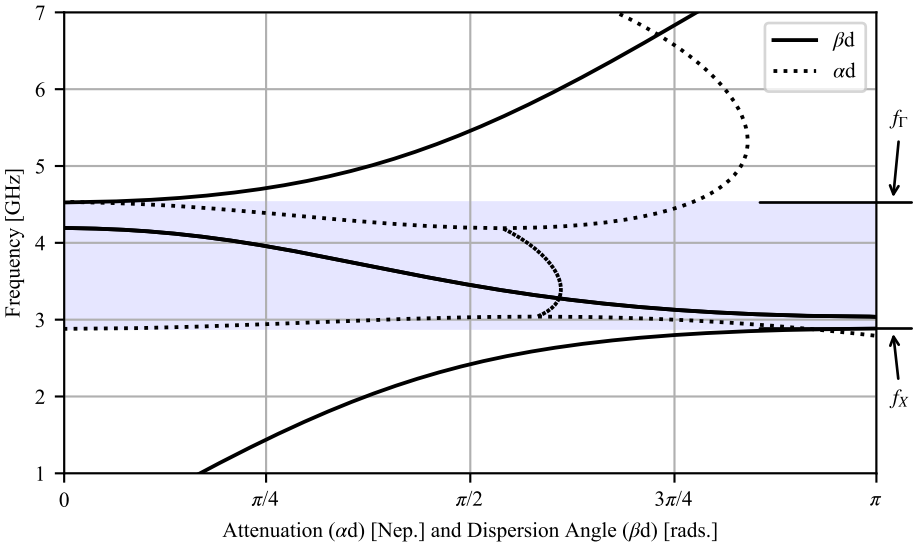

Figure 2.3: Representative dispersion diagram of the even-modes supported by an MTM-EBG. The shaded region represents the bandgap.

A representative dispersion diagram for this coupled MS-CPW mode is provided in Fig. 2.3; the shaded region represents the bandgap and indicates where the CPW- and MS-like modes interact. To a good approximation, this bandgap is enclosed by the $\Gamma-$ ($\beta d = 0$) and $X-$ ($\beta d = \pi$) point cutoff frequencies, denoted f_Γ and f_X, respectively. Outside of this region, the attenuation observed acts primarily on the CPW field components and minimally affects the MS field components. However, this should not be interpreted as claiming the MS-like mode is lossless. Very near the bandgap region in Fig. 2.3, it is apparent that the coupled MS-CPW mode is highly dispersive and may be susceptible to enhanced radiation losses; these losses are not accounted for within the equivalent circuit model.

Differences due to Layout

Depending on which conductors contain the capacitors (see Figs. 2.2 and 2.4), the dispersion of the MTM-EBG may be drastically altered to affect both the size of the bandgap and

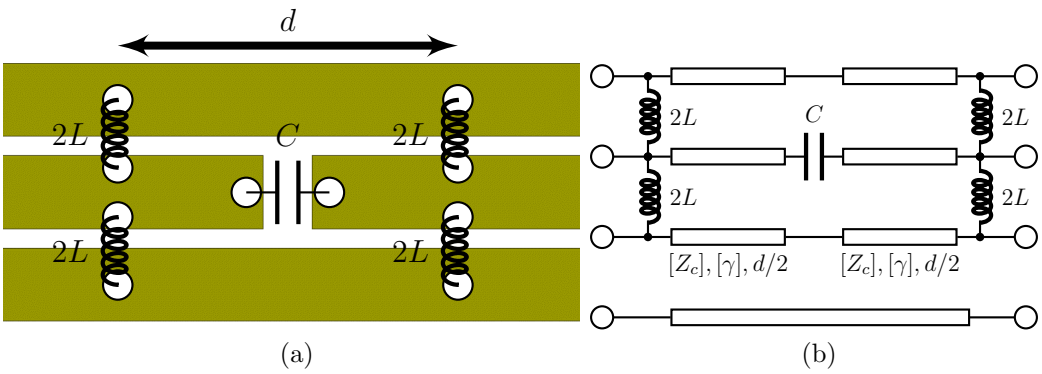

Figure 2.4: MTM-EBG unit cell with the capacitors in the CPW stripline: (a) Top view of MS layout with discrete lumped loading (conductor backing not shown) and (b) MTL equivalent circuit.

the amount of passband dispersion present. Originally reported in [7], this difference is exemplified in Fig. 2.5 where only the position of the capacitor was changed; all other geometric and loading parameters were held constant. The black curves of Fig. 2.5 represent the response of a MTM-EBG with a layout similar to Fig. 2.2; similarly, the blue curves represent the response a MTM-EBG with a layout similar to Fig. 2.4. By comparing the curves in Fig. 2.5, it is apparent that when the capacitors are placed in the ground conductors of the CPW transmission line (Fig. 2.2), the passband is more dispersive and bandgap is larger for otherwise identical dimensions. This makes this configuration better suited for applications requiring a large rejection bandwidth, or for dual-band operation for more widely spaced frequencies. On the other hand, if the operating frequencies are much closer together or a narrower rejection band is desired, a MTM-EBG with a layout similar to that of Fig. 2.4 is more appropriate.

2.1.3 Summary of Parametric studies

Parametric studies using the equivalent circuit were performed on each of the MTM-EBG variations previously discussed. A summary of the trends of increasing each of the MTM-EBG parameters on the frequencies defined in Fig. 2.6, is provided in Tables 2.2(a) and

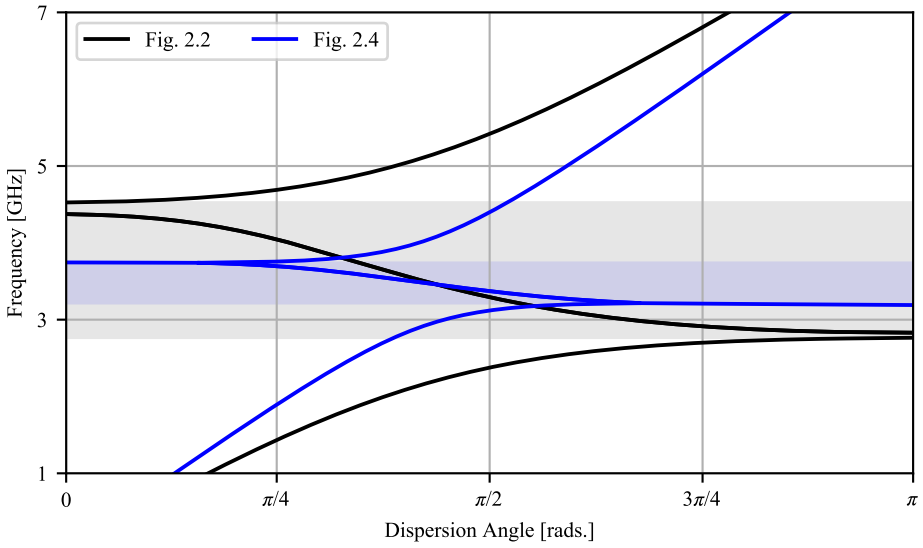

Figure 2.5: Difference in response for a MTM-EBG with a layout of Fig. 2.2 and Fig. 2.4. The shaded region represents the bandgap.

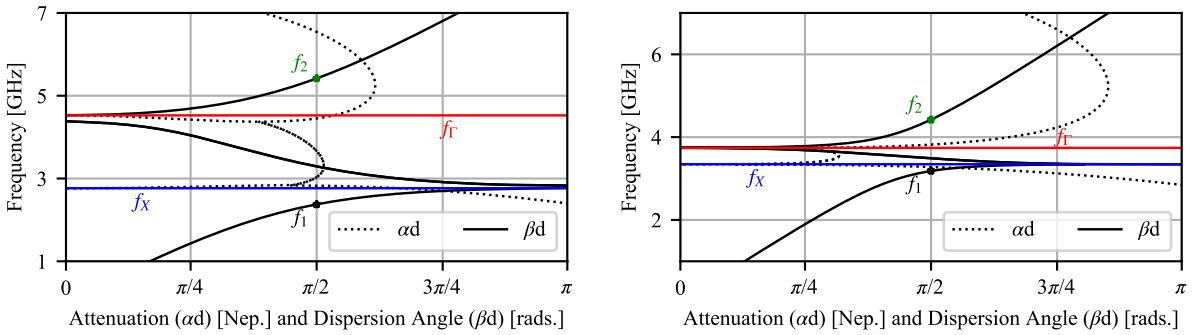

Figure 2.6: Metrics used to evaluate the effect of each of the individual MTM-EBG parameters for a layout of a) Fig. 2.2 and b) Fig. 2.4.

2.2(b); the full graphical results can be found in Appendix A. One interesting characteristic that has been revealed through these parametrics is the effect on the stripline s width on the size of the bandgap for both MTM-EBG configurations. Specifically, any increase in s when the capacitors are in the CPW ground conductors has the exact opposite effect if the capacitors are moved to the CPW stripline. This suggests additional flexibility in the physical size of the bandgap.

Table 2.1: Trends observed in increasing 8 parameters on the behavior of an MTM-EBG with a layout of a) Fig. 2.2 and b) Fig. 2.4

	s	g	W	d	C	L	ϵ_r	h
f_1	$\Uparrow$	-	$\downarrow$	$\downarrow$	-	-	$\downarrow$	$\uparrow$
f_X	$\Uparrow$	$\downarrow$	$\downarrow$	$\downarrow$	$\downarrow$	$\downarrow$	$\downarrow$	-
f_Γ	$\Downarrow$	$\Downarrow$	$\uparrow$	$\downarrow$	$\Downarrow$	-	$\downarrow$	$\downarrow$
f_2	$\Downarrow$	$\Downarrow$	$\uparrow$	$\downarrow$	$\Downarrow$	-	$\Downarrow$	$\Downarrow$

(a)

	s	g	W	d	C	L	ϵ_r	h
f_1	$\Downarrow$	$\Downarrow$	$\uparrow$	$\downarrow$	$\downarrow$	-	$\Downarrow$	$\uparrow$
f_X	$\downarrow$	$\Downarrow$	$\uparrow$	$\downarrow$	$\Downarrow$	$\downarrow$	$\downarrow$	-
f_Γ	$\Uparrow$	$\Downarrow$	-	$\downarrow$	$\Downarrow$	-	$\downarrow$	$\downarrow$
f_2	$\uparrow$	-	$\downarrow$	$\downarrow$	$\downarrow$	-	$\Downarrow\Downarrow$	$\downarrow$

(b)

$\Downarrow$ Decrease | $\downarrow$ Slight decrease | - No Effect | $\uparrow$ Slight increase | $\Uparrow$ Increase

2.2 Dual-Band Properties

Both bandgap and the resulting dispersion in the passband of the MTM-EBG have been used in the past to realize two fundamentally different mechanisms by which a device can be made dual-band. The first is to design the bandgap to restrict signal flow through one path at a given frequency but permit it to flow at another. This has been used extensively in the design of numerous dual-/multi-band devices, including dual-band patch antennas [4, 5], a dual-band wilkinson power divider [6] and a multi-band stub filter [9]. This method is practical and relatively simple to realize, but it does require additional footprint to incorporate the additional signal pathways. The second method, by distinct contrast, realizes the dual-band response by engineering the phase response of the MTM-EBG to have identical phase at two, generally arbitrary frequencies on either side of the bandgap. This mechanism was initially proposed in [7], where a dual-band quadrature hybrid coupler for GPS frequencies was designed.

When the second method of generating a dual-band response was initially proposed in [7], there were several properties that were not verified. First, is the use of dispersion analysis to design the embedded MTM-EBG when only a single unit cell is employed; second, is whether the characteristic impedance, or more generally the Bloch impedance, of the embedded

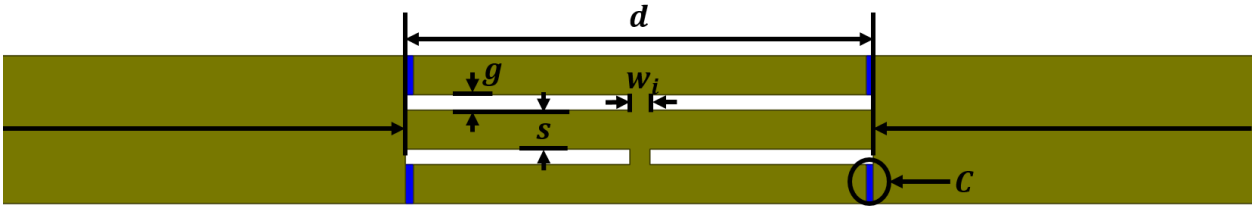

Figure 2.7: Simulation set-up to evaluate the phase and Bloch impedance of a single MTM-EBG unit cell. Discrete lumped capacitors (C) and strip inductors of width w_i were used here. The arrows indicate the port de-embedding applied to remove the effect of the MS TL.

MTM-EBG is equal to that of an underlying MS trace of identical width. These concerns ultimately affect the usage of the MTM-EBG as the goal of many dual-band components (i.e. structures that render a device dual-band) is to realize the same characteristic impedance and identical phase shift (within 180°) at both operating frequencies. These issues will be addressed in the following sections. It should be noted that only the MTM-EBG layout shown in Fig. 2.2 will be discussed in this section as it is better suited to the wider frequency separations required for the dual-band applications discussed here.

2.2.1 Validity of a single unit cell

The dispersion analysis performed on the MTM-EBG unit cell, by necessity, assumes an infinite cascade of identical unit cells. For compact dual-band devices, it is impractical to use multiple cells. Even if they were highly miniaturized, the capacitance required to operate at the desired frequency would be impractically large to realize with an interdigitated capacitor; this would restrict the applicability of these structures to much lower frequencies. It is therefore appealing to use only a single MTM-EBG unit cell for dual-band devices.

Using a single unit cell diverges substantially from its designation as a periodic structure and raises a concern on the validity of using a Bloch analysis to design these devices. So the

Table 2.2: Base parameters used to examine the dual-band properties.

s	g	W	d	C	w_i	h	ϵ_r
1.0 mm	0.4 mm	3.8 mm	12 mm	0.35 pF	0.5 mm	1.524 mm	3.0

question remains, is it appropriate to refer to the embedded MTM-EBG as a periodic device and to characterize them on the basis of their dispersion? As will be demonstrated in this section, the phase response of a single MTM-EBG is an excellent representation of the infinite cascade, implying that the dispersion analysis is a valid technique to start the design of the MTM-EBG. This is verified in simulation by creating a model of a single MTM-EBG, which is embedded in a MS TL of identical width. The simulation model is shown in Fig. 2.7, and the arrows indicate where the simulation was de-embedded to. The dimensions and loading values for this unit cell are provided in Table 2.2. Since the inductance has a relatively minor effect on the overall performance of the MTM-EBG, and due to the challenges associated with realizing a large inductance within the confines of the CPW gap, fully printed strip inductors were used in these studies. Design equations indicate that for g=0.4 and an inductor width (w_i) of 0.5 mm, the equivalent inductance is 0.2 nH [91]. Fig. 2.8(a) plots the phase response of this single unit cell against the dispersion that was predicted by the equivalent ciruit model, which incorporates the corrected inductance value. This demonstrates that a single unit cell is an excellent representation of the dispersion predicted by a Bloch analysis. Within the bandgap region, however, it is apparent that the single unit cell diverges substantially from the infinite array; this is not a significant concern as the phase within the bandgap is difficult to assign meaning to as it represents a pair of complex modes which simultaneously propagate and attenuate. As such, the field distribution can differ substantially from the fields enforced on the port faces and may invalidate the de-embdding process.

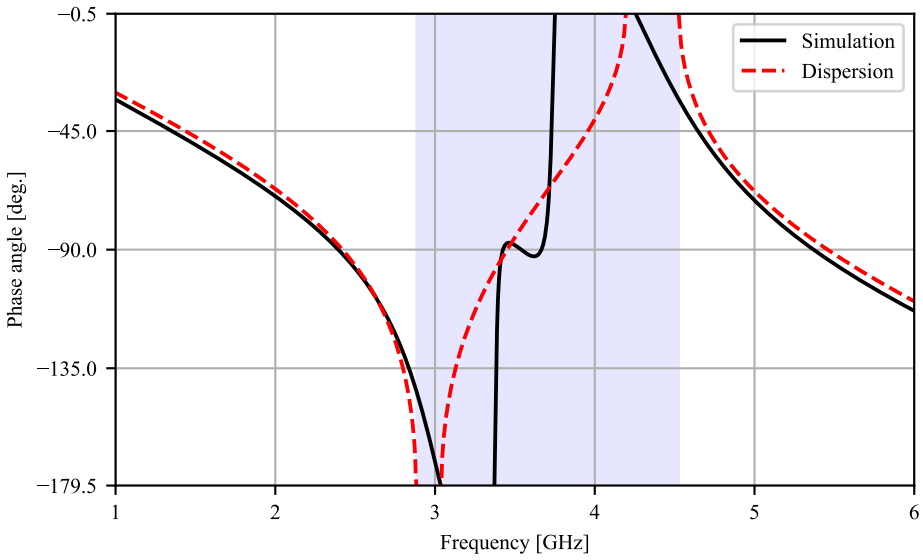

(a)

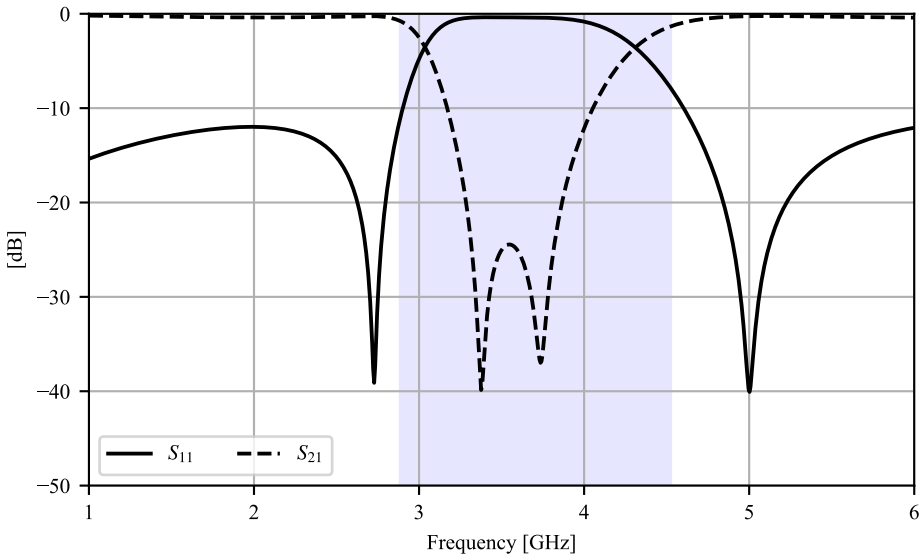

(b)

Figure 2.8: Results of the simulated single MTM-EBG unit cell: a) phase of S_{21} and the dispersion, and b) scattering parameter magnitude. The shaded region in both a) and b) indicates the bandgap predicted by the equivalent circuit model.

Even though the phase of S_{21} is an excellent representation of the dispersion, the same cannot be said about the scattering parameter magnitudes. This is shown in Fig. 2.8(b) where the shaded region again indicates the bandgap predicted by the equivalent circuit model. While it is clear that the single unit cell suppresses propagation within the same region as the bandgap, it has a much smaller bandwidth than what is predicted. However even a single cell suppresses the MS-like mode enough to be useful in dual-band devices, particularly those which rely on signal suppression such as the dual-band patch antennas proposed in [4,5], the dual-band Wilkinson power divider in [6], and the tri-band stub filter in [9].

2.2.2 Bloch Impedance

When designing the MTM-EBG for use in dual-/multi-band devices, it is generally assumed that the field distribution of the MS-like mode is nearly identical to that of a conventional MS TL, which implies that the characteristic impedance of the MS-like mode is similar to that of a conventional MS TL. This permits the use of conventional MS design equations to determine the necessary width of the MTM-EBG. The dispersiveness of the MTM-EBG complicates this assumption as it will cause the Bloch impedance of the periodic structure to be frequency dependent, which implies that the Bloch impedance of the MTM-EBG cannot be equal to the characteristic impedance of an equivalent MS TL. While this may be approximately true over a finite frequency range, it cannot be true within the bandgap. Therefore it is necessary to determine a way to evaluate the Bloch impedance of the MTM-EBG.

The multi-conductor behavior of the MTM-EBG makes it difficult to solve for the Bloch impedance directly from the constituent transmission matrix as has been done in previous periodic TL structures [22,23]. This challenge arises for several reasons: first, the necessary matrix expressions for a 4 conductor TL would require the chain multiplication of five 6×6

matrices, each of which represent the constituent elements of the MTM-EBG. While this is not an impossible feat, it is impractical given the second challenge. The MTM-EBG, in the proposed approach, is directly embedded within a MS TL; as such, it is the modal domain propagation characteristics we are concerned with, not the terminal domain propagation characteristics. As mentioned earlier, the modal characteristic impedance is not viewed to be unique by the majority of the MTL community. These factors make it impractical to attempt to find a closed form solution to the Bloch impedance of the MTM-EBG, but full-wave simulations are still valid to evaluate the impedance. As demonstrated earlier, this can also be used to design and predict the necessary phase response of the MTM-EBG. Here, an expression for the Bloch impedance based on available scattering parameter data will be derived. It is assumed here that only the MS-like mode is excited on the MTM-EBG, which allows the use of conventional single-mode expressions to solve for the Bloch impedance. This is enforced by exciting and terminating the MTM-EBG in a MS TL (i.e. embedding it in a MS TL) in the simulation modal; an example case of this is shown in Fig. 2.7. As mentioned earlier, one of the goals of dual-band components (i.e. structures that render a device dual-band) is to realize the same characteristic impedance at both operating frequencies [41, 43–45, 47, 53, 55]. In many dual-band devices, the solution begins with deriving a matrix expression for the behavior of the dual-/multi-band device. From this matrix expression, which may be the transmission matrix or impedance/admittance matrix, specific conditions may be solved for based on the entries. This was not used to find solutions in [41] as the structure was simple enough that it could be easily solved from the input impedance equation. In [44], for example, the stepped impedance stub-line structure was expressed as a transmission matrix. Given the desired characteristic impedance (Z_B) and phase angle (βl) of $90°\pm180°$, the entries can be set to the desired values (i.e. $A = D = 0$, $B = jZ_B$, $C = \frac{j}{Z_B}$). The necessary conditions on the stub length and impedance values can then be solved for from the resulting expressions. A similar approach will be used here for the MTM-EBG, but relies on numerical data.

$$\begin{bmatrix} A & B \\ C & D \end{bmatrix} = \begin{bmatrix} \cos\beta l & jZ_B \sin\beta l \\ jY_B \sin\beta l & \cos\beta l \end{bmatrix} \tag{2.2}$$

From (2.2) the characteristic impedance, or Bloch impedance with respect to the MTM-EBG, can be solved for by using (2.3):

$$Z_B = \sqrt{\frac{B}{C}} \tag{2.3}$$

(2.3) can be changed to accept scattering parameters by using conversion tables, which are widely available in a number of prominent textbooks [92]. Similar transformations using, for example, impedance parameters are equally simple and primarily dependent on convenience. The relevant conversions are shown in (2.4) and (2.5):

$$B = Z_0 \frac{(1+S_{11})(1+S_{22}) - S_{21}S_{12}}{2S_{21}} \tag{2.4}$$

$$C = \frac{1}{Z_0} \frac{(1-S_{11})(1-S_{22}) - S_{21}S_{12}}{2S_{21}} \tag{2.5}$$

Substituting (2.4) and (2.5) into (2.3) and reducing, leads to (2.6):

$$Z_B = \sqrt{Z_0 \frac{(1+S_{11})(1+S_{22}) - S_{21}S_{12}}{2S_{21}} Z_0 \frac{2S_{21}}{(1-S_{11})(1-S_{22}) - S_{21}S_{12}}}$$
$$= Z_0 \sqrt{\frac{(1+S_{11})(1+S_{22}) - S_{21}S_{12}}{(1-S_{11})(1-S_{22}) - S_{21}S_{12}}} \tag{2.6}$$

When using scattering parameters as a basis for the Bloch impedance, it may appear as though Z_B is dependent on a definition of Z_0; however, the scattering parameters will also change based on the value of Z_0. The net effect of this co-dependence is a general in-variance of Z_B to changes in Z_0 such that the characteristic impedance can be nearly arbitrarily chosen; this is only true for referencing the data against a new port impedance. Changing the characteristic impedance of the actual underlying input and output MS TLs, and therefore their widths, will have an effect on the junction parasitic effects. These parasitic effects will have an effect on the value of Z_B; this is found to be relatively minor though.

Using (2.6) and the simulation data from Section 2.2.1, the Bloch impedance of a single MTM-EBG can be calculated. These results for are provided in Fig. 2.9. Consider the case where the width of the MTM-EBG is 3.8 mm, which in a conventional MS TL corresponds to a characteristic impedance of 50 Ω. As shown in Fig. 2.9, the Bloch impedance of this unit cell is relatively flat far from the bandgap and larger than 50 Ω. Very near the bandgap, however, there is substantial variation in value of the Bloch impedance. The Bloch impedance is largely affected by the width of the MTM-EBG implying that conventional MS design equations are a valid starting point for the design of these devices.

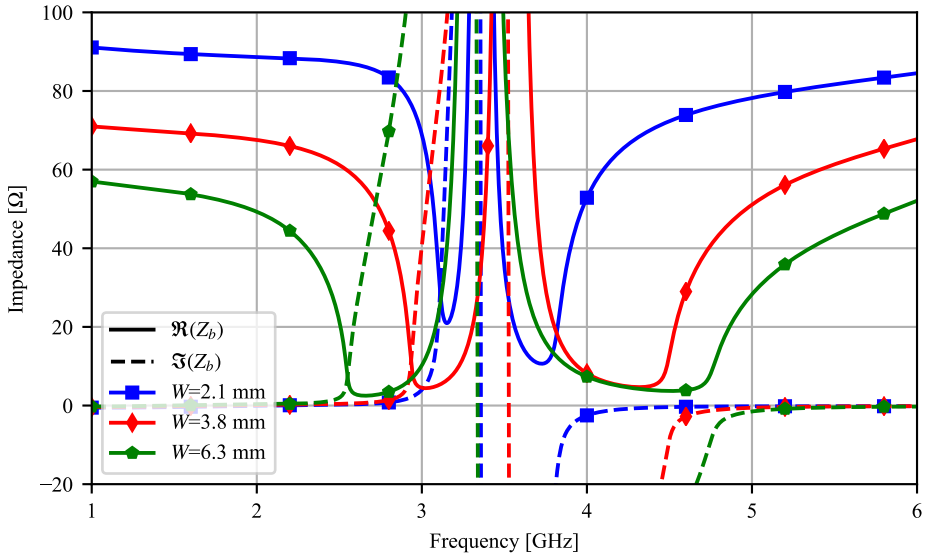

Figure 2.9: Bloch impedance of a single MTM-EBG unit cell using (2.6).

2.3 Filtering Properties

The studies on the dual-band properties of the MTM-EBG focused on an MTM-EBG with a layout identical to that of Fig. 2.2 as this configuration introduces more passband dispersion. This made it more applicable to the dual-band applications examined in this thesis where wider separations were required. To examine the filtering aspect, however, an MTM-EBG with a layout of Fig. 2.4 will be examined as it presents with a narrow rejection band that is on the order of size necessary to filter out select channels in telecommunications.

Previous MTM-EBG implementations were designed using only the equivalent MTL circuit model and subsequent dispersion analysis. While this provides the most robust view of the behavior of the MTM-EBG, it can be difficult to design for a desired response without in-depth knowledge of the MTM-EBG behavior. For this reason, expressions that can relate the loading values (L and C) to the bandgap edge (cut-off) frequencies are incredibly useful. In two-conductor systems, such as the NRI-TL [1], closed-form expressions are available

to determine these values for a given geometry. These expressions are substantially more complex for an MTL system, and are somewhat non-intuitive in their usage. For this reason, these expressions and a step-by-step procedure of how they may be used have been provided in Appendix B. It is important to note that this procedure is specific to the MTM-EBG topology shown in Fig. 2.4 and must be adapted for different MTL geometries and placement of reactive-loading elements.

2.3.1 Tunability

The bandgap of the MTM-EBG is heavily dependent on the capacitance (C) of the MTM loading. An example of this is provided in Fig. 2.10(a), which demonstrates the bandgap predicted by the equivalent circuit model [see Fig. 2.4(b)] for different values of C. In addition, Fig. 2.10(b) plots the results of numerically inverting the procedure discussed in Appendix B, with a fixed inductance of 0.08 nH. This allows for a visualization of the effect of increasing the capacitance on the center frequency (solid line) and bandwidth (dotted line). The superimposed star-markers represent the center frequency and bandwidths calculated from the curves in Fig. 2.10(a). As the capacitance increases, with all other parameters held constant, the bandgap shifts down by an appreciable amount which suggests that a method of systematically modifying the capacitance could make this device easily tunable. Furthermore, as demonstrated in Fig. 2.10, such a mechanism does not drastically alter the passband phase response of the MTM-EBG if the capacitor is placed in the CPW stripline conductor. Such a configuration is more appealing for tunability as it requires fewer tuning elements and helps to ensure better passband performance.

These results further demonstrate the effect of tuning only the capacitance on both the bandwidth and center frequency of the response and also provide a clearer image on the effective tuning range. As the capacitance is increased, the decrease in center frequency becomes less

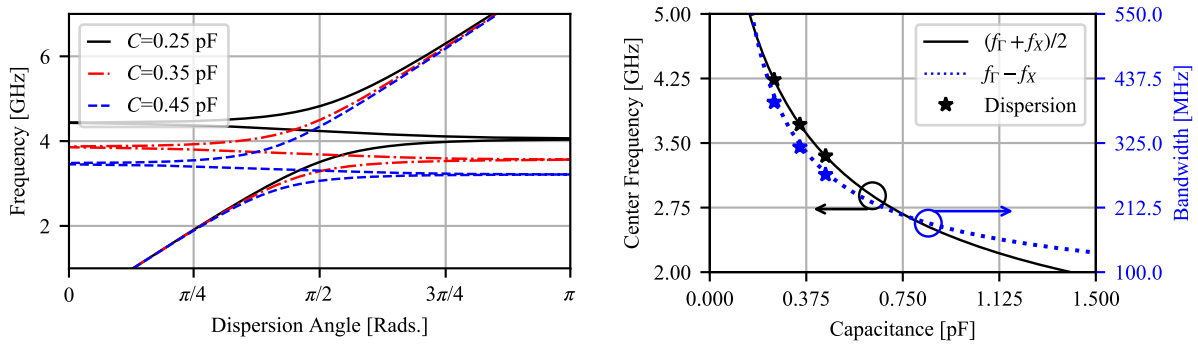

(a) (b)

Figure 2.10: Effect of varying only the capacitance C of an MTM-EBG unit cell based on a) the equivalent circuit model and b) the numerically inverting the anallytical expressions in Appendix B.

pronounced. This becomes increasingly exaggerated for larger and larger capacitance values, and effectively limits the tuning range to the maximum capacitance available to the tuning element.

For traditional planar filters, this tuning is accomplished by relying on a electrostatic bias network to vary the capacitance of either a varactor, or a MEMS capacitor. However, both of these technologies have very pronounced drawbacks. A varactor is a semi-conductor device that relies on the voltage-dependent capacitance of a diode; this is a popular choice for tunability due to its low cost and wide availability. In order to operate, however, these components require a DC bias network to alter the capacitance. This can drastically alter the performance of the filter as it requires the incorporation of various DC blocks and RF chokes that may be challenging to accurately model. The equivalent circuit model of the MTM-EBG can be, with relative ease, be modified to include the effect of the required bias network; part of this has been discussed in [2, 3] with the effect of capacitors in each conductor. The varactor is fundamentally a semi-conductor device and is therefore non-linear. This carries a number of consequences, one of which is intermodulation which seriously degrades the performance of modern telecommunication systems [93]. As this project was started with

support from our industrial sponsors, KP Performance Antennas and Infinite Electronics Group, even low level intermodulation was a serious concern for their desired applications. This prompted investigations into tuning mechanisms which do not substantially contribute to intermodulation.

MEMS, due to their primarily mechanical nature, are attributed to smaller non-linearities but are substantially more complex to fabricate [78]. As this was intended to be used in industrial applications, and therefore needs to be fabricated at low costs, MEMS tuning was determined to be impractical. Macroscopic mechanical tunability, as to differentiate from the mechanism behind MEMS capacitors, is typically exclusive to larger 3D cavity filters.

It is clear from Table 2.1 and Fig. 2.10, however, that any change in the capacitance will change the size of the bandgap as well. Without a mechanism of correcting for these changes, substantial variations in the bandwidth can be expected as demonstrated in previous tunable MTM- and EBG-based filters [88, 89, 94, 95]. Conventional filter theory indicates that for an N-th order filter, using $2N + 1$ tuning elements can completely control the bandwidth behavior by enabling control over both the resonators and the coupling regions. This is not only challenging to implement, but also impractical for higher order filters. Recently proposed constant ABW filters counteract this change in ABW by engineering the coupling coefficient to be inversely related to frequency, thereby minimizing the number of tuning elements necessary to realize the response [79–86]. Since the MTM-EBG is designed on the basis of dispersive modes, not coupled resonances, such an approach is not employed here.

Instead, an alternate mechanism that affects the propagating Bloch mode of the structure will be used here. This is based heavily on the principle of non-synchronous tuning; in a tunable filter, this maintains a constant ABW by tuning each of the resonating elements independently. In the case of the MTM-EBG, this modification artificially increases the

bandgap region. An example of this is shown in Fig. 2.11, where the transmission of a three-cell MTM-EBG array (solid line) is plotted against the transmission of a single MTM-EBG (dashed line). When the neighbouring cells are detuned (in this example the capacitance was changed), the stopband performance and center frequencies are maintained but the stopband ABW is increased. As a result the insertion loss within the rejection band is reduced.

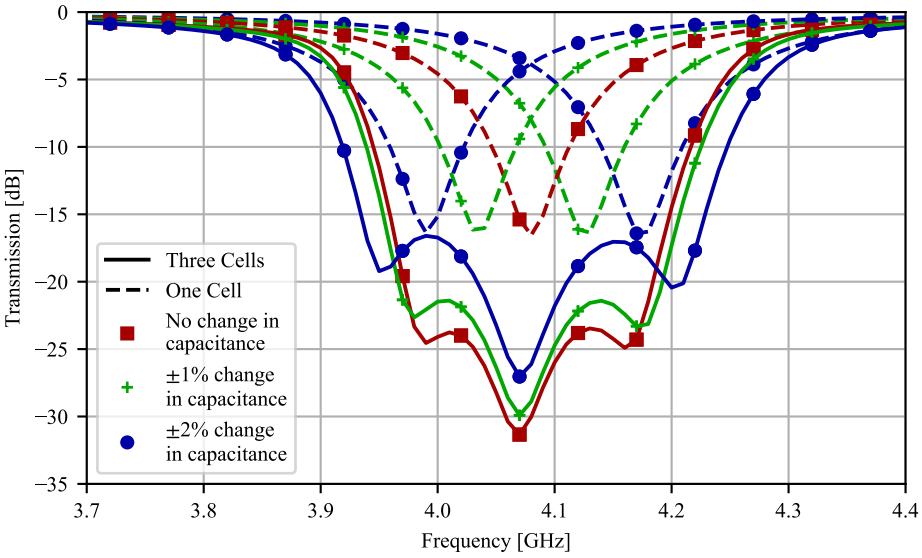

Figure 2.11: Transmission response of a three unit cell MTM-EBG array for increasing changes in the capacitance of neighbouring unit cells. Super-imposed is the response of the individual detuned MTM-EBG unit cells.

2.3.2 Embedded Bandstop Filters

As has been demonstarted in several previous works, such as [7, 10], the embedded MTM-EBG presents a strong, predictable rejection band with only a single unit cell. These suggest that the MTM-EBG is well suited to compact and embedded filtering applications, similar to what has been examined for alternate MTM and EBG topologies [68–72, 96]. As an example of this consider the response of N cascaded MTM-EBG shown in Fig. 2.12. These MTM-EBG unit cells were first embedded within a MS trace of the same characteristic impedance similar to what was done to examine the Bloch and phase response of the MTM-EBG. The parameters of each of these unit cells are identical to what is defined in Table 2.2.

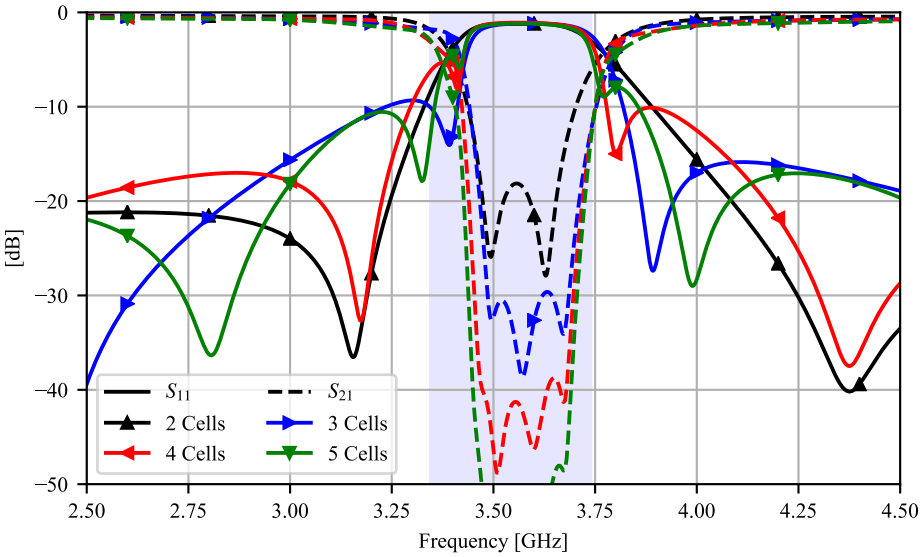

Figure 2.12: Scattering parameter magnitude for an array of different numbers of identical MTM-EBG unit cells. The shaded region represents the bandgap predicted by the equivalent circuit model.

As is apparent in Fig. 2.12 the magnitude response of a single MTM-EBG unit cell is not a good approximation of the bandgap. Increasing the number of unit cells increases the stopband bandwidth, and causes the magnitude response to approach the response predicted by the equivalent circuit model. However, the stopband is only one aspect of the performance of a bandstop filter; the other is the passband where it should, ideally, have perfect transmsission. As is apparent in the various curves of Fig. 2.12, the MTM-EBG-based filter generally has excellent passband performance; an exception, however, is the performance very near the bandgap.

Certain aspects of the passband performance of the embedded MTM-EBGs change substantially as additional unit cells are incorporated. Most notable is the appearance of additional reflection minima suggesting that their presence is related to the total structural length and should therefore occur at half-wavelength intervals; this is demonstrated in Fig. 2.13 where the layout employed is shown in Fig. 2.13(a). The markers in Figs. 2.13(b) and 2.13(c) correspond with one another. Far from the bandgap, as indicated by the star markers, these

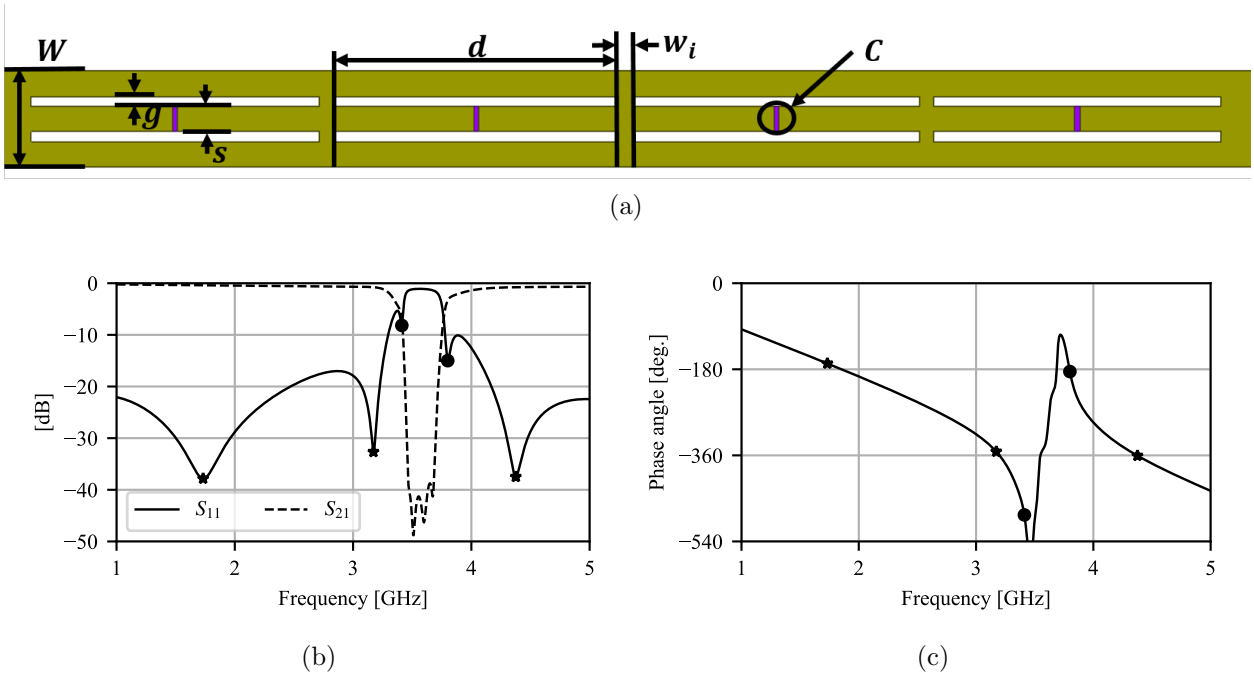

Figure 2.13: a) Layout of a four cell MTM-EBG-based filter, b) magnitude response and c) de-embedded transmission phase of a four unit cellbandstop filter. The markers indicate the location of the reflection zeros.

minima do infact correspond with half-wavelength intervals of the filter; near the bandgap, as indicated by the circle markers, this is not true. These minima are associated to lower return loss near the bandgap of the MTM-EBG. This may limit the application of the MTM-EBG-based bandstop filter to narrowband filtering applications without substantial tuning of the overall performance.

Through the careful introduction of mirrored asymmetries such that the edge (outer cells) differ from the inner cells, it is possible to effectively eliminate these poor return loss regions. While this further diverges from the assumption of a uniform array of unit cells, it has been previously demonstrated that even a single unit cell is representative of the infinite cascade. Parametric studies were performed on an asymmetric four cell filter, and these results are summarized in Table 2.3 based on the metrics in Fig. 2.14; the full results of this study are available in Appendix C.

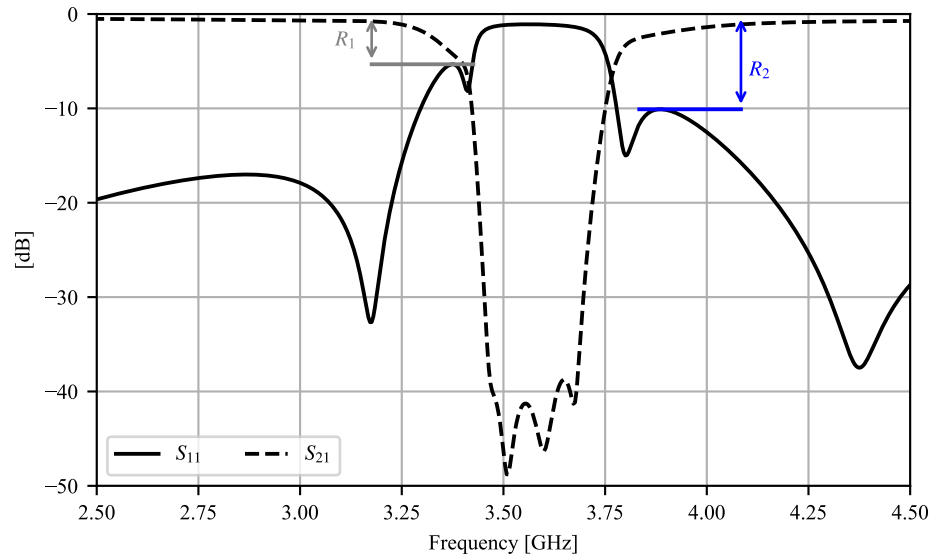

Figure 2.14: Metrics used to evaluate the effect of asymmetries on a mirrored four cell MTM-EBG-based filter.

Table 2.3: Summary of the effect of 5 parameters on the behavior of a four cell MTM-EBG-based, asymmetric filter when the asymmetry is in a) the outer cells and b) the inner cells.

	s	g	W	d	C
R_1	$\downarrow$	$\downarrow$	$\Uparrow$	-	$\Downarrow$
R_2	$\Downarrow$	$\Uparrow$	$\downarrow$	$\Uparrow$	$\Uparrow$

(a)

	s	g	W	d	C
R_1	$\Downarrow$	$\Uparrow$	$\Downarrow$	$\Uparrow$	-
R_2	$\Uparrow$	$\downarrow$	-	$\Downarrow$	$\Downarrow$

(b)

$\Downarrow$ Decrease | $\downarrow$ Slight decrease | - No Effect | $\uparrow$ Slight increase | $\Uparrow$ Increase

Chapter 3

Dual-Band Corporate Feed Networks using embedded MTM-EBG

3.1 Motivation

Corporate feed networks can be generalized to include any device that divides power to a large number of output ports. These are of particular interest to antenna-array applications as they permit the array to be excited from a single input port, while being able to control the magnitude and phase of the output ports. Canonically, these networks are formed by cascading simple T-junction power dividers, which are easily modeled and offer scalability over a wide frequency range. However, their dependence on impedance transformers, the simplest of which is a quarter-wavelength MS TL, introduces several limitations on the performance of these power dividers and corporate feeds: it is severely limiting in applications demanding compactness since the TL length constrains the operating frequency and dictates the size of the device; and the resonant mechanism of impedance matching implies narrow bandwidths that also contribute to insertion losses. Widening the bandwidth using multi-stage impedance transformers exacerbates the size and insertion-loss issues.

Owing to their frequency-dependence, such components do not directly lend themselves to the excitation of (non-harmonically related) dual-/multi-band antenna arrays; typically,

independent corporate feeds are required at each operating frequency, which greatly increases the total footprint and complexity of the network. Some efforts have recently been taken in literature to develop compact structures that can render a network dual-band [41, 43–45, 47, 53]. These are often limited in the frequency ratios they can realize and typically have higher insertion losses due to their reliance on additional resonances. Furthermore, these structures are not easily expanded to multi-band networks; multi-band solutions have been proposed [55, 56] but are often electrically large and/or suffer from relatively ad-hoc design methodologies. Network-specific solutions exist, such as [46, 49]. In [46] a port-extended quadrature coupled hybrid is proposed for dual-band operation. This port-extension technique is found as a solution to the quadrature coupled hybrid and therefore is unique to this network, making it difficult to apply to other networks; in addition, the total size of the network is significantly larger than either single-band variation. In [49], a dual-band Wilkinson power divider is proposed, which relies on multi-section TL and RLC loading. This design depends on the availability of discrete lumped elements and would be difficult to scale to higher frequencies.

3.1.1 Objectives

The goal of this chapter is to develop a dual-band corporate feed network that is suitable for antenna array applications using a variation of the original MTM-EBG topology proposed in [2]. Inspired by WLAN as a representative application, the targeted operating frequencies are 2.4 and 5.0 GHz. To experimentally verify the impedance properties that were discussed in Chapter 2, a fully printed MTM-EBG is designed to appear as a dual-band impedance transformer with a characteristic impedance of 70.7 Ω and cascaded in a back-to-back configuration to measure the behavior. This MTM-EBG is then modified for a characteristic impedance of 35.4 Ω and used to feed a T-junction power divider, thereby rendering the junction dual-band. It will be shown that the resulting T-junction power divider demonstrates

dual-band behavior with return-loss and insertion-loss performance at each band comparable to or better than that of an equivalent unloaded design of the same physical length, operating at the intermediate frequency. An initial design of the corporate feed network is examined in which three T-junctions are cascaded to form the corporate feed network; however, through this design, a sensitivity of the MTM-EBG to asymmetric current distributions was identified. To minimize the effect of this sensitivity, and to make the resulting network better suited to antenna arrays, the corporate feed network was modified and re-arranged. The resulting modified corporate power divider is shown to have comparable performance to *individual single frequency* networks designed around each operating point.

3.1.2 Outline

This chapter is organized as follows: Section 3.2 will present the design methodology used to create a desired Bloch, or characteristic, impedance and phase response, and demonstrates these properties through the design of a dual-band impedance transformer. Section 3.3 discusses the application of the designed impedance transformer in a T-junction power divider and presents experimental results for the fabricated device, and demonstrates, that when compared to alternate dual-band technologies, the MTM-EBG-based approach offers a smaller footprint and additional flexibility in the loss, phase and rejection performance. Section 3.4 discusses the design of the dual-band corporate feed network that is formed by cascading instances of the dual-band T-junction power divider proposed in Sec. 3.3. This structure is then fabricated and these results are discussed and potential sources of error are identified. Aspects of this chapter have also been published in [8, 10].

3.2 Back-to-Back Impedance Transformer

The impedance transformer is simple component capable of changing a real impedance into another by using a quarter-wavelength TL of predetermined characteristic impedance. This device is used in a wide number of devices to ensure good matching at a desired frequency; this frequency dependence does ultimately offer limit the range over which it can operate. A simple dual-band impedance transformer was proposed in [41] and operates using multiple impedance segments. This device is simple to design and implement, but due to the dependence on multiple resonant lengths it does suffer from additional loss and is, by necessity, electrically large. Here a dual-band impedance transformer is realized using an embedded MTM-EBG and experimentally verified in a back-to-back configuration.

3.2.1 Design

For a conventional impedance transformer, two conditions must be satisfied at the operating frequency: first, the transformer must incur 90° of phase; second, the characteristic impedance must be the geometric mean of the generator and load impedance. Here, we design an impedance transformer to convert 50 Ω to 100 Ω and back. In order to design an embedded MTM-EBG capable of realizing both impedance-transformation conditions at each of 2.4 and 5.0 GHz, the topology of Fig. 2.2 is selected to introduce sufficient dispersion. Although there is a procedure to rapidly design the reactive loading in Appendix B, it is limited to the position of only f_Γ and f_X and offers no insight into the 90° phase frequencies f_1 and f_2. As such, this design, and subsequent designs in this chapter, primarily rely on full dispersion analysis. The following steps outline a procedure that can be used to design a dual-band component:

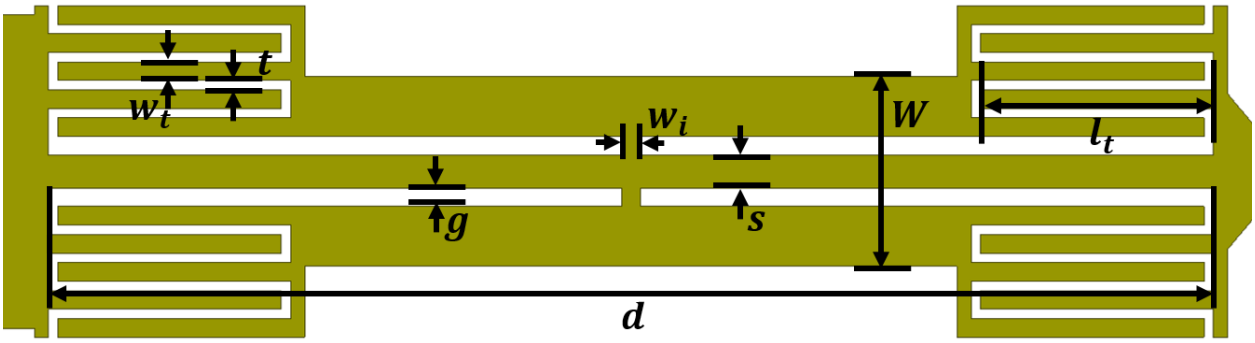

(a)

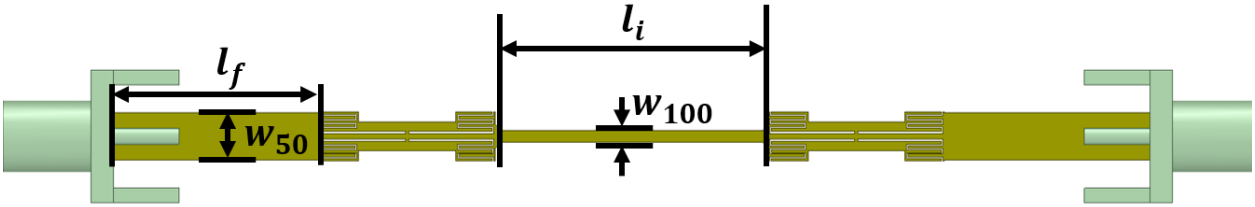

(b)

Figure 3.1: a) Layout and relevant dimensions of the embedded MTM-EBG unit cell: W=2.03 mm, d=12.5 mm, s=0.35 mm, g=0.2 mm, t=0.1 mm, w_t=0.2 mm, l_t=2.5 mm, w_i=0.2 mm. b) Layout and relevant dimensions of the back-to-back dual-band impedance transformer: w_{50}=3.36 mm, w_{100}=0.84 mm, l_i=20 mm, l_f=15 mm.

1. *Host TL:* The host TL must first be determined as this will strongly affect the characteristic impedance of the underlying MS TL. As shown in Table 2.2(a), the thickness of the dielectric does not have a substantial effect on the performance of the MTM-EBG. In order to more easily realize the properties with larger features, a thicker substrate was used. Table 2.2(a) shows that the position of the bandgap is largely affected by the permittivity (ϵ_r) of the host medium. While larger values of ϵ_r would offer additional miniaturization, they would also require smaller features to realize the desired impedance levels. Rogers RO4350B (ϵ_r=3.66, tanδ=0.004) of thickness 1.524 mm and clad in 35-μm copper was selected as a reasonable balance between both of these characteristics. Since the MTM-EBG will be designed to transform 50 Ω to 100 Ω, the necessary transformer impedance is therefore 70.7 Ω. This is largely dominated by the width of the MTM-EBG (W) and can be estimated using conventional MS design

equations [92].

2. *TL Length:* The locations of the equiphase points of the MTM-EBG are dependent on both the loading (L and C), the unit cell length (d), as well as the CBCPW dimensions (s and g). This offers a large degree of freedom when choosing the necessary length of the TL; for example, the length can be greatly reduced by using a larger capacitor with finer features. Similarly using a smaller capacitance can be corrected for by increasing the length of the unit cells. However in each of these extremes, one of the operating frequencies will be in a more dispersive region of the MTM-EBG and will therefore suffer from higher losses. Furthermore, since fully printed interdigitated capacitors will be used with a minimum feature size of 100 μm, and to reduce the losses at both frequencies, the length of this structure was selected as based on the quarter-wavelength of the intermediate frequency (3.7 GHz).

3. *Reactive Loading:* As demonstrated in Table 2.2(a), the inductance does not have a strong effect on the passband phase response; furthermore, in order to realize the MTM-EBG as a fully printed structure, the inductance was selected to be small and implemented using strip inductors of width 0.2 mm (approximately 0.1 nH). Since the interdigitated capacitors were placed in the CPW ground conductors, there was additional flexibility in the total width by permitting them to extend beyond the desired width of W.

4. *CBCPW Dimensions:* Based on the length (d), width (W) and loading values used for the MTM-EBG, the internal CBCPW dimensions (s and g) can be tuned to shift the phase at the desired operating frequencies. Based on the results in Section 2.1.3, when the capacitors are placed in the CPW ground conductors, increasing the CPW stripline (s) will cause the phase at 2.4 GHz to increase while decreasing the phase at 5.0 GHz; increasing the CPW gap (g) will cause the phase at both frequencies to increase.

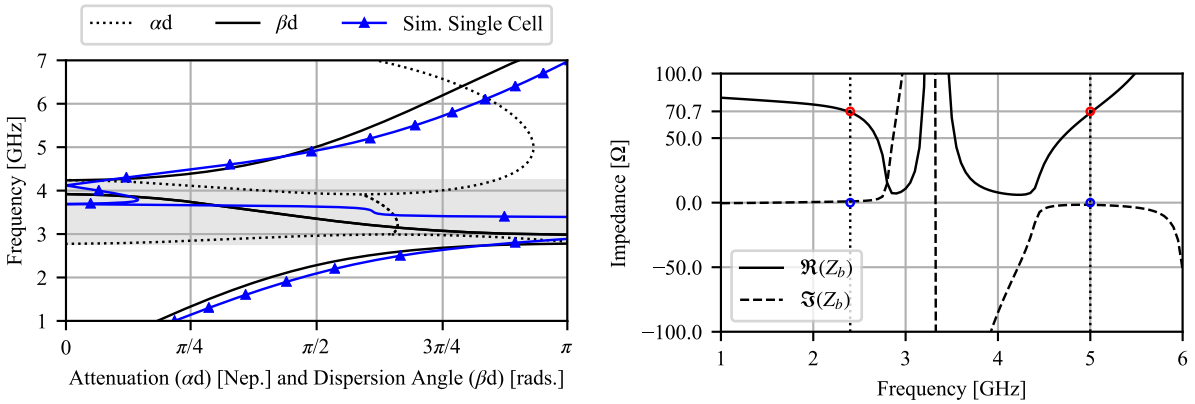

(a) (b)

Figure 3.2: a) Even-mode dispersion data for the MTM-EBG shown in Fig. 3.1(a). The bandgap for the coupled MS-CPW mode can be seen as the highlighted region from 2.78 GHz to 4.24 GHz. The super-imposed line provides the S_{21} phase of a single, fully printed MTM-EBG unit cell. b) Bloch impedance extracted from a single MTM-EBG unit cell shown in Fig. 3.1(a). The red and blue circles indicate the desired level of the real and imaginary parts.

The final MTM-EBG unit cell and network layout, after tuning to account for minor parasitic effects introduced by the connection to a conventional MS TL and the additional width of the capacitors, are shown in Figs. 3.1(a) and 3.1(b). A back-to-back configuration was selected to measure the MTM-EBG by permiting measurements to be made using a 50 Ω input port, while demonstrating the flexibility in the design of the Bloch impedance of the MTM-EBG. Prior to fabrication, an initial verification of the desired properties was performed on a single MTM-EBG embedded within a 70.7-Ω MS TL; this is identical to what was done in Chapter 2 to evaluate the phase and Bloch impedance of a single MTM-EBG. The comparison to the corresponding dispersion data is shown in Fig. 3.2(a), while the Bloch impedance is shown in Fig. 3.2(b). As is apparent in Fig. 3.2(a), the phase response of a single MTM-EBG is once again well captured by the dispersion analysis. The shaded region in this plot represents the bandgap predicted by the Bloch analysis; within this region, it is difficult to assign any meaning to the phase as it represents a pair of complex modes, which propagate and attenuate simultaneously.

Compared to the initial demonstration of the accuracy of a single unit cell to the infinite array in Sectiom 2.2.1, the results shown in Fig. 3.2(a) are noticeable more mismatched. This is attributed primarily to the presence of fully printed interdigitated capacitors that extend beyond the nominal width of the MTM-EBG. The per-unit properties of the underlying MTL therefore differ over the length of the fully printed unit cell and contribute to additional parasitic effects; these introduce the observed differences between the single cell phase and the predicted dispersion of the equivalent circuit model. Fig. 3.2(b) provides the Bloch impedance of the single MTM-EBG as calculated from (2.6). At 2.4 and 5.0 GHz respectively, the exact values are evaluated as Z_B=70.21+j0.99 and Z_B=71.74−j1.66 Ω respectively. While there is an imaginary part in both of these Bloch impedances, they are small enough to not drastically alter the propagation and simple represent additional losses introduced present in the MTM-EBG.

3.2.2 Simulation and Experimental Results

Simulation results for this structure are provided in Fig. 3.3 (solid red curves) and it is clear that the structure operates well at both of the desired operating frequencies. At 2.4 and 5.0 GHz respectively, which represent the points of minimum S_{11} the S_{11} is equal to -32.62 dB and -48.31 dB and the S_{21} is equal to -0.46 dB and -0.83 dB. Additional resonances are observed in both operating bands at 1.7 and 4.7 GHz; these are secondary resonances related to the length of 100-Ω TL connecting the two MTM-EBG unit cells, and represent an alternate matching condition for this configuration. The device is very well matched at both of the frequencies with low insertion losses, indicating it is properly transforming the impedances.

The back-to-back impedance transformer shown in Fig. 3.1 was fabricated using a LPKF Protolaser U3 laser milling system; the fabricated board is shown in Fig. 3.4 with an inset

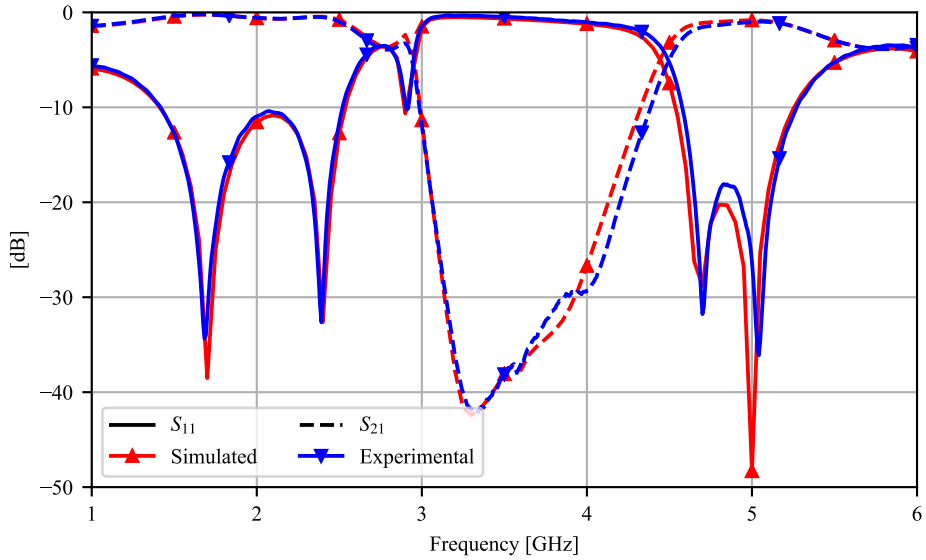

Figure 3.3: Simulated and experimental results for the back-to-back dual-band impedance transformer.

depicting one of the printed capacitors. A minor discoloration of the substrate surface due to the fabrication process can be observed across the plane of symmetry. This was introduced during the fabrication procedure and indicates that the underlying substrate was burned during the heating of the copper; this, however, had no effect on the results. The experimental results (dashed blue curves) are plotted against the simulated data in Fig. 3.3. As is apparent by these comparisons, the simulated and experimental results are in excellent agreement with one another. Small shifts in operating frequencies can be observed but are relatively minor and may be mitigated through further optimizations and better control over fabrication tolerances. At 2.39 and 5.04 GHz respectively, which represent the shifted frequencies of minimum S_{11}, the S_{11} is measured to be -32.63 dB and -36.12 dB and the S_{21} is equal to -0.50 dB and -0.96 dB; again this ignores the secondary resonances at 1.7 and 4.7 GHz.

3.3 T-junction Power Divider

3.3.1 Design and Simulation

The T-junction power divider is a simple power dividing structure useful in situations where isolation between the output ports in not required. Since it is a three-port network, it cannot be simultaneously matched, lossless and reciprocal; in the case of the T-junction it sacrifices the matching. There are two configurations which will allow it to be matched to the same impedance at each port; 1) 70.7 Ω impedance transformers can be placed on each of the output arms resulting in a 50 Ω junction input impedance; 2) a 35.4 Ω impedance transformer can be placed on the input of the junction, allowing a 50 Ω input line to be matched to the 25 Ω junction. In Section 3.2, the MTM-EBG designed there would have been well suited for this application; each junction would therefore require two such transformers. To reduce the number of frequency dependent elements, as well as to further demonstrate the flexibility of the MTM-EBG's Bloch impedance, it will be re-designed to appear as a 35.4 Ω impedance transformer.

The design of this impedance transformer follows the same steps as those outlined in Section 3.2.1, and will therefore not be re-iterated here. Furthermore, the same substrate [Rogers RO4350B (ϵ_r=3.66, tanδ=0.004, h=1.524 mm)] will be used for the power divider. After

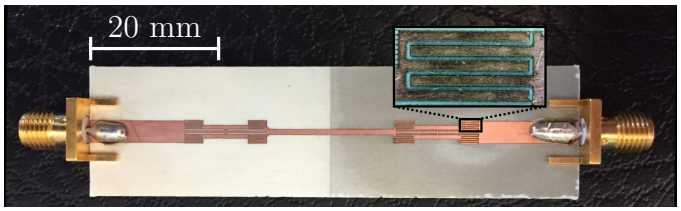

Figure 3.4: Fabricated back-to-back dual-band impedance transformer. The inset magnifies the interdigitated capacitor with 100 μm features.

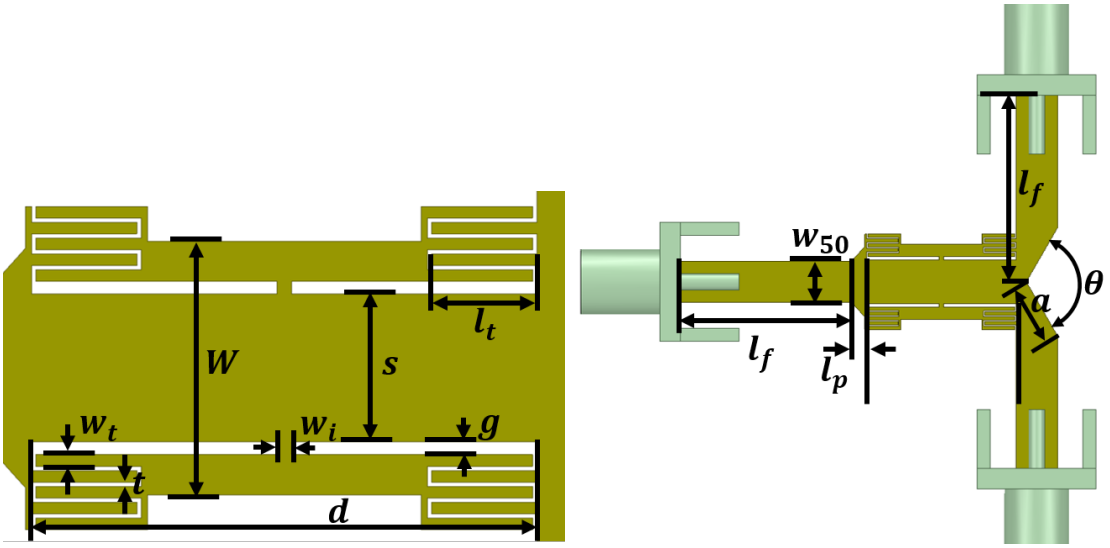

(a) (b)

Figure 3.5: a) Schematic and dimensions of the 35.4 Ω MTM-EBG unit cell:W=6 mm, d=12 mm, w_t=0.275 mm, s=3.5 mm, g=0.3 mm, t=0.1 mm, l_t=2.5 mm, w_i=0.35 mm. b) Schematic and dimensions of the MTM-EBG-loaded power divider: w_{50}=3.61 mm, l_f=15 mm, l_p=1.2 mm, a=5 mm, θ=120°.

following these steps and tuning to account for parasitic effects, the final MTM-EBG dimensions are provided in Fig. 3.5(a) and the power divider layout provided in Fig. 3.5(b). As

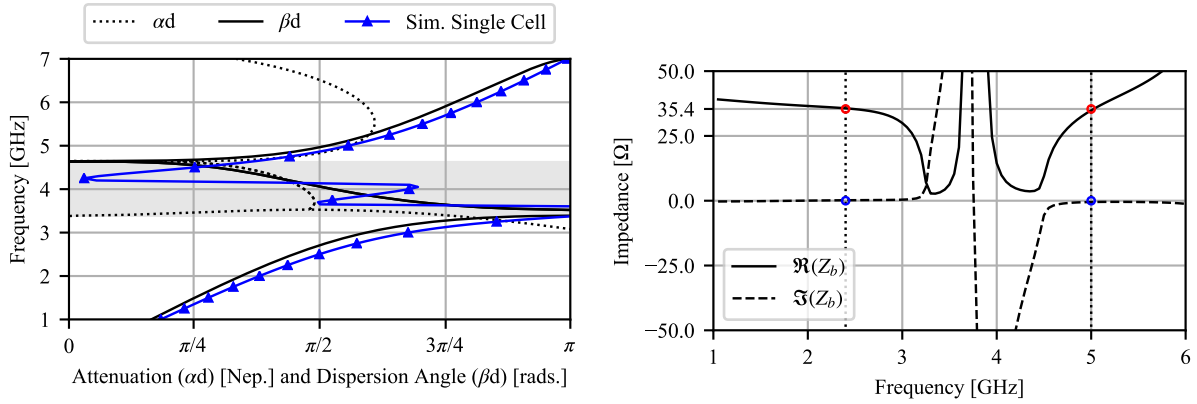

(a) (b)

Figure 3.6: a) Even-mode dispersion data for the MTM-EBG. The bandgap for the coupled MS-CPW mode can be seen as the highlighted region from 3.39 GHz to 4.72 GHz in. The super-imposed line provides the S_{21} phase of a single, fully printed MTM-EBG unit cell. b) Bloch Impedance extracted from a single MTM-EBG. The red and blue circles indicate the desired level of the real and imaginary parts.

was done with the back-to-back impedance transformer, simulations were again performed on the single MTM-EBG unit cell to verify the expected properties. The dispersion of this unit cell, as predicted by the equivalent circuit model, and the phase of a single unit cell is provided in Fig. 3.6(a). The single unit cell is again an excellent representation of the infinite cascade. Any differences between these curves is largely attributed to parasitic effects introduced by the printed elements, and the additional width of the capacitive regions. The Bloch impedance was also evaluated from this single unit cell and is shown in Fig. 3.6(b). This unit cells assumes values of $35.65 + j0.18\ \Omega$ and $34.86 - j0.51\ \Omega$ at 2.4 and 5.0 GHz, respectively, which are very close to the expected value of 35.4 Ω; however, achieving these values required tuning W to 6 mm. The parameters of the power divider were also tuned in order to improve the performance at both operating frequencies; for example, the triangular notch described by the angle θ was found to improve the return-loss performance, particularly at the higher frequency [97].

Figures 3.7(a) and 3.7(b) compare the simulated results of the MTM-EBG-loaded power divider (red triangles pointed up) and a conventional (unloaded) power divider (green triangles pointed left) operating at the intermediate frequency. This was done in order to establish a reference on the basis of the same overall physical size (the triangular notch is included); power dividers designed for either of the operating frequencies would require a different footprint. While not provided in these results, the isolation may be easily inferred from the construction of the power divider in Fig. 3.5. Comparing the red and green curves, it is clear that the MTM-EBG-loaded power divider has comparable insertion loss to the reference structure but significantly better return loss, particularly at 5.0 GHz. The simulated 10-dB fractional (absolute) return-loss bandwidths were determined to be 82.3% (1975 MHz) and 12.0% (600 MHz) around 2.4 and 5.0 GHz, respectively. The losses for both the loaded and unloaded designs are comparable at both operating frequencies. Fig. 3.7(b) provides the port-to-port phase error over a $\pm 10\%$ bandwidth for both the simulated MTM-EBG-loaded

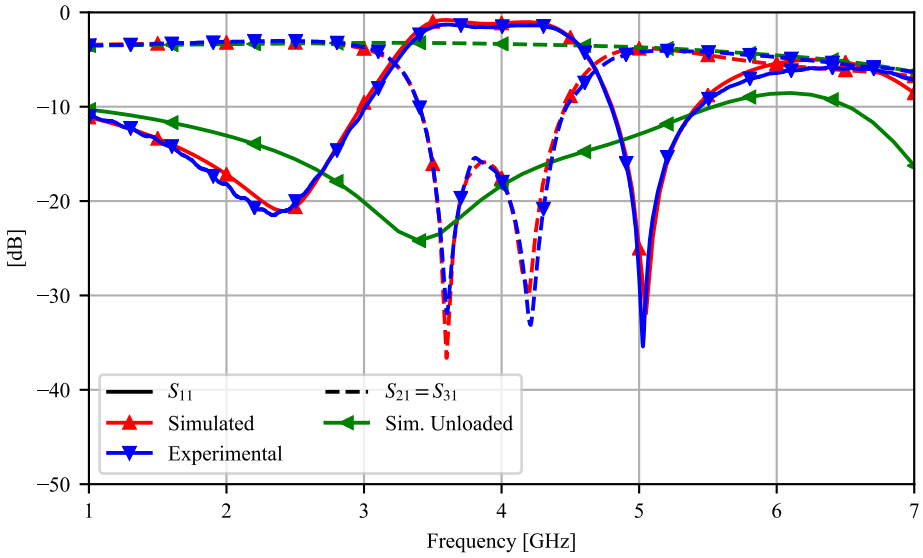

(a)

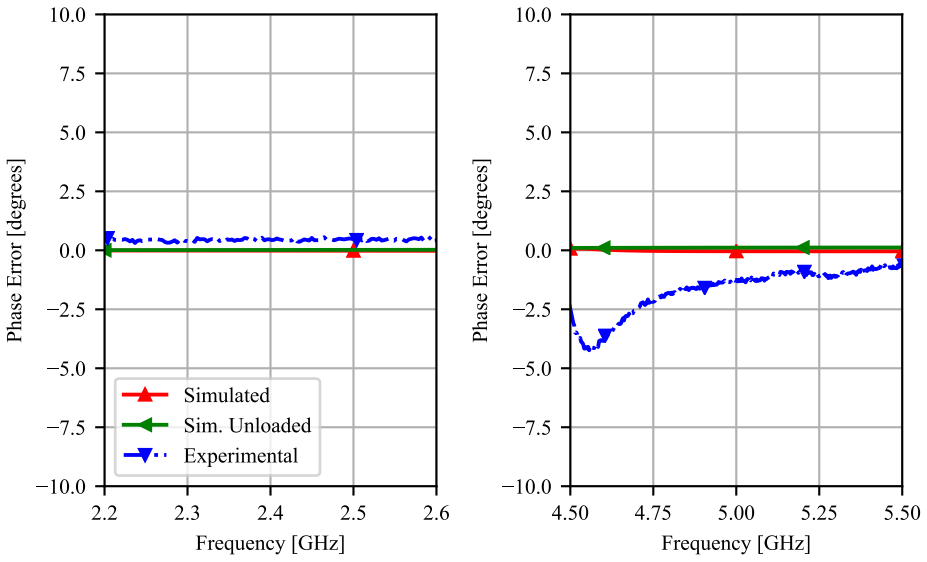

(b)

Figure 3.7: Simulated and experimental scattering parameter magnitudes and phases of the fully printed MTM-EBG-loaded dual-band power divider (a) magnitude and (b) port-to-port phase error ($\angle S_{21} - \angle S_{31}$).

and unloaded power dividers; as expected, these are both approximately zero at the operating frequencies. When compared to a 35.4-Ω conventional MS quarter-wavelength impedance transformer designed for 2.4 GHz [see Fig. 3.8(a)], the MTM-EBG-loaded impedance transformer [see Fig. 3.8(b)] is 30.5% miniaturized, this improvement in performance is significant.

Conversely, the MTM-EBG section appears slightly larger at 5.0 GHz [see Fig. 3.8(c)].

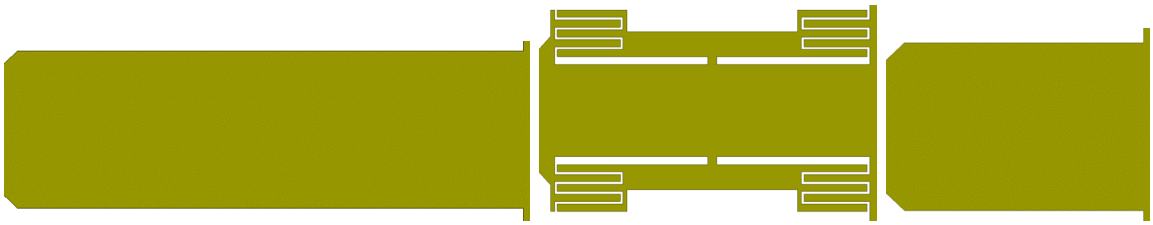

Figure 3.8: Size comparison of the MTM-EBG-loaded transformer to single-band variations: (a) unloaded transformer at 2.4 GHz, (b) MTM-EBG loaded impedance transformer and (c) unloaded transformer at 5.0 GHz.

3.3.2 Comparison to alternate technologies

Table 3.1: Comparison of the embedded MTM-EBG to a variety of dual-band structures reported in recent literature.

	f_f/f_s [GHz]	**Branch Size**
This work	2.4/5.0	0.18 λ_g × 0.09 λ_g
[43]	0.9/1.9	0.15 λ_g × 0.16 λ_g
[45]	2.4/5.8	0.29 λ_g × 0.23 λ_g
[47]	2.0/5.2	0.28 λ_g × 0.14 λ_g*
[53]	2.4/5.2	0.31 λ_g × 0.63 λ_g
[55]	1.32/2.44/3.56/4.68	0.45 λ_g × 0.15 λ_g
[56]	1.5/2.4/3.5/4.2	0.40 λ_g × 0.16 λ_g*

*Exact dimensions were not specified and were inferred visually.

Table 3.1 demonstrates the operating frequencies and relative electrical size of the 35.4 Ω MTM-EBG compared to a variety of other dual-band embedded structures reported in the recent literature. In each case included in Table 3.1, the dual-band structures are fully printed and may be designed for nearly arbitrary impedance values. The branch size in each of the designs included in Table 3.1 refers to the footprint of the element which renders the device dual-band, not the footprint of the actual device as many of the devices examined here were different. This branch size is then compared to the *guided* wavelength of a MS mode at the lower operating frequency, to account for the effect of high-permittivity dielectric substrates on miniaturization, and enable a better comparison (particularly in [53]). As can be seen in

the table, the MTM-EBG is significantly smaller than alternate fully printed structures and occupies only 67% of the area of the next smallest design [43].

The design procedure presented in this work can be easily modified for any desired operating frequencies or impedance level, therefore making the proposed structure flexible to nearly any application. Furthermore, the embedded MTM-EBG can be designed for nearly arbitrary phase at each operating frequency; the design approaches in [43, 45, 53, 55, 56] were limited to a phase response of $\pm 90^{\circ}$ with little discussion on how to operate at alternate phases. Only [47] had a procedure for adjusting the phase response. In addition to the flexibility offered by the embedded-MTM-EBG it also provides a strong, well modelled rejection band for intermediate frequencies; the MTM-EBG design approach is robust enough to enable the intermediate rejection bandwidth and center frequency to be varied over a large range, even as the phase response at both operating frequencies is maintained. An example of this is provided in Fig. 3.9(a) and 3.9(b), which demonstrates the dispersion of two vastly different MTM-EBG unit cells that have identical phase at 2.4 and 5.0 GHz. In comparison, [45] offered effectively no rejection of intermediate frequencies, and [43, 53, 55, 56] had limited discussion on how to control the rejection band; furthermore, it appears that this rejection is directly tied to the operating frequencies. This demonstrates that the MTM-EBG can be used in applications requiring dual-band operating, but flexible rejection and suppression of signals between them.

3.3.3 Experimental Results

The dual-band power divider discussed previously was fabricated using the U3 on Rogers RO4350B substrate (ϵ_r=3.66, tanδ=0.004 and h=1.524 mm) with 35 μm thick electrodeposited copper; the fabricated T-junction power divider is shown in Fig. 3.10 with the inset

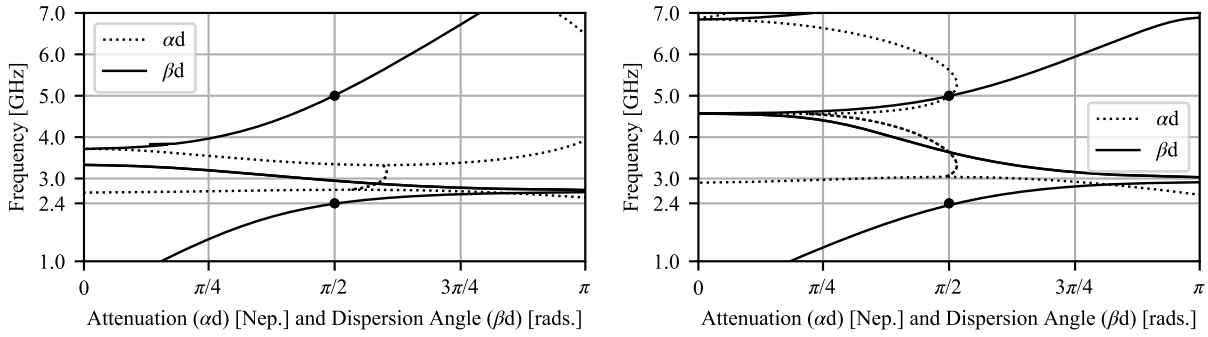

Figure 3.9: Comparison of the dispersion of two unit cells which have identical phase shifts at 2.4 and 5.0 GHz, while having different rejection bands. Both cells: ϵ_r=3.66 and h=1.524 mm. Cell dimensions: a) s=2.2 mm, g=0.6 mm, W=5.6 mm, d=10 mm, C=0.8 pF and L=0.2 nH and b) s=2.4 mm, g=0.3 mm, W=6 mm, d=12 mm, C=0.43 pF and L=0.4 nH.

showing one of the fabricated interdigitated capacitor. Comparing these experimental results (blue triangles pointing down) to the initial simulation results of the MTM-EBG-loaded T-junction power divider, which are presented in Fig. 3.7(a), it is apparent that the results are in excellent agreement. The 10-dB fractional (absolute) return-loss bandwidths were determined to be 83.7% (2010 MHz) and 12.6% (630 MHz) around 2.4 GHz and 5.0 GHz respectively. Nevertheless, it is important to acknowledge the discrepancies, however minor: first, it is evident that the return-loss peak in the lower operating band has shifted by 2.1% from 2.4 GHz to 2.35 GHz; second some additional loss has been incurred throughout the bandgap and at the upper operating frequency, increasing the insertion loss in experiment to 4.19 dB from 3.84 dB in experiment. While not as pronounced in the back-to-back transformer, past fabrications using this laser-milling system on this substrate have found that the dielectric-laser interaction can introduce some loss if the substrate is burned. Studies performed in HFSS have found that if this burning occurs within the capacitive interdigitations, the losses will be far more pronounced. As is apparent in the inset of Fig. 3.10, there is minor scorching along the edges of the capacitive interdigitations which appears as a build-up of dark material. It is believed that this build-up is formed when ejected copper particles are

trapped by the melting dielectric and are not successfully removed. The small feature size of these interdigitations make it impractical to attempt to physically clean, without severely damaging the features and further altering the results. In addition to this insertion loss, it is apparent from Fig. 3.7(b) that a small phase error has been introduced at both operating points. It was measured to be 0.47 degrees at 2.4 GHz and -1.25 degrees at 5.0 GHz and while small appears to have been introduced by minor defects in the individual capacitors.

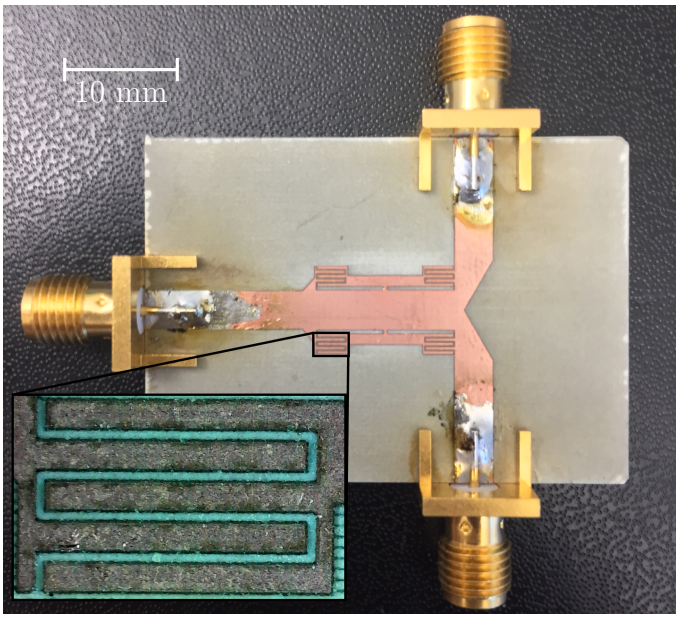

Figure 3.10: Fabricated dual-band power divider; inset: fabricated capacitors and scale.

3.4 Corporate Feed Network

3.4.1 Initial Design Challenges

As an initial design, the dual-band power divider discussed in Sec. 3.3 was expanded into a corporate feed network by connecting additional dual-band power dividers directly to the output of another. The resulting schematic is provided in Fig. 3.11 with the exact MTM-EBG dimensions provided in Fig. 3.5. This device was again fabricated using the Protolaser

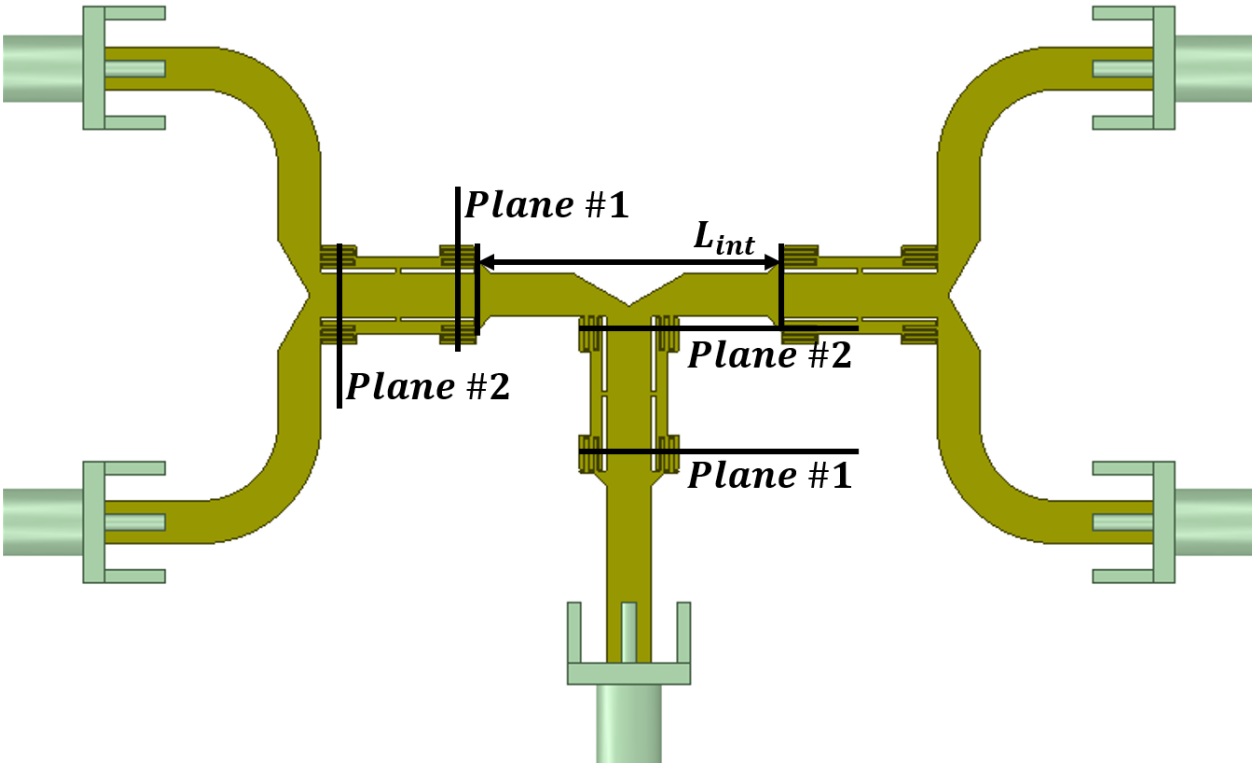

Figure 3.11: Initial layout of a corporate feed network. Plane references indicate where the current distributions were extracted.

LPKF U3, but it was determined that this device did not function as well as intended. First, when compared to an identical network without MTM-EBG loading, it had worse return loss performance; some increase in insertion loss was expected due to the mechanism behind the operation of the MTM-EBG. Second, and more importantly, the port-to-port phase error was unacceptable high in simulation and made worse in the experimental results. Both of these issues are clear from the experimental and simulation results shown in Figs. 3.12(a) and 3.12(b).

It is clear in Fig. 3.12(a) that the MTM-EBG-loaded corporate feed network performed worse than the unloaded network, particularly due its unusually broadband performance. This was identified as being a result of the short intermediate distance L_{int} that was used to connect

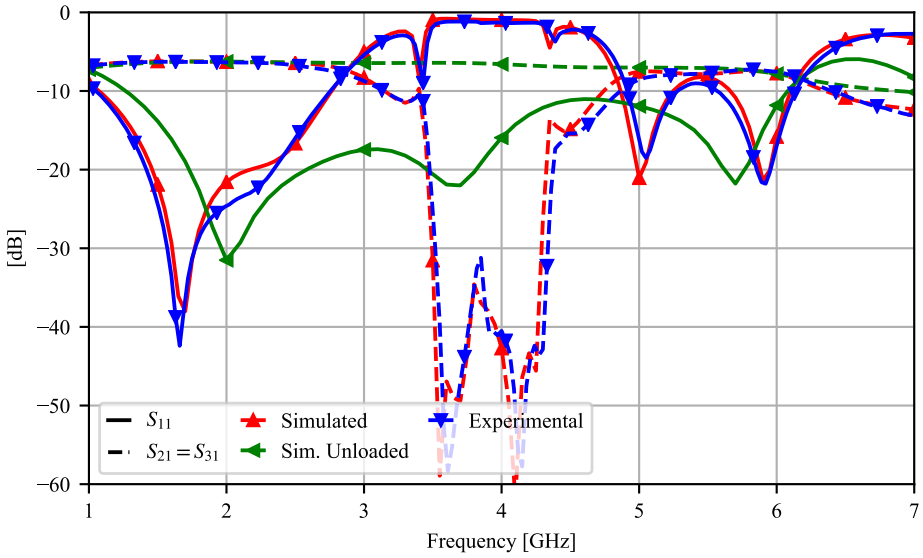

(a)

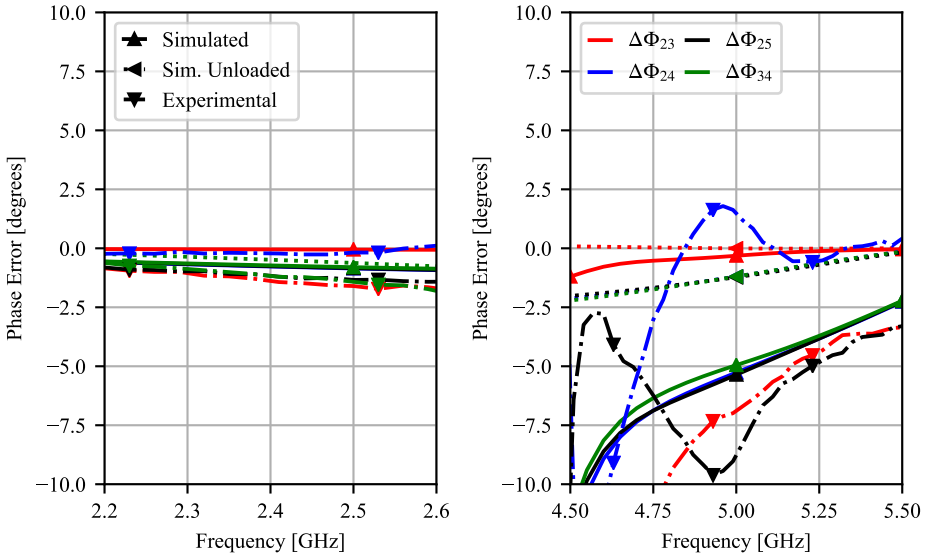

(b)

Figure 3.12: Experimental and simulation results for the initial dual-band corporate feed network design: a) Scattering parameter magnitudes, including a simulated unloaded network and b) port-to-port phase error ($\Delta\phi_{ij} = \angle S_{i1} - \angle S_{j1}$).

the second stage transformers to the input. As a result of this short distance, the unloaded corporate feed network can be viewed as a multi-section impedance transformer which are well known to be broadband [40, 41]. However, in this case the additional parasitics of the junctions strongly degraded the performance of the unloaded network; this translated to an

equal, if not more pronounced degradation in the MTM-EBG-loaded network. Parametric studies found that by increasing the intermediate length L_{int} could improve the performance of the MTM-EBG-loaded network at both operating points, while decreasing the bandwidth of the unloaded design. Given the current layout, increasing this distance would make the proposed network less practical and less suited to antenna applications; the layout was modified to both account for a long intermediate distance and improving the applicability of the network to antenna applications.

Another issue with this design was the high phase error observed at the high frequency operating point. The initial specifications for this network were an identical phase and magnitude at each of the output ports; Fig. 3.12(b) indicates this was not accomplished. While the phase-error over the lower band is acceptable, the phase error at the higher frequency is not and reaches nearly 5°; this is made worse in fabrication and reaches nearly 10°. Since this error was found in simulation, it indicates it was an issue with the design rather than the fabrication as the single stage divider had no error in simulation (see Fig. 3.7(b)). It was then identified that this error was associated to a sensitivity of the MTM-EBG to current imbalances.

For a conventional MS TL any discontinuity will disturb the current distribution by changing the phase incurred by currents on the conductor edges. While normally not a pronounced issue in MS devices, this can seriously degrade the performance of the MTM-EBG as it can supports an odd-mode which is excited by these imbalances. Discussed in Chapter 2, the CBCPW host network supports three distinct quasi-TEM modes; two even-modes and an odd CSL mode. To verify the presence of this odd-mode, the currents on the ground plane directly below select reference points of the MTM-EBG were examined (see Fig. 3.11). The ground plane was examined as the interdigitations made it difficult to identify any imbalances without increasing the size and convergence of the simulation. These current

distributions were then normalized to their respective maximum values and compared to currents extracted at the same locations for the single stage power divider; these results are shown in Figs. 3.13(a) and 3.13(a).

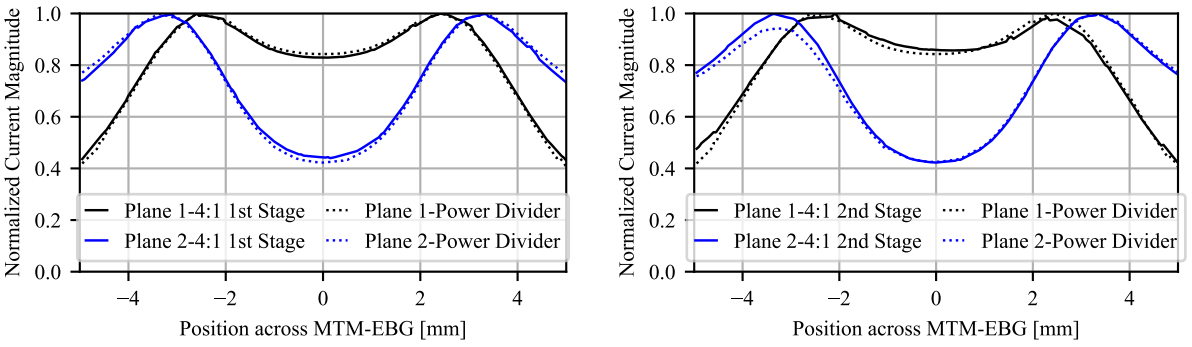

(a) (b)

Figure 3.13: Simulated current magnitudes accross the transverse plane of an MTM-EBG. Normalized current profiles at a) the first stage transformer and b) the second stage transformer.

The first stage of the corporate power divider has a current profile identical to that of the power divider. However, the profiles of the second stage clearly differ from that of the single stage divider; not only are they different, but the distribution for the corporate power divider is clearly asymmetric. Such a current profile is only possible if an odd mode was excited on the MTM-EBG. Typically for MTL networks, such as a CBCPW, these parasitic modes would be suppressed through the use of bonding wires or grounding vias [90]; this also suppresses the PPW-like mode so such a solution could not be employed for the MTM-EBG. Instead, to mitigate the propagation of the odd-mode the input to these second stage transformers can be tapered to cause a more uniform current distribution at the input of the second stage transformers.

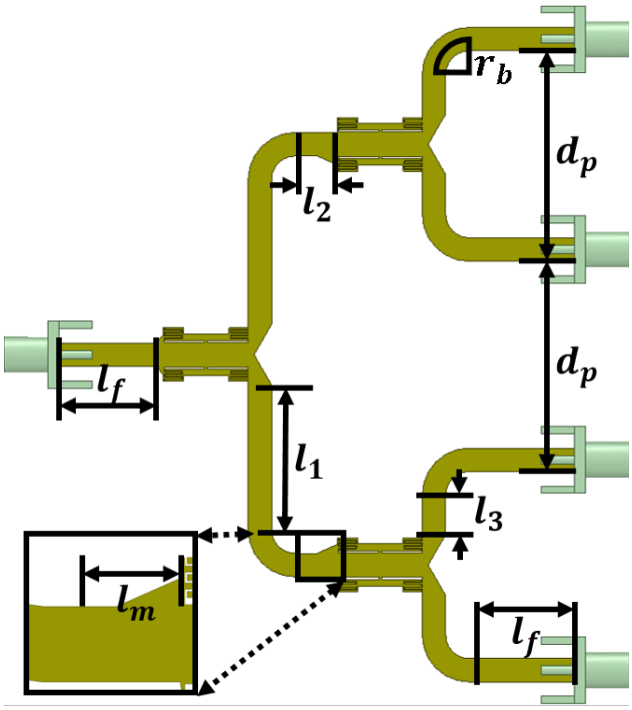

Figure 3.14: Circuit layout and dimensions for the final 4:1 power divider including an inset of the asymmetric taper. See Fig. 3.5 for exact MTM-EBG dimensions: a=5 mm, d=30 mm, l_1=25 mm, l_2=5 mm, l_3=10 mm, l_f=15 mm, l_m=3 mm, d_p=30 mm, r_b=6 mm.

3.4.2 Design and Simulation

Based on the challenges discovered in the design of the corporate feed network in Section 3.4.1, a new corporate feed layout was adopted which is not only more practical for antenna array applications but also has better performance. The revised corporate feed network was designed with a fixed port-to-port distance d_p of 30 mm. This revised layout is shown in Fig. 3.14. In this design the intermediate length L_{int} is made up of l_1, l_2 and the MS bend of radius r_b=6 mm. These dimensions, and l_3, were tuned to maximize the performance at both operating frequencies. Since these dimensions reduced the bandwidth of an unloaded network operating at the intermediate frequency, a comparison was made to unloaded networks designed for the operating frequencies under the constraint that they have identical footprints and identical port-to-port distances d_p. This was accomplished by modifying l_2 and l_f, and varying d for each transformer segment (see Fig. 3.5) to adjust the operating

Table 3.2: Comparison of the simulated MTM-EBG corporate feed to the individual single frequency unloaded designs with identical total footprint, where $\Delta\phi_{ij} = \angle S_{i1} - \angle S_{j1}$.

	Unloaded		**MTM-EBG**	
Parameter	@ 2.4GHz	@ 5.0GHz	**@ 2.4GHz**	**@ 5.0GHz**
$S11$ [dB]	-30.6	-21.1	**-30.0**	**-25.2**
$S21$ [dB]	-6.28	-7.18	**-6.35**	**-7.50**
$S31$ [dB]	-6.32	-7.36	**-6.36**	**-7.48**
$\Delta\phi_{23}$ [deg.]	0.42	-0.54	**0.67**	**0.43**
$\Delta\phi_{24}$ [deg.]	0.31	-0.61	**0.76**	**0.14**
$\Delta\phi_{25}$ [deg.]	0.03	0.00	**0.11**	**-0.04**
$\Delta\phi_{34}$ [deg.]	-0.11	-0.07	**0.08**	**-0.29**

frequency. A comparison of the simulation results of these structures is provided in Table 3.2, where symmetry enforces $S_{21} = S_{51}$ and $S_{31} = S_{41}$.

In addition to the modified layout, a small asymmetric taper was added to the input of the second stage transformers in order to suppress the excitation of the odd CSL-like mode and, therefore reduce the port-to-port phase error $\Delta\phi_{ij}$. This asymmetry is shown in the inset of Fig. 3.14; as a result, the port-to-port phase errors are reduced to levels comparable to an unloaded structure operating at 5.0 GHz. It is clear from Table 3.2 that, with these modifications, the MTM-EBG-loaded 4:1 corporate feed network has comparable or superior performance at each operating frequency compared to the single-frequency networks, indicating that the MTM-EBG-loaded device is a suitable replacement for either unloaded reference structure.

Figure 3.15(a) provides the full range of simulated scattering-parameter data for the designed 4:1 feed network shown in the solid lines. As the network is symmetric between ports 2 (3) and 5 (4), only partial scattering-parameter results have been provided. As is apparent from Fig. 3.15(a), the MTM-EBG-loaded 4:1 corporate feed network has excellent performance about each of its desired operating points, with the simulated 10-dB fractional (absolute) return-loss bandwidths of 48.7% (1168 MHz) and 11.3% (565 MHz) around 2.4 and 5.0 GHz, respectively. Similar to what was provided for the single stage divider, Fig. 3.15(b) provides

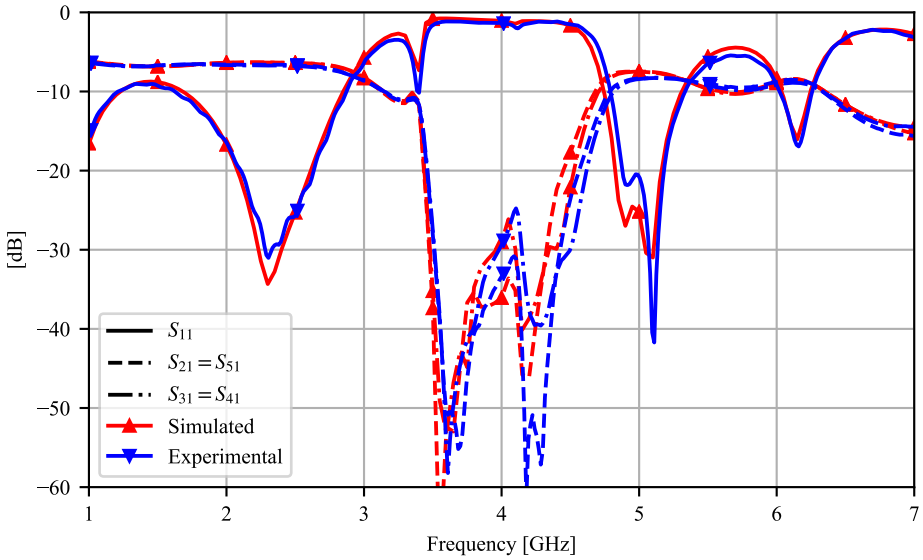

(a)

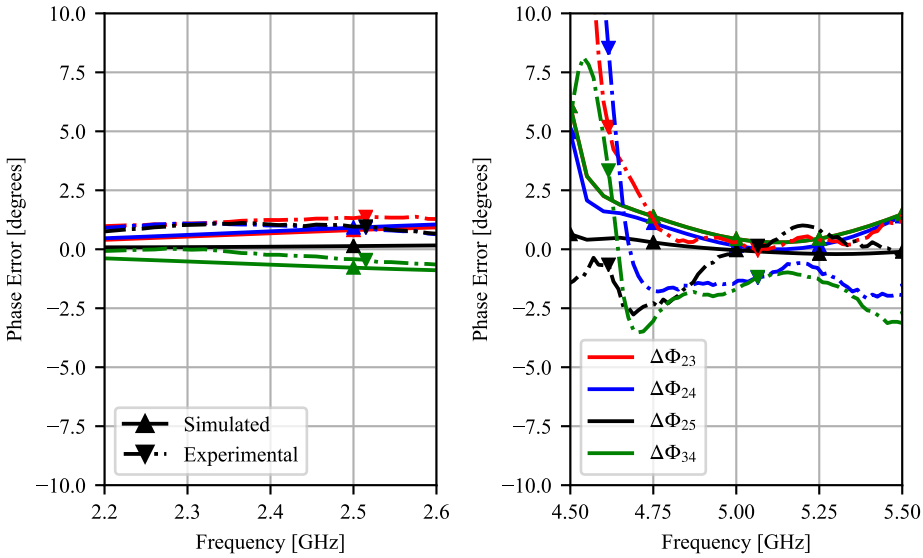

(b)

Figure 3.15: Simulated and experimental scattering-parameter results for the fully printed MTM-EBG-loaded corporate feed network: (a) magnitude and (b) port-to-port phase error $\Delta\phi_{ij} = \angle S_{i1} - \angle S_{j1}$.

$\Delta\phi_{ij}$ around a $\pm 10\%$ bandwidth at each operating point. It should be observed that the port-to-port phase error is not constant and generally not zero; this is largely due to previously mentioned sensitivities of the MTM-EBG to current imbalances. Nevertheless, at the operating frequencies, the phase error remains relatively low.

3.4.3 Experimental Results

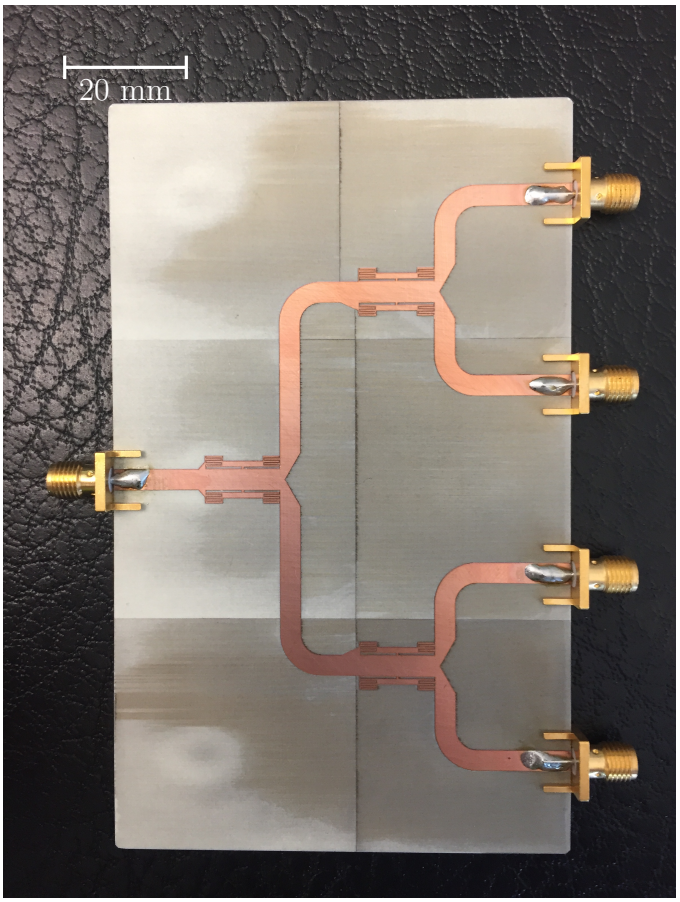

Figure 3.16: Fabricated dual-band corporate feed.

The 4:1 corporate feed network previously was also fabricated and measured using the same process as discussed in Sections 3.2 and 3.3. The fabricated sample is shown in Fig. 3.16; while it appears as though there is some discoloration of the underlying dielectric, the substrate has not been burned and therefore this does not have any effect on the overall performance. As presented in Fig. 3.15(a) and 3.15(b), the experimental results (dotted curves) are, once again, in excellent agreement with the simulated results (solid curves) with the exception of marginally higher insertion losses. At 2.4 GHz, S_{11}, S_{21} and S_{31} were found -29.01, -6.61 and -6.72 dB respectively; at 5.0 GHz the same values were found to be -20.95, -8.31 and -8.38 dB, respectively. The experimental 10-dB fractional (absolute) return-loss bandwidths were determined to 52.0% (1248 MHz) and 10.8% (542 MHz) about 2.4 and

5.0 GHz respectively. These, too, are in excellent agreement with the simulated results.

The overall performance at 5.0 GHz is marginally worse compared to the simulated design, both in return and insertion loss. The additional insertion loss is attributed to the laser-induced burning within the interdigitated capacitors, which was not modeled and which is similar to what was observed with the single-stage design. The experimental and simulated port-to-port phase errors $\Delta\phi_{ij}$ as shown in Fig. 3.15(b) are in excellent agreement at the design frequencies, with $\Delta\phi_{23}$, $\Delta\phi_{24}$, $\Delta\phi_{25}$, and $\Delta\phi_{34}$ equal to 1.23, 1.01, 1.06 and -0.23 degrees at 2.4 GHz, and 0.32, -1.33, -0.07 and -1.65 degrees at 5.0 GHz. In addition, these phase errors are comparable to what was observed in the fabricated MTM-EBG single stage power divider indicating that the error is related to a defect between the individual capacitors. Finally, it should be noted that the observed phase errors, if applied to a four-element antenna array fed by the proposed 4:1 feed network, would result in less than 0.25 degrees of main-beam tilt with very little, if any, effect on the 3-dB beamwidths.

Chapter 4

Mechanically Tunable MTM-EBG-based Microstrip Filters

4.1 Motivation

Mechanically tunable filters, such as those presented in [84–86], are better suited to high power applications as they suffer from none of the non-linearities that can arise in semiconductor-based tuning schemes [79, 81]. In addition, they are significantly less challenging to fabricate than MEMS-based capacitors [80, 83]. Due to the requirements and the maneuverability necessary to realize mechanical tunability, they are typically reserved for larger 3D cavity based filters. MTM-based tunable filters have also been proposed, but rely on varactor components to enable the tunability. They also require a large number of unit cells to realize the desired response, while suffering from variations in the passband performance. Due to the planar and fully printable nature of the MTM-EBG, as well as the ease of modelling through equivalent circuit, it is well suited for tunability. It is also possible to realize a fully mechanical tuning scheme with the MTM-EBG.

An application where both the tunability and filtering offered by the embedded MTM-EBG is useful is in TV Whitespace spectrum telecommunications. TV Whitespace refers to the

frequency spectrum that was previously allocated for television signals, but has since been rendered obsolete with the introduction of digital TV. This spectrum has since been repurposed for non-broadcasting applications under the restriction that these transmissions do not interfere with existing licensed broadcasters [98]. Due to the properties of this band, it has increased range and comparatively large operating bandwidths making it attractive to telecommunication applications. However, due to the sporadic nature of existing licensed broadcasters, filters to suppress transmission in these bands are necessary. A filter which is simultaneously tunable would greatly reduce the number of filters and allow for greater flexibility in implementation.

4.1.1 Objectives

This chapter will first demonstrate the feasability of the MTM-EBG to create a highly compact tunable MS bandstop filter based on the MTM-EBG with a constant ABW. This is demonstrated in a filter design with fewer unit cells and a reduced tuning range. Mechanical tuning is realized by placing a dielectric plate directly on the surface of the MTM-EBG and varying its relative position across the capacitive regions of the MTM-EBG. The constant ABW is then engineered by using an effective plate permittivity that differs slightly for each cell to asynchronously tune the response of each individual MTM-EBG unit cell; as demonstrated in Chapter 2, this compensates for bandwidth changes introduced by the tuning. These individual plates are then combined into a single tuning element to facilitate a simplified tuning set-up. The resulting structure is demonstrated to have excellent performance, comparable to 3D tunable filters, while being fully uniplanar and highly compact. Per a recommendation by our industrial sponsors KP Performance Antennas and Infinite Electronics Group, the tunable filter is then modified to operate over the full TV Whitespace spectrum with a constant ABW; specifically, from 470-700 MHz with an ABW of 35 MHz. In order to

meet this specification while ensuring good passband performance, additional unit cells were necessary and required certain asymmetries to ensure reasonable passband performance.

4.1.2 Outline

This chapter is organized as follows; Section 4.2 discusses the design, simulation and experimental results of an intial fixed-frequency MTM-EBG-based MS bandstop filter with an ABW of 225 MHz centered at 4.18 GHz using three unit cells. Section 4.3 discusses the mechanism behind the mechanical tunability, and discusses the design of the tunable plate to realize a constant ABW. Simulated and experimental results of the fabricated tunable filter are then discussed, which is tunable in simulation from 3.5 to 4.1 GHz with a constant ABW of approximately 220 MHz, and compares the experimental performance to that of tunable filters in recent literature. Section 4.4 details the modifications and design changes necessary to realize the performance over the TV Whitespace spectrum, where a fixed-frequency design centered at 804.2 MHz and 10-dB ABW of 37.4 MHz is presented. The tuning range is met by using a plate of permittivity ϵ_p=10.2, with accomplishes a tuning range of 52.3% and a constant ABW of 32.7±4.6 MHZ. Aspects of this chapter have been submitted to the IEEE Journal of Microwave Theory and Techniques, and are currently under review.

4.2 MTM-EBG-Based Microstrip Bandstop Filter

In this section, an MTM-EBG-based 225 MHz bandstop filter centered at 4.18 GHz will be realized on Rogers 4350B (ϵ_r=3.66 and tanδ=0.004) with a thickness of 1.524 mm. To simplify both the requirements on the simulation model and fabrication, the minimum feature size was selected to be 200 μm. Due to the strict requirements of the bandgap, the procedure outlined in Appendix B is used to more precisely design the loading. This further

incorporates the parametric studies outlined in Table 2.1 to help guide the design of the host medium.

4.2.1 Design

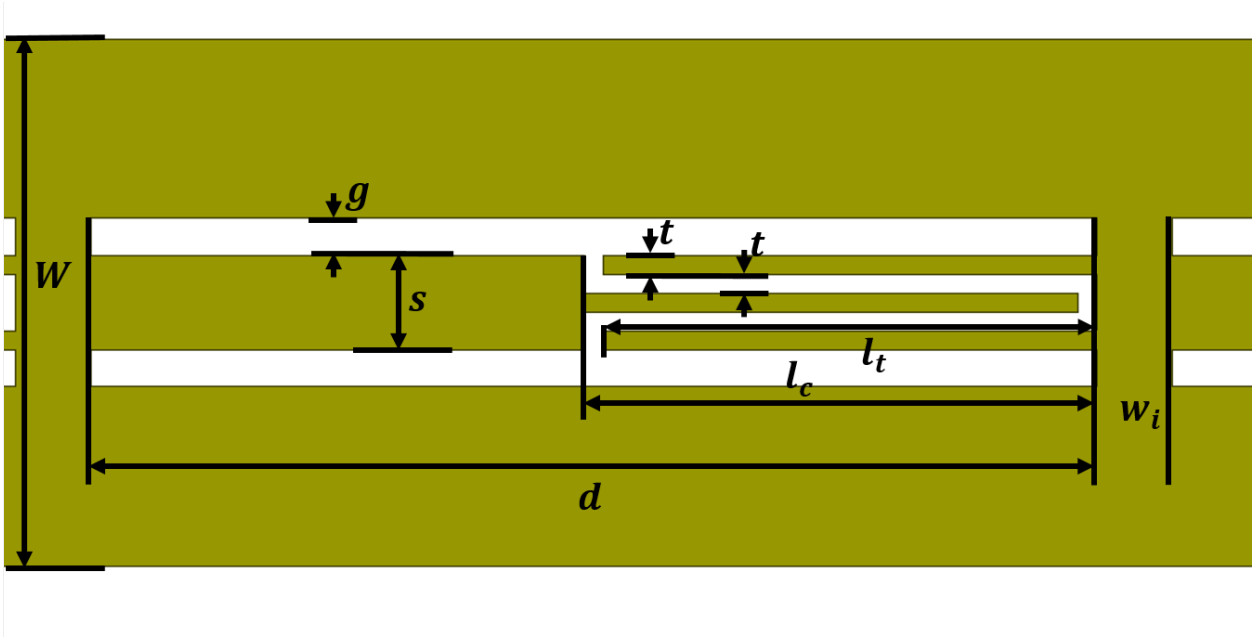

Figure 4.1: Schematic and dimensions of the individual fully printed MTM-EBG unit cell with an interdigitated capacitor: W=5.6 mm, d=10.7 mm, s=1.0 mm, g=0.4 mm, t=200 μm, l_c=5.45 mm, l_t=5.25 mm, w_i=0.8 mm.

Since the bandgap was desired to be centered at 4.18 GHz with a bandwidth of 225 MHz, the procedure outlined in Appendix B can be used to determine the necessary loading given the desired f_X and f_Γ of 4.09 and 4.31 GHz. In order to do this, however, the host medium must first be determined. To maximize the physical tuning range, the length was first selected to be 11.5 mm. This permitted the use of smaller capacitance values that could be easily realized with the small feature size. While this length is on the order of a quarter-wavelength, this was selected based on the application of the tunability and could be substantially miniaturized simple by increasing the capacitance.

Based on the discussion in Chapter 2 and the trends described in Table 2.2(b), a small CPW stripline width (s) will result in a smaller bandwidth. In this application the minimum s is restricted to the width of an interdigitated capacitor with three 200-μm fingers and two 200-μm gaps, for a total of 1 mm. With this limitation of s and a characteristic impedance of 50 Ω, a capacitance (0.35 pF) that results in f_Γ=4.31 GHz would require a negative inductance to make f_X=4.09 GHz, which is obviously unrealizable. As demonstrated in Table 2.2(b), the bandwidth can also be reduced by increasing the width of the MTM-EBG, and, in turn, reducing the characteristic impedance. Setting the width to 5.6 mm, and the characteristic impedance to 35.4 Ω, allows for both small and realizable loading values; based on Appendix B, these values were determined to be C=0.3 pF and L=0.08 nH. These loading values were realized using interdigitated capacitors and strip inductors of width w_i; this inductance was evaluated to be L=0.083 nH [91]. After tuning to account for parasitic junction effects, the final dimensions of the individual unit cells are provided in Fig. 4.1. It is worthwhile to note that the extraction of the equivalent series capacitance of the final interdigitated capacitor design has a value between 0.24 and 0.28 pF over the full frequency range [92]. This indicates that the proposed analytical approach is an excellent starting point for the design of the MTM-EBG.

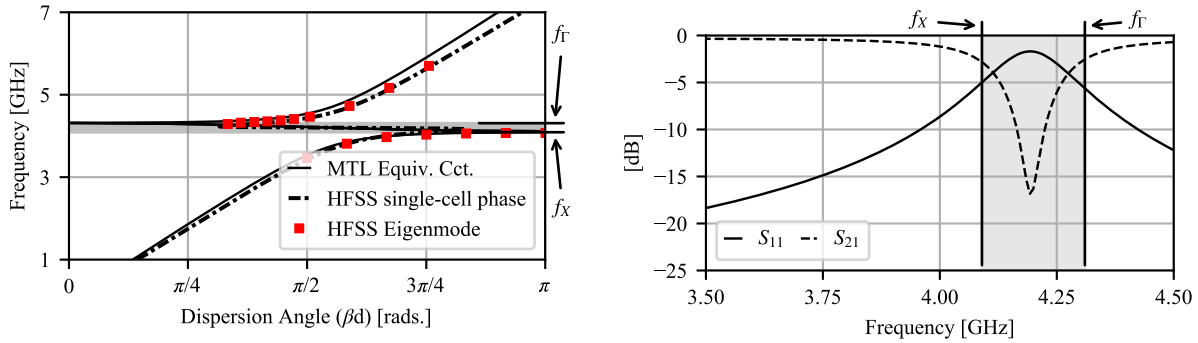

(a) (b)

Figure 4.2: a) Dispersion diagram from the equivalent circuit model compared to the phase of a single unit cell and corresponding eigenmode simulations. b) Scattering parameter magnitude response of a single unit cell. The shaded region in each represents the bandgap predicted by the equivalent circuit model and is calculated as 220 MHz from the f_X to f_Γ.

To further demonstrate the validity of using a finite number of unit cells and the accuracy of the equivalent circuit model, a unit cell of identical geometry to what was provided in Fig. 4.1 was simulated as embedded in a 35.4 Ω TL and de-embedded to the start of the MTM-EBG. The phase response (dash-dotted) of this single unit cell has been plotted against the MTL dispersion data (solid) for the same unit cell in Fig. 4.2(a). Minor differences exist between the simulated response of the single unit cell and the dispersion predicted by the equivalent circuit model, but this is primarily attributed to the presence of fully printed features in the simulated model, which are treated by the equivalent circuit model as fully lumped. An eigenmode simulation was performed in Ansys HFSS (red squares) using the fully printed unit cell and these results demonstrate that the phase response of a single unit cell is an excellent representation of an infinite cascade of unit cells with the exception of within the bandgap itself. However, as discussed in Chapters 2 and 3, this is not a concern as it is difficult to assign meaning to the phase within this region, and this behavior is better captured in the magnitude response of the single unit cell which is shown in Fig. 4.2(b). While the stop-band bandwidth of this single unit cell appears narrower than that of the infinite array, it does occur very close to the expected frequency. In fact, increasing the number of unit cells in the simulation domain will in turn increase the bandwidth of the stop-band to better approximate the infinite cascade. The number of unit cells was therefore selected to increase the 10-dB rejection ABW to 225 MHz. The schematic for the resulting three-cell MTM-EBG-based bandstop filter, with all relevant dimensions and SMA connectors included, is provided in Fig. 4.3. Since the individual unit cells were designed for 35.4 Ω, these were matched to a 50 Ω input using a taper of length L_t.

It should also be noted that due to the mechanism that is ultimately employed to compensate for changes in the ABW, it was found that at least three unit cells were necessary to ensure a minimum of 15 dB of rejection over the full tuning range. Using fewer unit cells would result in the rejection band splitting when fully down-tuned, leading to less than 10-dB of

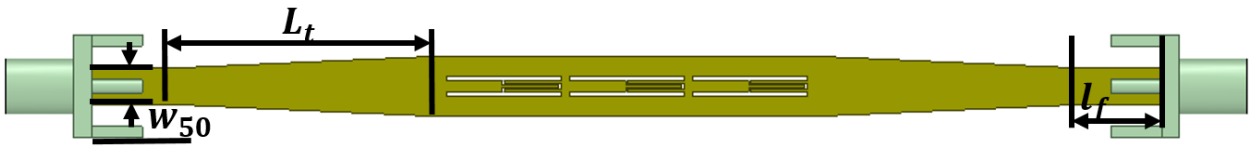

Figure 4.3: Dimensions of the three cell MTM-EBG-based bandstop filter: w_{50}=3.36 mm, L_t=25 mm, l_f=7.35 mm. See Fig. 4.1 for exact dimensions of the individual MTM-EBG unit cells.

rejection in parts of the band. More unit cells could also have been added, but this would have resulted in a more complicated design procedure for the dielectric plate used in Section 4.3.

4.2.2 Simulation and Experimental Results

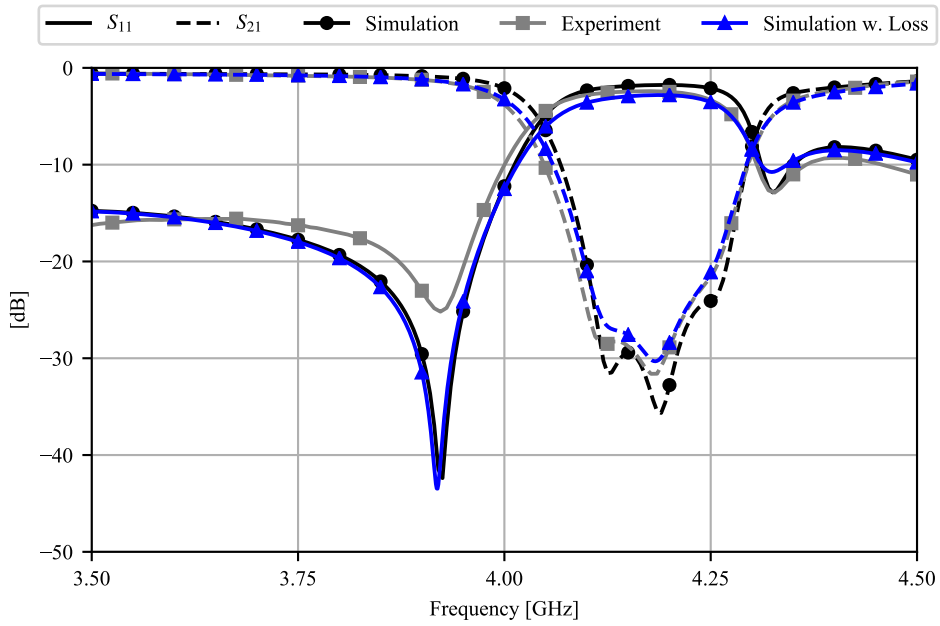

Figure 4.4: Simulation and experimental results for the fixed frequency MTM-EBG-based bandstop filter.

The MTM-EBG-based MS bandstop filter was simulated in HFSS and the simulated scat-

tering parameters (circle markers) are shown in Fig. 4.4. This structure, as shown in Fig. 4.5, was then fabricated in-house using a LPKF ProtoLaser U3 laser milling system and the experimental results (square markers) are provided once again in Fig. 4.4. Generally, the fabrication results are in excellent agreement with the simulated data; however it is apparent that some additional loss has been introduced during the fabrication. As a result, both the peak return loss of the rejection band and the 10-dB bandwidth increased, the latter increasing from 225 MHz to 247 MHz. As was demonstrated in Chapter 3, the additional losses could be better accounted for by filling the interdigitated capacitors with a lossy medium (ϵ_r=1 and tanδ=0.1) modelling residues from the laser-milling process; this largely accounts for the observed increase in ABW. Any further disagreements between the experimental and simulated data are attributed to minor fabrication defects that introduce asymmetries between the individual unit cells. Typically, these are within the tolerances for laser-based milling.

4.3 Tunable MTM-EBG-Based Microstrip Bandstop Filter

4.3.1 Variable-Position Dielectric Plate

As discussed in Section 2.3.1, the response of the MTM-EBG is very sensitive to changes in the loading capacitance. Due to concerns over the effect of non-linearities in conventional tuning mechanisms, this tuning is accomplished by mechanically changing the position of a dielectric plate placed directly on top of a fully printed MTM-EBG. An example of this configuration is shown in Fig. 4.6, which is only possible due to the planar nature of the MTM-EBG. In order to properly evaluate the feasibility of the proposed approach, a single

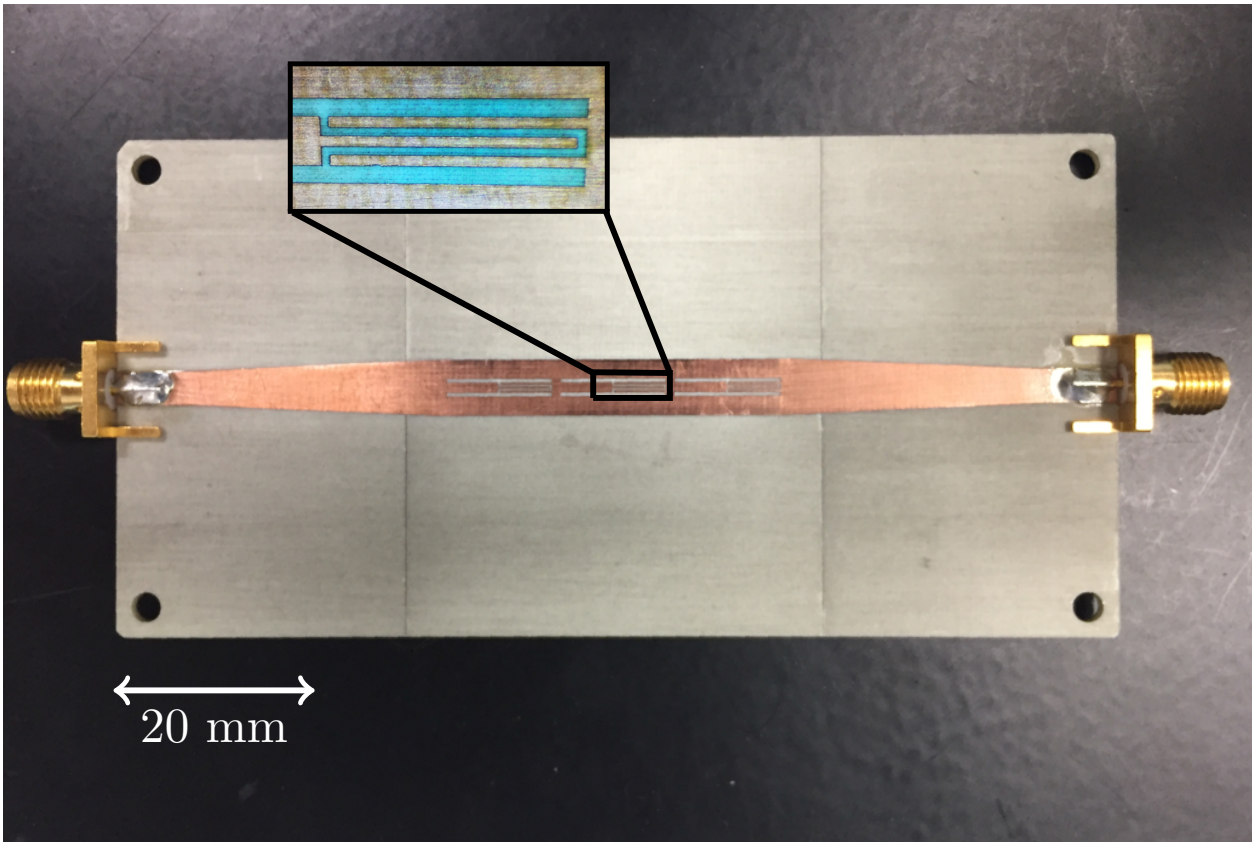

Figure 4.5: Fabricated MTM-EBG-based bandstop filter, with insets highlighting one of the interdigitated capacitors.

MTM-EBG unit cell was used, which was designed in Section 4.2 and shown in Fig. 4.1. The dispersion and magnitude response of this single cell is provided in Figs. 4.2(a) and 4.2(b) respectively. A dielectric plate of height h_p=1 mm and permittivity ϵ_p is then placed directly on top of this single unit cell, as shown in Fig. 4.6, and simulated for various values of the displacement X. The center frequency and 3-dB transmission bandwidths can then be calculated and plotted versus this displacement; these results are shown in Figs. 4.7(a) and 4.7(b). As X increases, the ratio of air to dielectric above the capacitor increases thereby reducing the effective permittivity seen by the interdigitated capacitor. This in turn reduces the capacitance of the MTM-EBG unit cell, and causes the center frequency to increase. Small changes in ϵ_p cause the slope of the center frequency curve to shift. For the same change in X, however, the 3-dB transmission bandwidth similarly increases; small differences in the

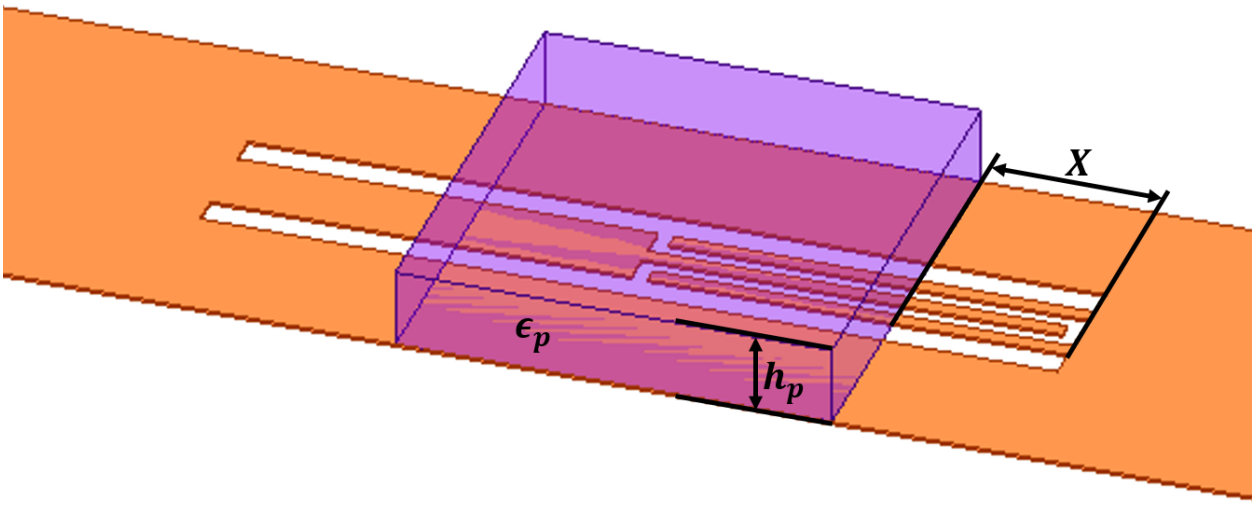

Figure 4.6: 3D view showing the position of a dielectric plate of thickness h_p placed above the printed MTM-EBG unit cell and the displacement X.

permittivity of the plate have a similar effect to what is observed for the center frequency. A similar study was performed on h_p, but found that there was an insignificant difference between responses for realistic values (between 0.5 mm and 1.5 mm). Therefore, these results have not been included.

To compensate for these changes in ABW the mechanism discussed in Section 2.3.1 will be used here and implemented into a *single* tuning element using the dielectric plate tuning method. By designing the ϵ_p to be slightly different above each unit cell used in the bandstop filter, the response of each unit cell can be slightly detuned from one another at full coverage to precisely compensate for the change in the ABW. However in order to maintain the constant ABW, very small differences in plate permittivity are required between the unit cells. It was determined that this difference would be best accomplished by introducing periodic perforations to precisely control the effective ϵ_p of each plate, particularly by changing the

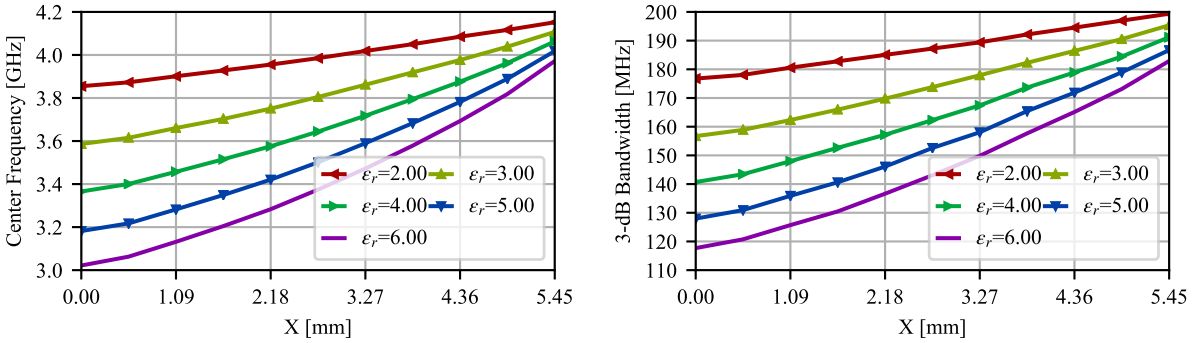

(a) (b)

Figure 4.7: Effect of the dielectric plate displacement on a) the center frequency and b) the 3-dB rejection bandwidth of a single MTM-EBG unit cell, for different values of ϵ_p.

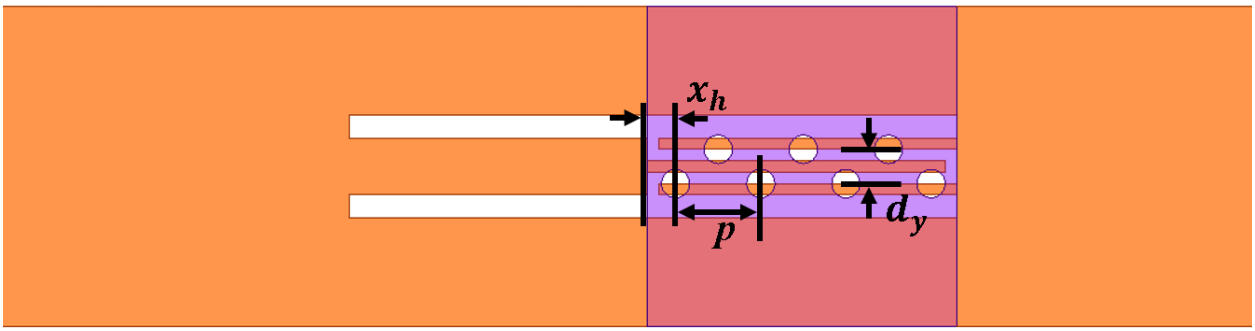

Figure 4.8: Simulation set-up used to evaluate the effect of the spacing of the dielectric perforations: p=1.5 mm, d_y=0.6 mm, x_h=0.4 mm, h_p=1 mm and ϵ_p=3.66.

period (p) and offset (d_y) of the perforations; these are indicated in Fig. 4.8.

Parametric studies were performed on p and d_y using the model shown in Fig. 4.8 with the base parameters provided in the caption; the dimensions of the underlying MTM-EBG unit cell are provided in Fig. 4.1. The center frequency behavior of these parametric studies are shown in Figs. 4.9(a) and 4.9(b). It is apparent from Fig. 4.9(a) that changes in p can introduce a substantial change in the center frequency response, but only for a densely spaced array of perforations. By distinct contrast, small changes in d_y can produce a large changes in the response, particularly for small values of X. Simultaneously varying these

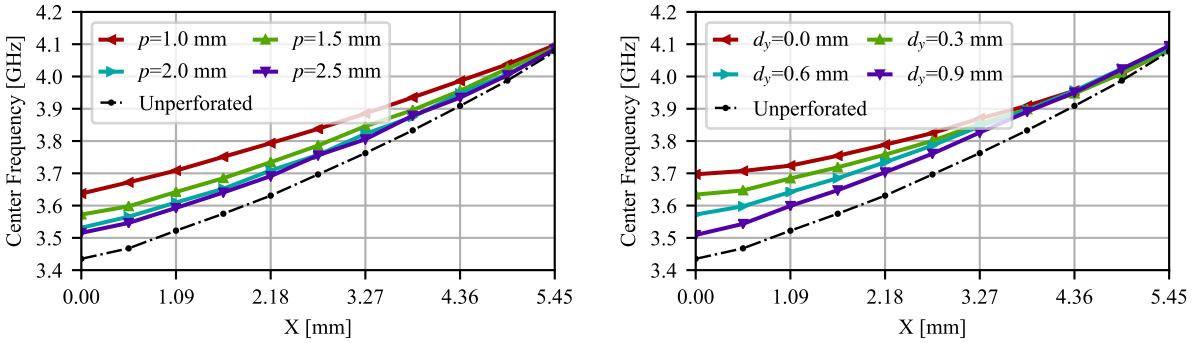

(a) (b)

Figure 4.9: Parametric studies on the effect of: a) period (p), and b) perforation offset (d_y).

parameters can be used to realize nearly any center frequency response versus displacement, and similarly can be used to realize an arbitrary bandwidth response of the filter. The effect of these parameters on the bandwidth has not been included here, as it can be predicted based off the center frequency curves and results in Fig. 2.10.

The proposed method is reminiscent of non-synchronous tuning, which was proposed in [99] and used in [86]; a major difference between these methods is the proposed technique can be realized using a *single* tuning element, greatly reducing the complexity of the tuning system.

A perforated dielectric plate of Rogers RO4350B (ϵ_r=3.66, tanδ=0.004, h_p=1.524 mm) was designed with 500-μm diameter holes. Using Fig. 2.11 as a reference, the necessary frequency shift between the individual unit cells can be estimated for a starting point. Some additional tuning was necessary to account for additional parasitics due to the connection of the unit cells. After tuning the response of the plate, with an additional consideration that it be mechanically stable, the final structure is shown in Fig. 4.10(a). The simulation model shown in Fig. 4.10(b) indicates both the height of the plate (h_p) as well as the direction in which the plate was varied.

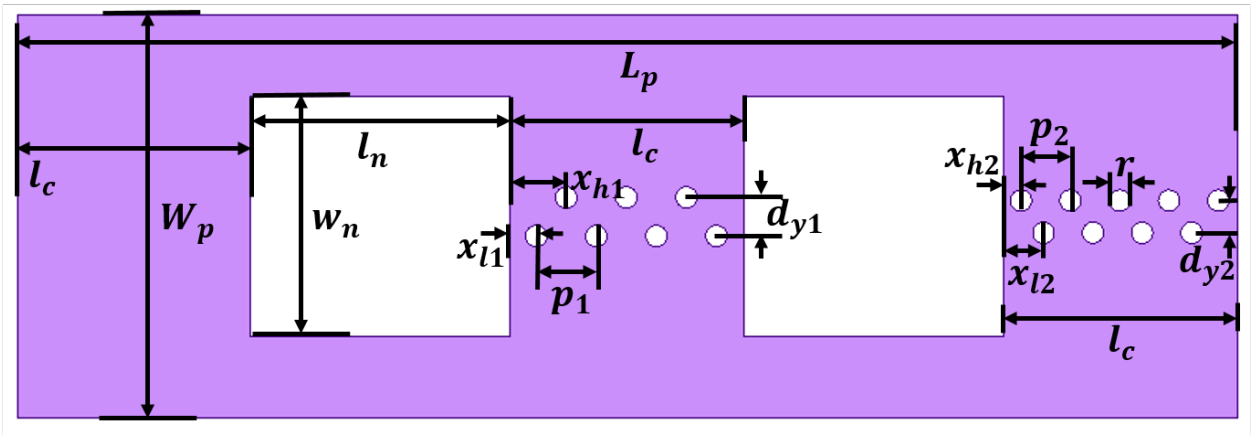

(a)

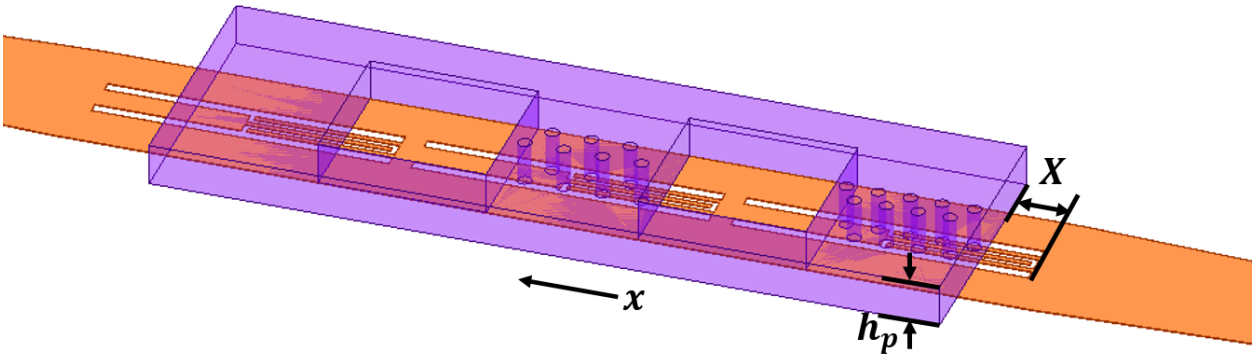

(b)

Figure 4.10: a) Dimensions of the dielectric plate: W_p=9.4 mm, L_p=28.45 mm, w_n=5.6 mm, l_n=6.05 mm, l_c=5.45 mm, x_{l1}=0.6 mm, x_{h1}=1.3 mm, p_1=1.4 mm, d_{y1}=0.9 mm, x_{l2}=0.925 mm, x_{h2}=0.4 mm, p_2=1.15 mm, d_{y2}=0.525 mm, r=500 μm. b) 3D layout showing the perforated dielectric plate of thickness h_p=1.524 mm, X=2.18 mm, and x indicating the direction of tuning. Exact dimensions for the filter and unit cell are shown in Fig. 4.10.

4.3.2 Simulation Results

Simulated scattering parameters of Fig. 4.10(b) for various values of X are provided in Fig. 4.11. When comparing the various curves shown in Fig. 4.11, it is apparent that the peak return loss is largely independent of the center frequency and remains relatively constant over the full tuning range. It should also be observed that as the center frequency decreases, the peak insertion loss in the rejection band also increases, but remains below 15 dB over the full range. The pass-band phase response was examined, but it was found

to be minimally dispersive away from the bandgap. This is to be expected based on the dispersion shown in Fig. 4.2(a), and the effect of changing the capacitance C as shown in Fig. 2.10.

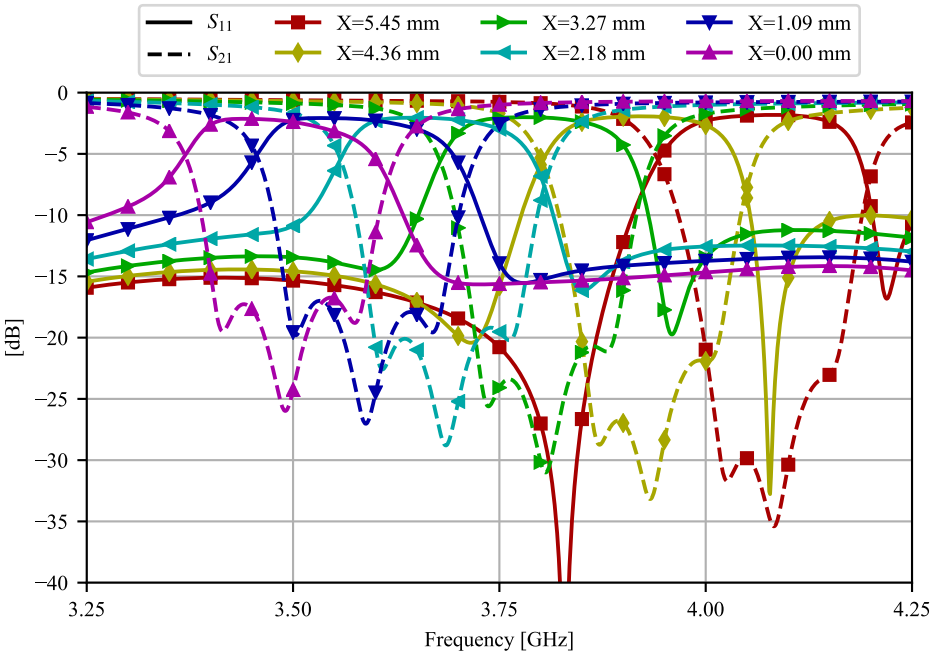

Figure 4.11: Full simulated scattering parameter results of the full tuning range.

Figure 4.12 shows the calculated 10-dB ABWs of each of the S_{21} curves in Fig. 4.12 and several additional points as a function of the center frequency, which is calculated as the arithmetic average of the 10-dB edge frequencies. In addition, calculated 10-dB ABWs are also provided for an unperforated dielectric plate. From this comparison, it is apparent that the compensated dielectric plate has a significant effect in reducing the variation in the ABW over the tuning range. Using (4.1), the tuning range ($\%T_r$) was calculated to be 15.3%, while the average ABW over the full tuning range (BW_m) was found to be 220 MHz using (4.2) with a percent variation ($\%\Delta$) of 2.14% using (4.3):

$$\%T_r = 100\% \left(2 \times \frac{f_{max} - f_{min}}{f_{max} + f_{min}} \right) \tag{4.1}$$

$$BW_m = \frac{BW_{max} + BW_{min}}{2} \tag{4.2}$$

$$\%\Delta = 100\% \left(\frac{BW_{max} - BW_m}{BW_m} \right) \tag{4.3}$$

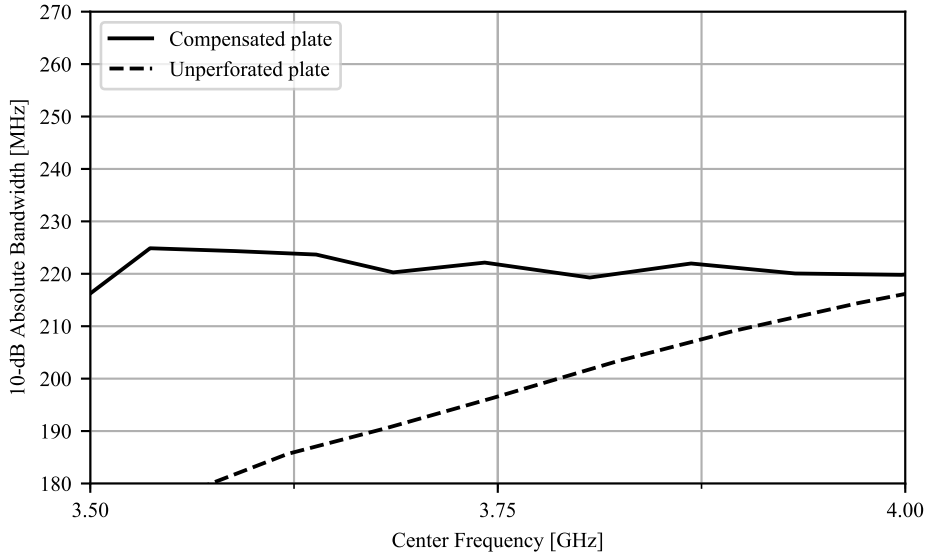

Figure 4.12: Simulated 10-dB rejection bandwidth versus center frequency based on Fig. 4.11.

There is some additional variation for lower center frequencies, but this is largely attributed to the periodicity of the holes in the dielectric plate. Using smaller holes with a tighter spacing is expected to reduce any apparent ripples in the ABW vs center frequency curves. This tuning range can be increased by using a higher permittivity dielectric for the tunable plate; for example, as shown in Fig. 4.7(a) with ϵ_r=6 the tuning range can be increased to 26.4%.

4.3.3 Tuning Super Structure Design

While the initial simulations were performed assuming the dielectric plate was precisely positioned without the use of a support structure, this was deemed to be impractical for multiple experimental measurements. This, by necessity, required the design of a tuning "super-structure" to both precisely control the location of the plate as well as eliminate the presence of any airgaps between the dielectric plate and the underlying MTM-EBG unit cells. For reasons of simplicity and access, a 3D structure was designed to act as a scaffold for the dielectric plate and 3D printed in ABS (acrylonitrile butadiene styrene). This structure was also designed to more precisely measure the physical position of the dielectric plate.

Based on these considerations, and the realizable dimensions using a Dremel 3D45, a simple sliding rail was used as the primary mount of the tuning structure, which was then affixed to the MTM-EBG using a variable height plate controlled by a screw. This was necessary as the limited nozzle output (approximately 50-μm) introduced a challenge in eliminating the presence of an airgap. Overcompensating (i.e. making the structure smaller than necessary) for the copper thickness would increase the pressure the dielectric plate applied to the MTM-EBG filter, while undercompensating would introduce an airgap. This variable height part (#4) reduced the necessary precision of the printed components.

After incorporating these changes, the final tuning structure model is provided in Fig. 4.13(a) and is composed of four, individually printed components: #1) Bottom support to restrict potentially bowing of the dielectric due to excessive pressure from the plate, thereby minimizing potential airgaps; #2) Upper support that incorporates a rail notch to freely vary the position of part #3; #3) Primary rail system that can be measured for the displacement and includes holes to facilitate the vertical movement of part #4. The hexagonal gap is designed for a 8-32 nylon screw; #4) Housing for the dielectric plate that allows for visual

confirmation its position. Parts #1, #2 and #3 were printed with a 50% infill, while part #4 was printed at 100% infill due to potential component breakage.

This tuning structure was not expected to have a pronounced effect on the performance of the tunable filter, but a verification was necessary. Due to the computational power required and uncertainty in the exact isotropy of the 3D printed ADS, only the case *without* the dielectric plate was examined. Incorporating this structure into the simulation model with known properties of ABS ($\epsilon_r \approx 3.2$ and $\tan\delta \approx 0.09$) [100], and assuming the lower infill could be modelled as a homogenous media, resulted in the blue curves in Fig. 4.14. This demonstrates that outside a minor downshift in operating frequency, which can be reduced by using a lower infill for the individual parts, the performance is largely unaffected by the presence of the tuning structure.

4.3.4 Experimental Results

The dielectic plate shown in Fig. 4.10(a) was fabricated using an LPKF Protomat S62, and the resulting structure is shown in Fig. 4.15(a). The full results of this structure, at the same displacement values as in simulation, are provided in Fig. 4.16. Similar to what was done for the simulation results, the 10-dB ABW was calculated for each of the S_{21} curves shown in Fig. 4.16 and plotted against their respective center frequencies, as shown in Fig. 4.17; this includes experimental measurements for an unperforated plate as a reference. As is clear in this comparison, the proposed compensation mechanism has had a pronounced effect in reducing the variation in ABW as the MTM-EBG-based bandstop is tuned. An increase in the ABW can be observed in both the compensated and unperforated plate of approximately the same amount which was reported in Section 4.2, suggesting that the source of this increase is again related to additional loss and asymmetries between the individual unit cells. The average experimental ABW was calculated to be 244 MHz, with a variation

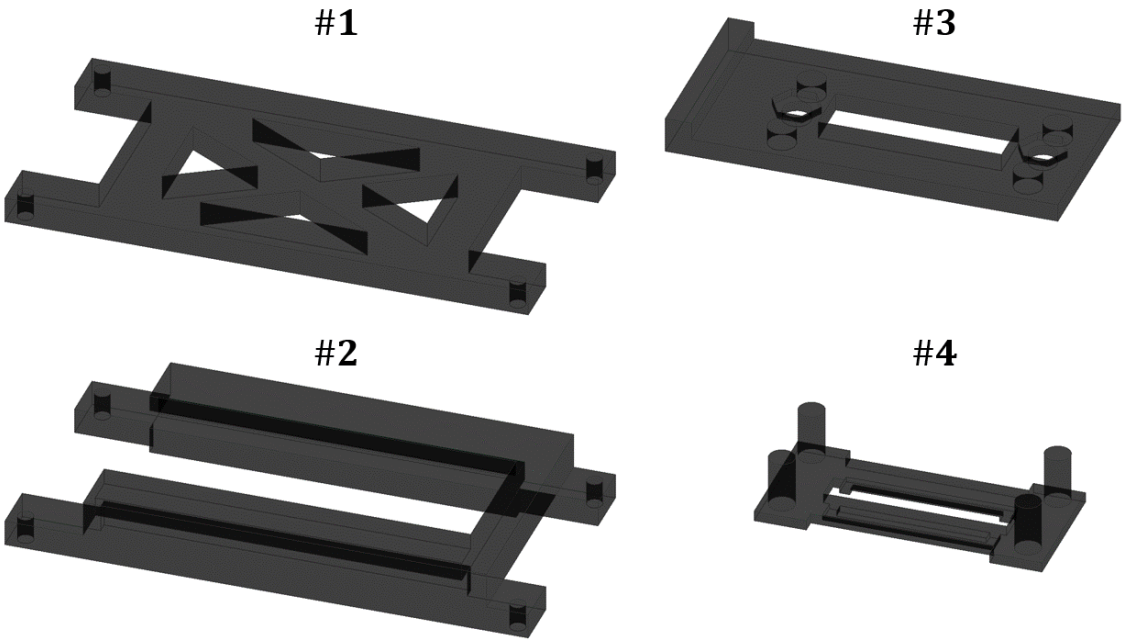

(a)

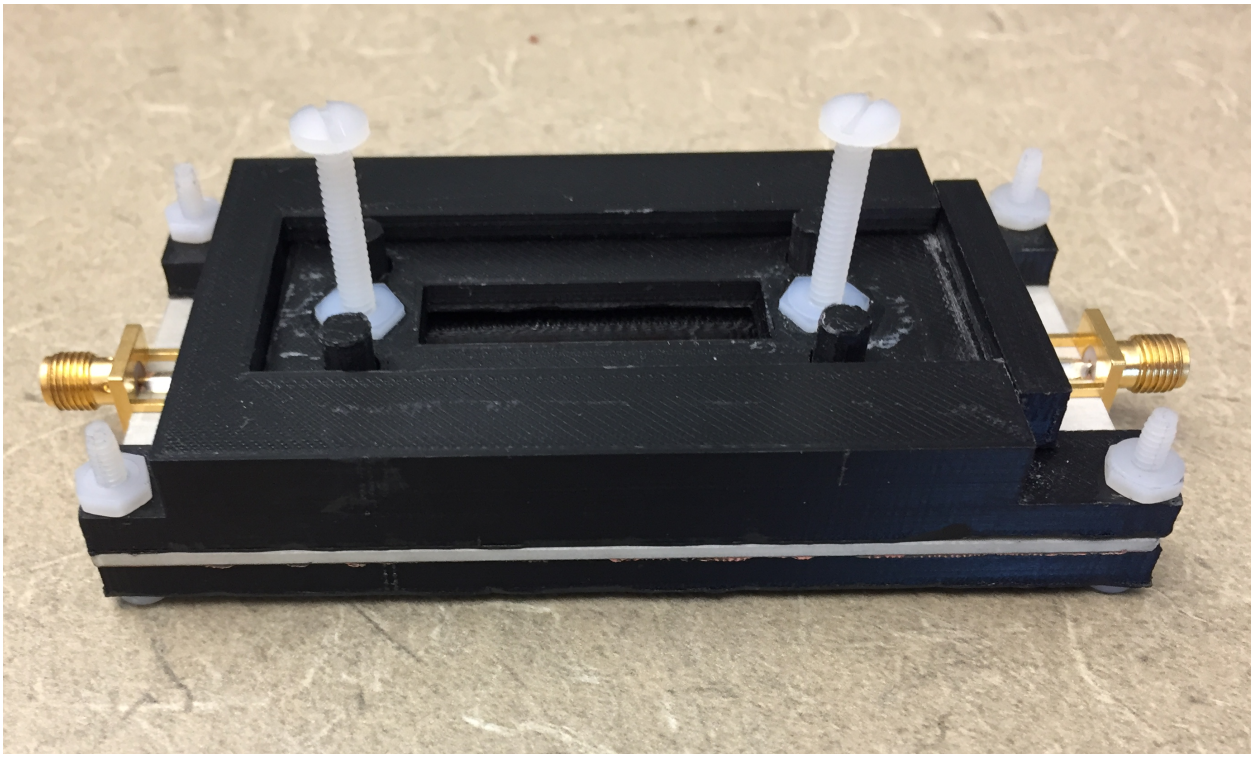

(b)

Figure 4.13: Tuning superstructure a) individual components and b) fabricated structure.

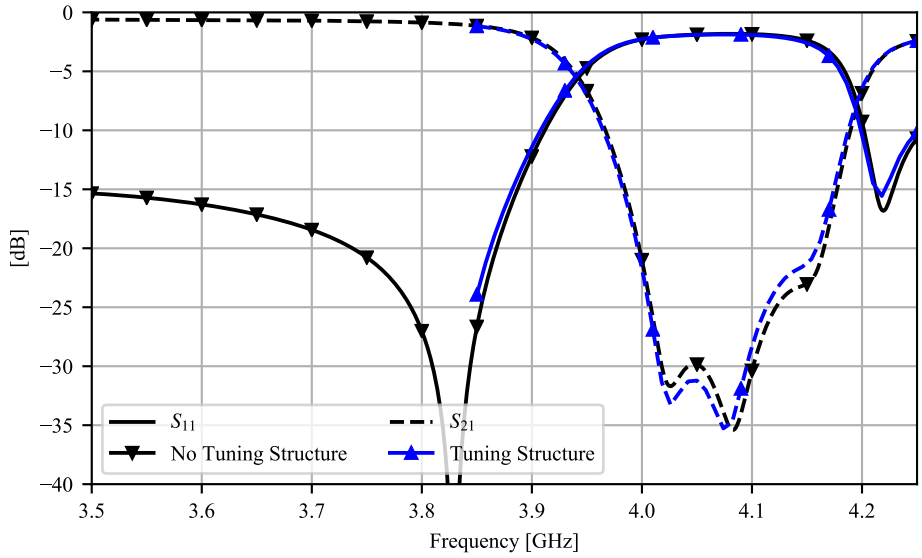

Figure 4.14: Comparison of the simulated MTM-EBG-based filter with and without the proposed tuning structure.

of 1.31%. This apparent decrease in variation is attributed to two factors; first, the increase in average ABW and second, a small reduction in the tuning range.

Comparing the experimental results in Fig. 4.16 to the simulated data provided in Fig. 4.11, it is apparent that the tuning range has been moderately reduced. In simulation for the minimum displacement of X=0 mm, the response was shifted to a center frequency of 3.49 GHz; in the experimental results, the same displacement resulted in a center frequency of 3.56 GHz. The experimental tuning range was therefore reduced from 15.3% to 12.3%. This may be attributed to anisotropy in the dielectric plate, which changes the effective permittivity seen by the interdigitated capacitors. In Fig. 4.12, most of the variation in the ABW occurs when the filter is tuned to the lowest center frequency. Since we have not completely tuned down to this level in the experimental results, this variation is effectively ignored and, as a result, contributes to a smaller experimental variation in ABW.

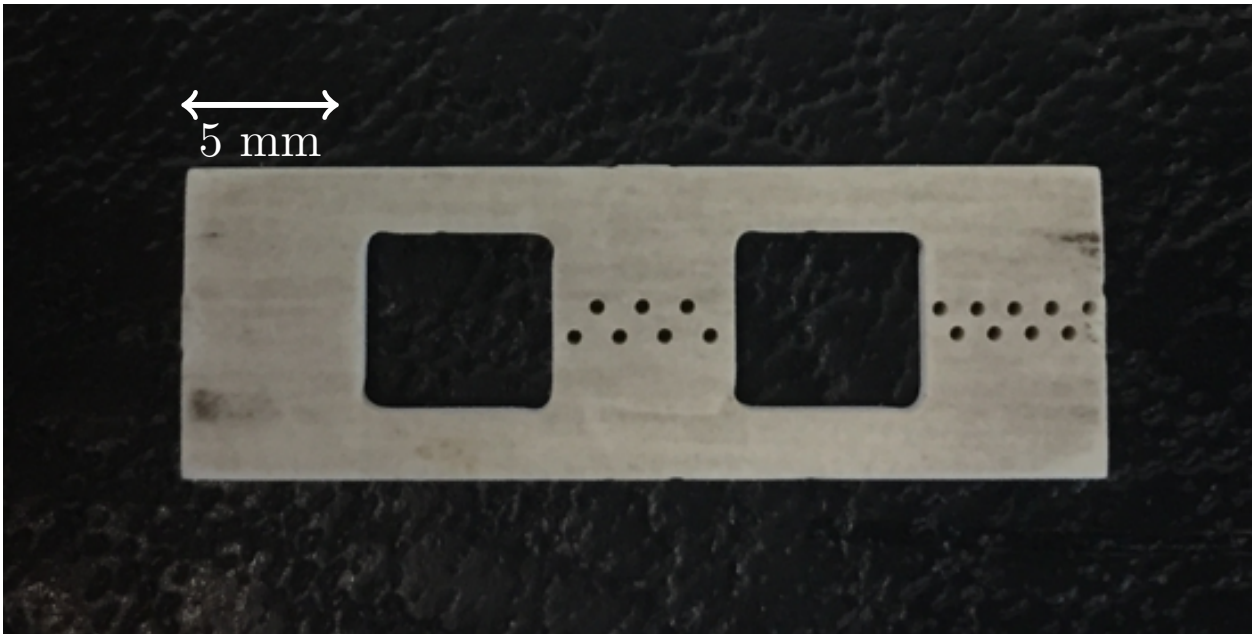

(a)

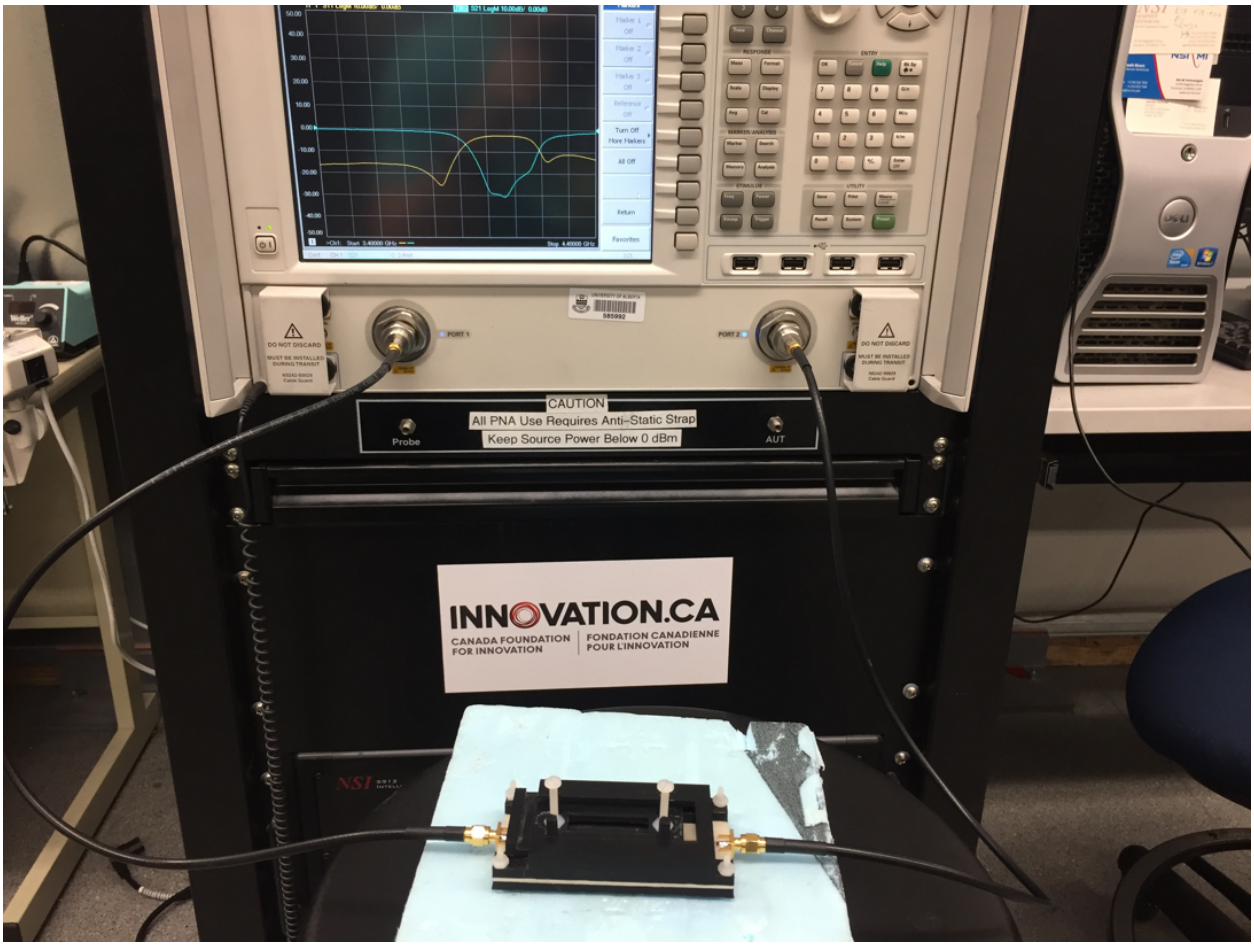

(b)

Figure 4.15: a) Fabricated dielectric plate and b) experimental measurement set-up.

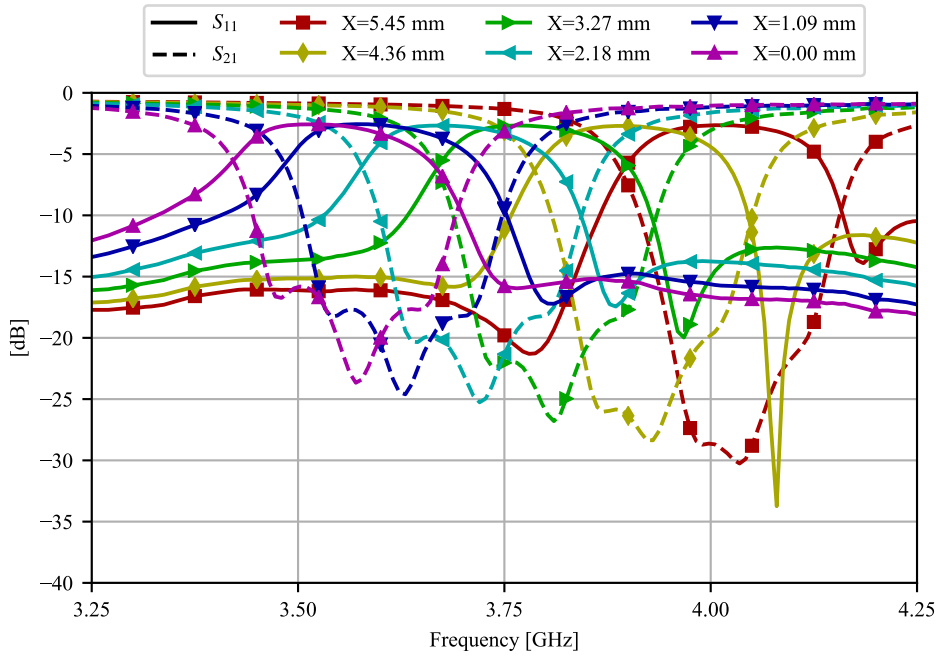

Figure 4.16: Full experimental scattering parameter results over the full tuning range.

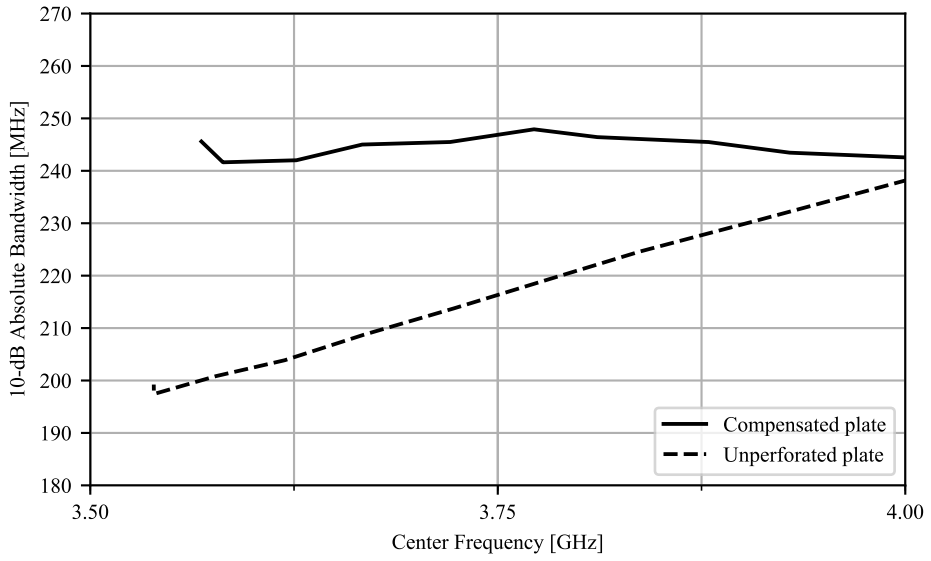

Figure 4.17: Experimental 10-dB rejection bandwidth versus center frequency based on Fig. 4.16.

PIM Measurements

Intermodulation of frequency components is not exclusively introduced by active, non-linear devices; it can also be introduced depending on the quality of the fabrication. Otherwise known as passive intermodulation (PIM), this is just as degrading on the performance of telecommunication systems as normal intermodulation. A large component of PIM can be found in interfaces, particularly in metal-to-metal connections. One claim in the use of mechanical tunability is that by using it, we introduce less intermodulation than active tuning schemes. Furthermore, we have assumed that the MTM-EBG-based filter has comparable PIM to conventional planar topologies. There is no way to simulate sources of PIM.

Thanks to our industrial partners, we were able to measure the PIM of this device using a Summitek Instruments iQA1921A. Generally, the PIM of a device is independent of the actual performance of the device, so the range the iQA operates over (1800-1945 MHz) was not a determining factor in the actual PIM results. The iQA, by default, inputs 43 dBm (20 W) of power at frequencies of 1945 and 1990 MHz and measures the resulting intermodulation. The MTM-EBG-based filter was first measured without the tuning structure or dielectric plate attached and found a PIM value of -131.46 dBc. The tuning structure and dielectric plate were then added and two cases were measured. First, when the dielectric plate fully covered the interdigitated capacitor, and second, when the interdigitated capacitor was uncovered. Respectively, these cases had PIM values of -129.16 and -132.82 dBc. As a baseline comparison to establish this performance against a conventional purely MS-based device, a simple bandstop filter was measured to have a PIM value of -137.60 dBc.

It is apparent that the MTM-EBG does not contribute a significant increase of PIM compared to a conventional MS-based device. Furthermore, the proposed tuning mechanism does not appear to contribute. While these are reasonable levels, telecommunication applications are

trending towards even lower PIM requirements; the specification from our industrial partner was -160 dBc. To reduce the PIM further would require a drastic change in design, and would necessitate a shift toward a different connection (such as a through SMA) or potentially a different fabrication process.

4.4 TV Whitespace Tunable Filter

The previous tunable filter was designed to have a fixed-frequency response just slightly outside the desired tuning range. In the case of the TV Whitespace filter, the actual design frequency was selected to be above the desired tuning range by an appreciable margin. In order to realize the desired tuning range of 39.31%, a dielectric permittivity of $\epsilon_p \approx$7-9 would have been required. These are not values readily available from manufacturers, so a larger permittivity is necessary to cover this range. To reduce the footprint of this filter, it was designed such that the lower portion of the tuning range meets the TV Whitespace spectrum specification.

4.4.1 Fixed-Frequency Filter Design and Results

The design of this filter followed a very similar procedure to that of the three-cell filter designed in Section 4.2 and therefore suffered from similar challenges; specifically, the restriction on the minimum bandwidth due to the tuning range and the position of the capacitors. The number of unit cells helps dictate the minimum insertion loss while the filter is fully de-tuned and increases the ABW. Due to the desired increase in tuning range, it was found that four unit cells were required in order to ensure that the stop-band had at least 10 dB of rejection; however, in early variations, this increased the ABW to approximately 47 MHz. In order to reduce this without increasing the total width of the MTM-EBG, and therefore sacrificing

some passband performance, several alterations were made to reach the desired ABW based on the parametrics in Table 2.2(b).

First, the dielectric substrate was changed from Rogers RO4350B (ϵ_r=3.66 and tanδ=0.004) to Rogers RO3003 (ϵ_r=3.0 and tanδ=0.001). The justification for this change can be seen clearly in Table 2.2(b), which demonstrates that as the substrate permittivity is reduced (and all other parameters are held constant), the center frequency increases and bandwidth slightly decreases. Second, increasing the capacitance has a strong effect on decreasing the bandgap of an infinite cascade of unit cells. Since a single unit cell is representative of this infinite cascade, the same modification can be done to reduce the ABW. By displacing the capacitor from the center of the unit cell, which does not have a significant effect of the overall performance, the capacitor finger length (and therefore capacitance) can be increased while maintaining a similar unit cell size offering additional miniaturization. To incorporate this shift, however, the distance between the capacitive regions was not equal to the total length of the capacitive fingers; the tuning set-up shown in Fig. 4.10 could not be employed here. Instead the four unit cells were arranged in a "square" configuration, as shown in Fig. 4.18, which eliminates any potential overlap between the unit cells.

Since additional unit cells were necessary to realize the tunability of this filter, it suffered from the same mismatch that was discussed in Section 2.3.2, in that there was very poor performance near the edges of the bandgap. To compensate for this mismatch, the filter was made slightly asymmetric by increasing the CPW stripline width (s) of the inner unit cells; these are indicated in Fig. 4.19. After tuning, the final layouts of the individual unit cells are shown in Figs. 4.19(a) and 4.19(b); identical dimensions have not been repeated.

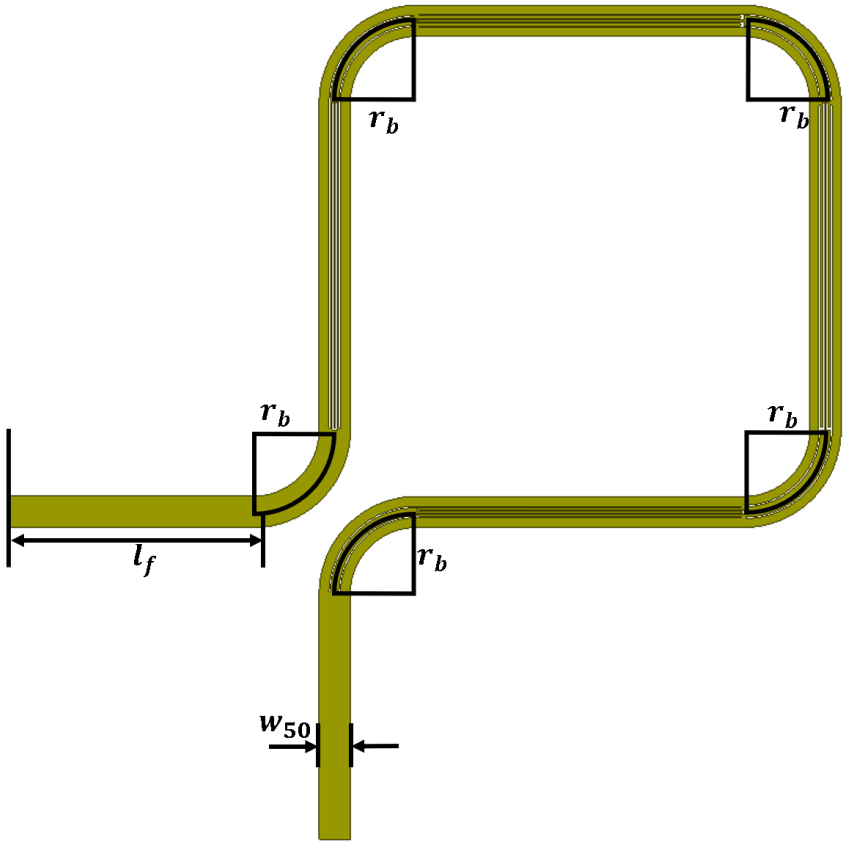

Figure 4.18: Full simulation model of the MTM-EBG-based TV Whitespace Filter: l_f=30 mm, r=6 mm and w_{50}=3.8 mm.

Simulation and Experimental Results

The full structure shown in Fig. 4.18 was then simulated in HFSS and these results are shown in Fig. 4.20. The 10-dB ABW was calculated as 37.4 MHz with a center frequency of 804.2 MHz and passband performance better than 10 dB over the full passband. Above 822 MHz the passband performance is degraded, but this is outside the specifications for TV Whitespace applications.

This structure was then fabricated on Rogers RO3003 in-house using the LPKF Protolaser U3; the fabricated board is shown in Fig. 4.21 and the measured data is again shown in Fig. 4.20. Generally, these results are in excellent agreement. The 10-dB ABW for

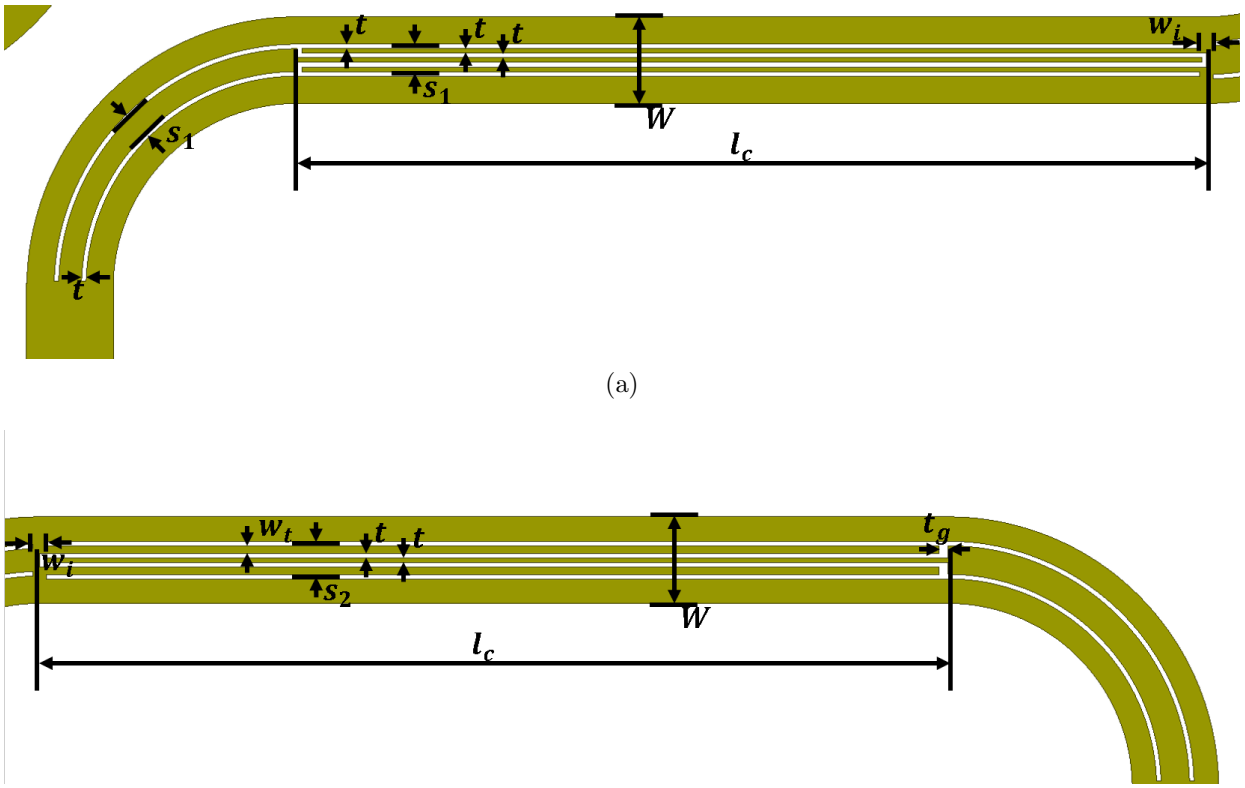

Figure 4.19: Layout of the individual MTM-EBG unit cells: a) Outer unit cell: W=3.8 mm, s_1=1.0 mm, l_c=40.0 mm, w_i=0.6 mm, and t=0.2 mm. b) Inner cell: s_2=1.5 mm, w_t=0.325 mm and t_g=0.4 mm.

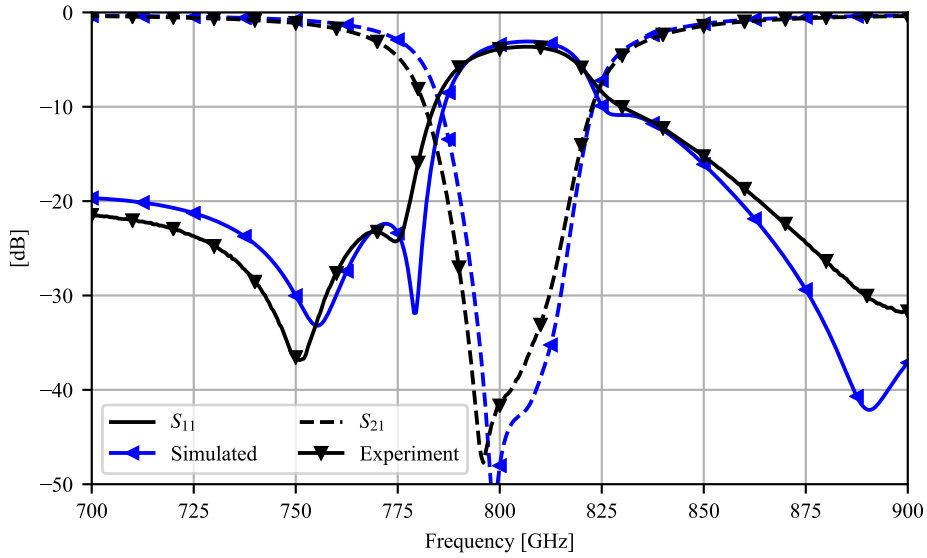

Figure 4.20: Simulated and experimental results for the TV Whitespace MTM-EBG-based bandstop filter.

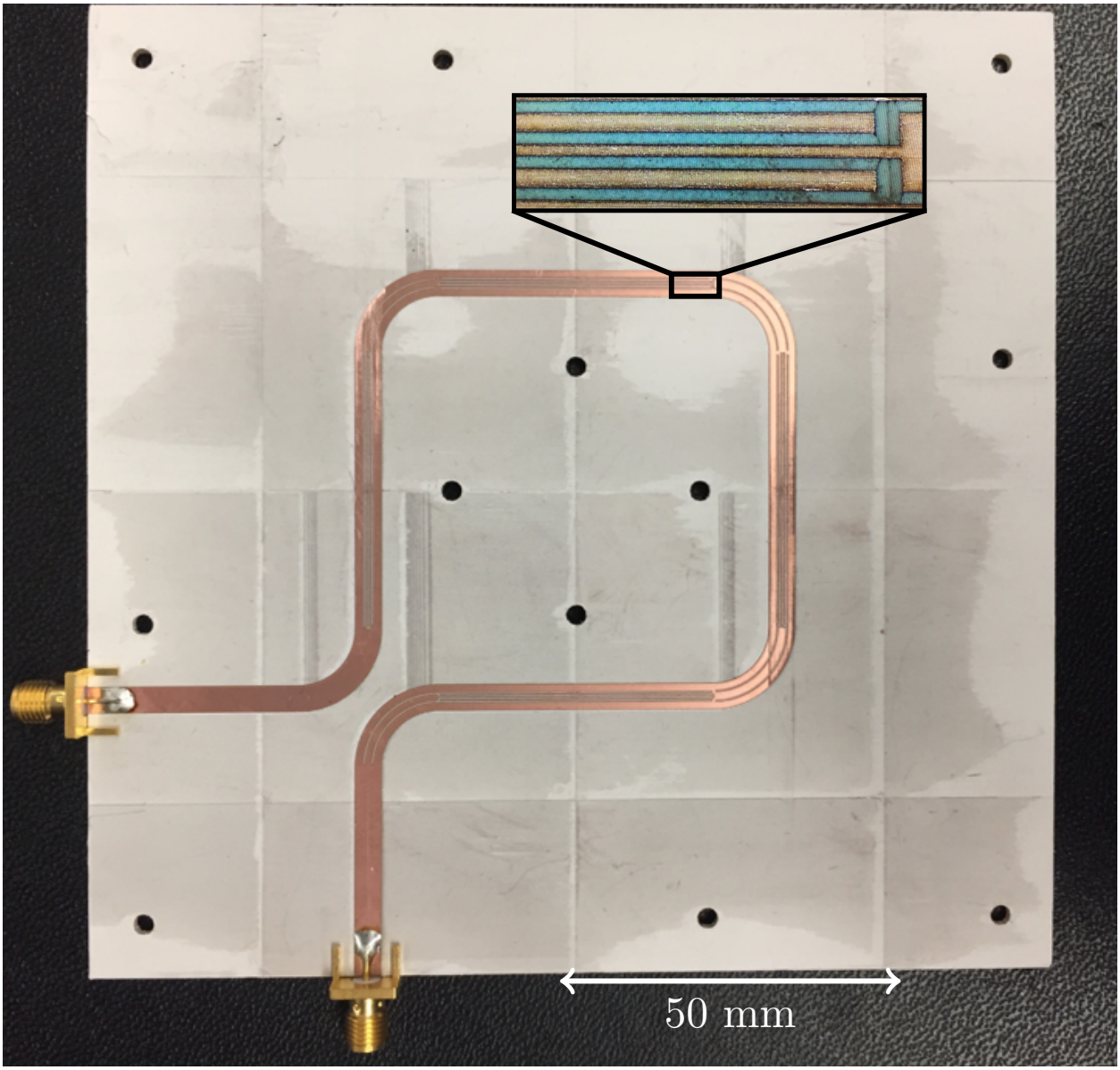

Figure 4.21: Fabricated fixed-frequency TV Whitespace filter. The inset shows the base of one of the interdigitated capacitors.

the experimental results was calculated as 40 MHz with a center frequency of 802.7 MHz. This slight increase in the 10-dB ABW is largely attributed to small asymmetries between the individual unit cells that were introduced during the fabrications. These asymmetries also slightly affected the passband performance of the filter. While it is clear that some discoloration was introduced during the fabrication, previous fabrications indicate that this

has no effect on the overall performance of the filter.

4.4.2 Tunable Filter Design and Results

Dielectric Plate Design

The dielectric plate used to realize the tuning range of the TV Whitespace filter was designed using the same procedure discussed in Section 4.3.1. However, due to the higher permittivity used here in order to realize the necessary tuning range (ϵ_p=10.2) and the increased number of unit cells, the individual holes were not staggered and only the periodicity of each plate was changed; this greatly simplified the design procedure. The design of this plate started with shifting the response of each individual unit cell to the desired position by changing the period of the airholes, then tuning the response of the full filter to the desired ABW. After this tuning, the final dimensions for the plate are provided in Fig. 4.22.

Simulation Results

Simulations were performed on the TV Whitespace filter for varying degrees of displacement X. Similar to what was done in Section 4.3, Fig. 4.23 plots the scattering parameter response for a reduced set of displacements and Fig. 4.24 plots the corresponding 10-dB transmission ABW against the respective center frequency. As expected due to the tuning range and shown in Fig. 4.23, there is a substantial variation in the stop-band rejection level as the filter is tuned. Additional unit cells could be added to mitigate this effect, but would require different asymmetries, layout and plate designs. Even though the peak rejection level within the stop band decreases, the passband return loss remains relatively constant as the stop-band is tuned, and never increases above -16 dB.

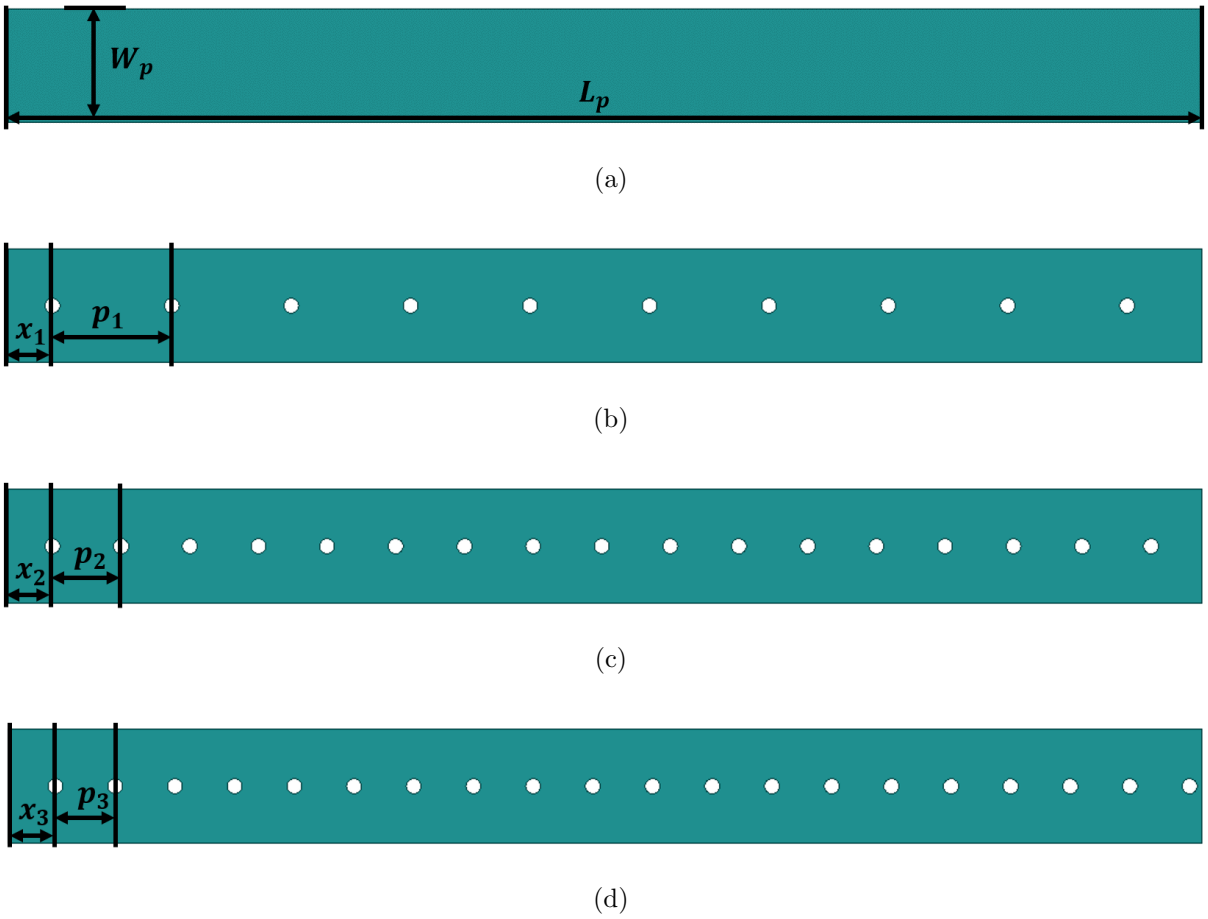

Figure 4.22: Dimensions of the four tunable plates used in the TV Whitespace tunable filter: a) L_p=40 mm, W_p=3.8 mm. b) x_1=1.5 mm, p_1=4 mm. c) x_2=1.5 mm, p_2=2.3 mm. d) x_3=1.6 mm, p_3=2.0 mm.

Compared to an unperforated plate, the bandwidth varies substantially less as shown in Fig. 4.24. The unperforated plate has a tuning range of 54.6% with a variation of 33.0% while the compensated plate has a tuning range of 52.3% with a variation of 13.9%. The average ABW (BW_m) for the compensated design was calculated as 32.7 MHz. It is clear that both the unperforated and compensated designs share a nearly identical rate of change for large values of X and correspondingly high center frequencies. This is attributed to the relatively small period of the air holes. While increasing this periodicity should result in a more constant ABW over the full range, it is possible that in doing so it would sacrifice the performance when the capacitors were fully covered. Alternatively, the air holes could be

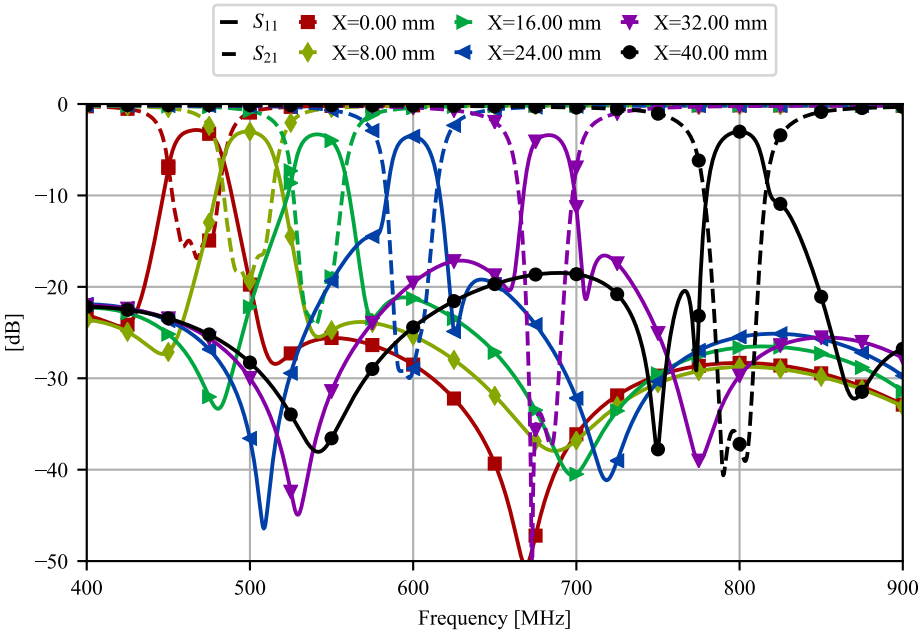

Figure 4.23: Simulated scattering parameters of the tunable TV Whitespace filter over the full displacement range.

staggered in the same manner as the tunable filter presented in Section 4.3. This design offers better variation over the TV Whitespace frequency range, which only covers 470-700 MHz. Over this range, the unperforated plate has a variation of approximately 25.4% while the compensated design only varies by approximately 8.9%. This in turn reduces the BW_m for the compensated design to 30.7 MHz.

Experimental and Fabrication Challenges

The design of the tuning superstructure was far more challenging than the previous design in Section 4.3.4 due to the requirement that each plate had to be independently varied. A single tuning structure was printed, however the cumulative defects due to the feature size are believed to have contributed to poor measurements and a high degree of difficultly tuning. In addition to the tuning structure, the individual plates were challenging to use due

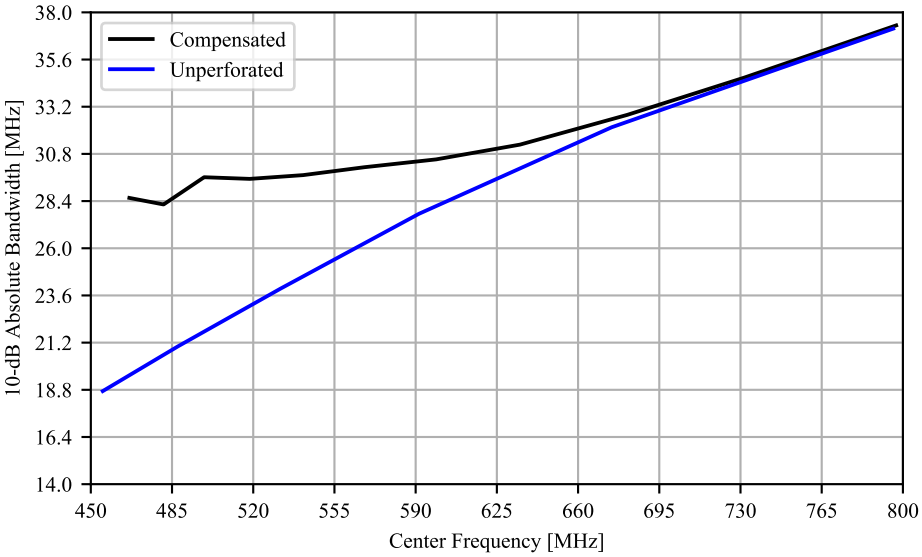

Figure 4.24: Simulated 10-dB rejection bandwidth versus center frequency based on Fig. 4.23.

to the softness of Rogers 3010. Due to these complications, successful measurements over the tuning range were not acquired. Future works concerning this device will be directed towards re-designing the tuning mechanism to be functional with the TV Whitespace tunable filter.

4.5 Comparison to Alternate Technology

Two separate MTM-EBG-based tunable filters were designed in this chapter. Each of these designs have excellent tunability performance that is comparable to waveguide (WG) and substrate-integrated WG (SIW) tunable filters, as demonstrated in Table 4.1. This table summarizes the tunability performance of both bandstop and bandpass filters on the basis of (4.1), (4.2), (4.3) and the maximum center frequency within the tuning range. The %Δ observed in Section 4.3.4 is comparable to complex WG structures and is lower than alternate planar systems by several percentage points. While the filter designed and tested in Section 4.4 had a larger variation in the ABW, it had a larger tuning range and a comparable BW_m

to alternate MS-based filters. Adding a single additional unit cell to this structure would likely improve the variation to the levels observed, but was outside the scope of this work.

Table 4.1: Comparison of the MTM-EBG tunable filters to alternate bandpass and bandstop filters in recent literature. BW in MHz and f_{max} in GHz

	BW_m	$\pm\%\Delta$	f_{max}	$\%T_r$	Technology	# Tuning Elements
§4.3	244*	1.31	4.03	12.3	MS	1
§4.4	*33**	*13.9*	*0.8*	*52.3*	*MS*	*4*
[79]	112*	4.89	1.88	35.0	MS	2
[80]	546*	7.80	5.41	38.7	MS	3
[81]	60^+	6.67	0.78	34.2	MS	4
[82]	60^+	4.17	0.85	31.3	MS	6
[84]	300*	5.00	16.2	9.5	WG	1
[85]	181*	1.66	19.7	1.7	WG	4
[86]	46*	1.63	6.00	64.9	SIW	4
[87]	290^+	3.48	1.5	50	MS	3

* 10-dB BW, + 3-dB BW, WG=Waveguide
Simulation, Experiment

As demonstrated in this work, the MTM-EBG is easily integrated into an existing MS TL and occupies little to no additional space; the tuning structure used here is, of course, 3D, but is necessary for the mechanical tuning and could be miniaturized if desired without much difficulty. Conversely, the designs presented in [79, 81] and [82] have a large footprint to accommodate the resonating elements, and require these large dimensions to ensure the coupling coefficient displays the proper behavior with frequency. Furthermore, the dependence on varactor elements in those designs limits the maximum frequency of operation and can introduce non-linearities contributing to effects such as PIM. While WG-based filters generally had a comparable $\%\Delta$ to the proposed filter, they either had significantly less tuning range [85] or employed secondary non-synchronous tuning to reduce the $\%\Delta$ to the reported levels and required a multi-layer design [86].

One additional benefit offered by the proposed MTM-EBG-based tunable filter is the ability to change the tuning range without requiring a total re-fabrication of the structure. In

[79–82, 84–86] the tuning range is tied to a hardwired component, such as a varactor or a piezo-electric actuator. As was previously demonstrated, the tuning range for the proposed MTM-EBG is almost entirely related to the permittivity of the dielectric plate.

Chapter 5

Conclusion

5.1 Summary

An overview behind the operation of the MTM-EBG is provided in Chapter 2, and properties of the fully embedded MTM-EBG are examined. Two distinct applications are discussed; the ability to realize a dual-band response through engineering a particular phase response, and a strong predictable rejection band for bandstop filtering. It is demonstrated that a single MTM-EBG has a phase response that is accurate to the dispersion predicted by the Bloch analysis, with a predictable Bloch impedance from scattering parameter data. The aspect of tunability was then discussed, and it was shown that the bandgap of the equivalent circuit model depends heavily on the capacitance. By asymmetrically varying the capacitance of neighbouring unit cells, the bandwidth of a finite cascade of MTM-EBG unit cells can be increased representing a mechanism by which a constant ABW may be maintained. A mirrored asymmetry was than investigated and found to have a pronounced effect on the passband performance of the cascaded MTM-EBGs. This was investigated for a four cell cascade, but should be applicable to any number of unit cells.

In Chapter 3, the MTM-EBG is ultimately used to realize a dual-band corporate feed network. As an initial step, the MTM-EBG is used to develop a dual-band back-to-back

impedance transformer for converting 50 Ω to 100 Ω. Experimental results verified the initial properties, and the 70.7 Ω MTM-EBG was re-designed for 35.4 Ω. Compared to alternate dual-band embedded components in past literature, the MTM-EBG is noticeably more compact and offers flexibility in not only the phase it produces, but also the position of the rejection band. The dual-band T-junction was then used to realize a dual-band T-junction power divider and expanded into the dual-band corporate feed network. An initial design of this corporate feed network revealed a sensitivity of the MTM-EBG to asymmetric current distributions. It was identified to be caused by the excitation of the CSL mode of the MTM-EBG. Due to the mechanism of operation behind the MTM-EBG it was not possible to suppress this mode without seriously degrading the performance of the MTM-EBG. Topological changes were made to mitigate the effects of the CSL mode and resulted in an improved dual-band feed network, which was ultimately better suited for use in antenna systems.

Chapter 4 presents two different applications of a tunable MTM-EBG-based bandstop filter with constant ABW. The first was designed to operate with constant ABW from 3.5 to 4.1 GHz such that it may be used in telecommunication systems. An initial design of the fixed-frequency filter is provided and fabricated. Instead of using a varactor, the tunability is realized by placing a piece of dielectric directly on the surface of the MTM-EBG. By varying the position of this dielectric along the MTM-EBG, the effective capacitance can be varied with relative ease. Furthermore, due to the layout of the fixed-frequency filter the tuning mechanism can be realized with a single element while maintaining a constant ABW. Experimental results for this tunable filter verify this performance with only a slight reduction in tuning range and an increase in the ABW. The tunable MTM-EBG was then re-designed for an application targeting TV Whitespace filtering. To reach the necessary range, additional unit cells were cascaded which ultimately degraded the passband performance. This was compensated for by introducing a slight mirrored asymmetry and changes to the layout of

the individual unit cells; these changes required a more complicated tuning mechanism.

5.2 Future Research

Future research directions within the scope of this work include, but are not limited to:

1. Fully integrated dual-band antenna array: It was demonstrated in this work that the MTM-EBG could be used to realize a dual-band corporate feed network. Future implementations of this structure would focus on the integration of dual-band antenna elements, such as the patch antennas demonstrated in [4], into the dual-band corporate feed network to realize a complete dual-band antenna array.

2. Multi-band networks incorporating embedded MTM-EBG unit cells: Initial research suggests this may be accomplished by using multiple cascaded MTM-EBG, each of which have been designed such that the net phase through the cells is the desired phase at each of the operating points. Additional research into how this phase can be accurately modelled using a finite number of unit cells, as well as further research on how propagation near the bandgap can be improved.

3. Extension of the MTM-EBG to the MM-wave regime: Due to the availability of fully printed features for the MTM-EBG, this structure should be comparatively easy to extend to MM-wave applications demanding planar structures. However, realizing the necessary capacitance to operate at these frequencies will be the primary challenge as current fabrication techniques used in this group are limited to features on the order of 100 μm and MM-wabe operation will inevitable require finer features. In addition, loss will be a much more serious issue at these frequencies so finer control over fabrication tolerances and dielectric substrates will be necessary. Lithography is a viable option to meet these specifications, but has yet to be applied in practice.

4. Expanded application of the MTM-EBG as a bandgap filter: A better characterization of the MTM-EBG as a filter element would permit it to be applied to realize different filtering layouts and applications. Furthermore, this would reduce the limits imposed by geometric constraints. In order to accomplish this, a better understanding of the discrete resonances of the MTM-EBG and, ideally, the development of a closed form expression for the response of a single MTM-EBG unit cell. Some research has been taken in regards to this goal, but is limited by a lack of understanding of how to decouple the MTM-EBG from the input transmission line and characterizing the response of the MTM-EBG on the basis of interresonator coupling.

5. Synchronously tuned constant ABW tunable MTM-EBG: The current tunable filter has a limitation in that it requires additional unit cells to preserve the stop-band rejection levels. Future research would examine the modifications required to ensure a constant ABW where additional engineering of the tunable dielectric plate is not required. Based on recent publications concerning constant ABW filters, this may be accomplished by engineering the coupling coefficient between the input and output lines to be frequency independent. This endeavor is limited to the current understanding of how neighbouring MTM-EBG unit cells may couple, which is well understood on the basis of modal coupling but offers little insight into how the coupling coefficient of this cell may be modified.

Summary of Contributions

Journal Papers (Under Review)

1. **Jacob A. Brown**, Stuart Barth, Braden P. Smyth and Ashwin K. Iyer, "Compact Mechanically Tunable Microstrip Bandstop Filter with Constant Absolute Bandwidth

Using an Embedded Metamaterial-Based EBG," Under review in *IEEE Trans. Microw. Theory Techn.*, 2019.

Journal Papers (Accepted or Published)

1. Stuart Barth, Braden P. Smyth, **Jacob A. Brown** and Ashwin K. Iyer, "Theory and Design of Dual-Band Microstrip Networks Using Embedded Metamaterial-Based Electromagnetic Bandgap Structures (MTM-EBGs)," In press for the Special Issue on Recent Advancements in Metamaterials and Metasurfaces, *IEEE Trans. Antennas Propag.*, 2019.

2. **Jacob A. Brown**, Stuart Barth, Braden P. Smyth and Ashwin K. Iyer, "Dual-Band Microstrip Corporate Feed Network Using an Embedded Metamaterial-Based EBG," *IEEE Trans. Antennas Propag.*, vol. 67, no. 11, pp. 7031–7039, 2019.

Conference Papers (Accepted or Published)

1. **Jacob A. Brown** and Ashwin K. Iyer, "Mechanically Tunable MTM-EBG-based Bandstop Filter", Accepted for presentation at *14th European Conf. Antennas and Propagation EuCAP 2020*, March 2020.

2. Stuart Barth, Braden P. Smyth, **Jacob A. Brown**, and A. K. Iyer, "Embedded MTM-EBGs for antenna applications," *USNC-URSI National Radio Science Meeting*, (Boulder, CO, USA), January 9-12, 2019.

3. **Jacob A. Brown** and Ashwin K. Iyer, "Design and Characterization of a Dual-Band Impedance Transformer Based on an Embedded MTM-EBG", *Proc. IEEE Int. Symp. Antennas and Propagation USNC/URSI National Radio Science Meeting*, July 2019.

4. Braden P. Smyth, Stuart Barth, **Jacob A. Brown** and Ashwin K. Iyer, "The MTM-EBG: A Fully Uniplanar, Printable, and Embedded Solution for Multi-Band Functionality in Microstrip Devices and Antennas," *Proc. 2019 URSI International Symposium on Electromagnetic Theory (EMTS)*, May 2019.

Patent Applications

1. Ashwin K. Iyer, Stuart Barth, Braden P. Smyth, and **Jacob A. Brown**, "Applications of metamaterial electromagnetic bandgap structures," International (PCT) Patent Application PCT/CA2019/050638, filed May 10, 2019.

Bibliography

[1] G. V. Eleftheriades, A. K. Iyer, and P. C. Kremer, "Planar negative refractive index media using periodically L-C loaded transmission lines," *IEEE Trans. Microw. Theory Techn.*, vol. 50, no. 12, pp. 2702–2712, Dec. 2002.

[2] S. Barth and A. K. Iyer, "A Miniaturized Uniplanar Metamaterial-Based EBG for Parallel-Plate Mode Suppression," *IEEE Trans. Microw. Theory Techn.*, vol. 64, no. 4, pp. 1176–1185, Apr. 2016.

[3] S. Barth, "Theory and Applications of a Uniplanar Transmission-Line Metamaterial-Inspired Electromagnetic Bandgap Structure," Master's thesis, University of Alberta, 2015.

[4] B. P. Smyth, S. Barth, and A. K. Iyer, "Dual-Band Microstrip Patch Antenna Using Integrated Uniplanar Metamaterial-Based EBGs," *IEEE Trans. Antennas Propag.*, vol. 64, no. 12, pp. 5046–5053, Dec. 2016.

[5] S. Barth and A. K. Iyer, "A low-profile dual-band circular patch antenna for GPS using metamaterial-based EBGs," in *Proc. IEEE Int. Symp. Antennas and Propagation USNC/URSI National Radio Science Meeting*, Jul. 2017, pp. 1727–1728.

[6] B. P. Smyth and A. K. Iyer, "Dual-band wilkinson power divider using uniplanar metamaterial-based EBGs," in *Proc. IEEE Int. Symp. Antennas and Propagation USNC/URSI National Radio Science Meeting*, Jul. 2017, p. 457.

[7] S. Barth and A. K. Iyer, "A Dual-Band Quadrature Hybrid Coupler Using Embedded MTM-EBGs," in *Proc. IEEE Int. Symp. Antennas and Propagation USNC/URSI National Radio Science Meeting*, Jul. 2018, pp. 199–200.

[8] S. Barth, B. P. Smyth, J. A. Brown, and A. K. Iyer, "Theory and Design of Dual-Band Microstrip Networks Using Embedded Metamaterial-Based Electromagnetic Bandgap Structures (MTM-EBGs)," in press for the Special Issue on Recent Advancements in Metamaterials and Metasurfaces, *IEEE Trans. Antennas Propag.*, 2020.

[9] B. P. Smyth and A. K. Iyer, "Compact Tri-Band Microstrip Stub Filter Using Embedded MTM-EBGs," in *Proc. IEEE Int. Symp. Antennas and Propagation USNC/URSI National Radio Science Meeting*, Jul. 2018, pp. 163–164.

[10] J. A. Brown, S. Barth, B. P. Smyth, and A. K. Iyer, "Dual-Band Microstrip Corporate Feed Network Using an Embedded Metamaterial-Based EBG," *IEEE Trans. Antennas Propag.*, vol. 67, no. 11, pp. 7031–7039, Nov. 2019.

[11] J. O. Scanlan, "Theory of microwave coupled-line networks," *Proceedings of the IEEE*, vol. 68, no. 2, pp. 209–231, Feb. 1980.

[12] C. R. Paul, *Analysis of Multiconductor Transmission Lines*. John Wiley & Sons, 2008, google-Books-ID: uO5HiV6V8bkC.

[13] J. A. Brandão Faria, "Nonuniqueness of modal transformations for multiconductor transmission line problems," *International Transactions on Electrical Energy Systems*, vol. 27, no. 8, p. e2342, 2017.

[14] S. Datta, C. T. Chan, K. M. Ho, and C. M. Soukoulis, "Effective dielectric constant of periodic composite structures," *Physical Review B*, vol. 48, no. 20, pp. 14 936–14 943, Nov. 1993. [Online]. Available: https://link.aps.org/doi/10.1103/PhysRevB.48.14936

[15] J. S. Colburn and Y. Rahmat-Samii, "Patch antennas on externally perforated high dielectric constant substrates," *IEEE Transactions on Antennas and Propagation*, vol. 47, no. 12, pp. 1785–1794, Dec. 1999.

[16] A. Alu and Nader Engheta, "Physical insight into the "growing" evanescent fields of double-negative metamaterial lenses using their circuit equivalence," *IEEE Transactions on Antennas and Propagation*, vol. 54, no. 1, pp. 268–272, Jan. 2006.

[17] F. Elek and G. V. Eleftheriades, "Dispersion analysis of the shielded Sievenpiper structure using multiconductor transmission-line theory," *IEEE Microw. Wireless Compon. Lett.*, vol. 14, no. 9, pp. 434–436, Sep. 2004.

[18] F. Elek, "Theory and Applications of multiconductor transmission line analysis for shielded sievenpiper and related structures," Ph.D. dissertation, University of Toronto, 2010.

[19] R. Islam, "Theory and applications of microstrip/Negative-Refractive-Index transmission line (MS/NRI-TL) coupled-line couplers," Ph.D. dissertation, University of Toronto, 2011.

[20] F. Yang, K. P. Ma, Y. Qian, and T. Itoh, "A uniplanar compact photonic-bandgap (UC-PBG) structure and its applications for microwave circuit," *IEEE Trans. Microw. Theory Techn.*, vol. 47, no. 8, pp. 1509–1514, Aug. 1999.

[21] C. Sabah, F. Urbani, and S. Uckun, "Frequency Dependence of Bloch Impedance in Left-Handed Transmission Line," in *Proc. Second European Conf. Antennas and Propagation EuCAP 2007*, Nov. 2007, pp. 1–5.

[22] T. Nakabayashi, A. Mishiro, H. Deguchi, and M. Tsuji, "Improvement of transmission characteristics of composite right/left handed microstrip lines by using impedance matching," in *2017 IEEE Asia Pacific Microwave Conference (APMC)*. IEEE, 2017, pp. 1076–1079.

[23] A. Grbic and G. V. Eleftheriades, "Periodic analysis of a 2-D negative refractive index transmission line structure," *IEEE Transactions on Antennas and Propagation*, vol. 51, no. 10, pp. 2604–2611, Oct. 2003.

[24] J. B. Pendry, A. J. Holden, D. J. Robbins, and W. J. Stewart, "Low frequency plasmons in thin-wire structures," *Journal of Physics: Condensed Matter*, vol. 10, no. 22, p. 4785, 1998.

[25] H. Mosallaei and K. Sarabandi, "Magneto-dielectrics in electromagnetics: concept and applications," *IEEE Transactions on Antennas and Propagation*, vol. 52, no. 6, pp. 1558–1567, Jun. 2004.

[26] J. B. Pendry, A. J. Holden, D. J. Robbins, and W. J. Stewart, "Magnetism from conductors and enhanced nonlinear phenomena," *IEEE Trans. Microw. Theory Techn.*, vol. 47, no. 11, pp. 2075–2084, Nov. 1999.

[27] V. G. Veselago, "Electrodynamics of substances with simultaneously negative electrical and magnetic permeabilities," *Physics-Uspekhi*, vol. 10, no. 4, pp. 504–509, 1968.

[28] J. B. Pendry, "Negative refraction makes a perfect lens," *Physical review letters*, vol. 85, no. 18, p. 3966, 2000.

[29] A. K. Iyer and G. V. Eleftheriades, "Free-Space Imaging Beyond the Diffraction Limit Using a Veselago-Pendry Transmission-Line Metamaterial Superlens," *IEEE Transactions on Antennas and Propagation*, vol. 57, no. 6, pp. 1720–1727, Jun. 2009.

[30] D. Schurig, J. J. Mock, B. J. Justice, S. A. Cummer, J. B. Pendry, A. F. Starr, and D. R. Smith, "Metamaterial Electromagnetic Cloak at Microwave Frequencies," *Science*, vol. 314, no. 5801, pp. 977–980, Nov. 2006.

[31] C. Caloz, "Metamaterial Dispersion Engineering Concepts and Applications," *Proc. IEEE*, vol. 99, no. 10, pp. 1711–1719, Oct. 2011.

[32] M. A. Antoniades and G. V. Eleftheriades, "Compact linear lead/lag metamaterial phase shifters for broadband applications," *IEEE Antennas and Wireless Propagation Letters*, vol. 2, pp. 103–106, 2003.

[33] ——, "Multiband compact printed dipole antennas using nri-tl metamaterial loading," *IEEE Transactions on Antennas and Propagation*, vol. 60, no. 12, pp. 5613–5626, Dec. 2012.

[34] S. Jamilan, M. A. Antoniades, J. Nourinia, and M. N. Azarmanesh, "A compact multiband printed dipole antenna loaded with two unequal parallel nri-tl metamaterial unit cells," *IEEE Transactions on Antennas and Propagation*, vol. 63, no. 9, pp. 4244–4250, Sep. 2015.

[35] D. Sievenpiper, L. Zhang, R. F. Broas, N. G. Alexopolous, E. Yablonovitch *et al.*, "High-impedance electromagnetic surfaces with a forbidden frequency band," *IEEE Transactions on Microwave Theory and techniques*, vol. 47, no. 11, pp. 2059–2074, 1999.

[36] P. de Maagt, R. Gonzalo, Y. C. Vardaxoglou, and J.-. Baracco, "Electromagnetic bandgap antennas and components for microwave and (Sub)millimeter wave applications," *IEEE Trans. Antennas Propag.*, vol. 51, no. 10, pp. 2667–2677, Oct. 2003.

[37] F.-R. Yang, K.-P. Ma, Y. Qian, and T. Itoh, "A novel tem waveguide using uniplanar compact photonic-bandgap (uc-pbg) structure," *IEEE Transactions on microwave theory and techniques*, vol. 47, no. 11, pp. 2092–2098, 1999.

[38] R. Abhari and G. V. Eleftheriades, "Metallo-dielectric electromagnetic bandgap structures for suppression and isolation of the parallel-plate noise in high-speed circuits," *IEEE Trans. Microw. Theory Techn.*, vol. 51, no. 6, pp. 1629–1639, Jun. 2003.

[39] T. Wu, H. Chuang, and T. Wang, "Overview of Power Integrity Solutions on Package and PCB: Decoupling and EBG Isolation," *IEEE Trans. Electromagn. Compat.*, vol. 52, no. 2, pp. 346–356, May 2010.

[40] M. Kishihara, K. Yamane, I. Ohta, and T. Kawai, "A design of multi-stage, multi-way microstrip power dividers with broadband properties," in *Proc. IEEE MTT-S Int. Microwave Symp. Digest (IEEE Cat. No.04CH37535)*, vol. 1, Jun. 2004, pp. 69–72 Vol.1.

[41] C. Monzon, "A small dual-frequency transformer in two sections," *IEEE Trans. Microw. Theory Techn.*, vol. 51, no. 4, pp. 1157–1161, Apr. 2003.

[42] M. A. Maktoomi, A. P. Yadav, M. S. Hashmi, and F. M. Ghannouchi, "Dual-frequency impedance matching networks based on two-section transmission line," *Antennas Propagation IET Microwaves*, vol. 11, no. 10, pp. 1415–1423, 2017.

[43] K.-. M. Cheng, "A novel approach to the design and implementation of dual-band compact planar 90deg branch-line coupler," *IEEE Trans. Microw. Theory Techn.*, vol. 52, no. 11, pp. 2458–2463, Nov. 2004.

[44] C. Hsu, J. Kuo, and C. Chang, "Miniaturized Dual-Band Hybrid Couplers With Arbitrary Power Division Ratios," *IEEE Trans. Microw. Theory Techn.*, vol. 57, no. 1, pp. 149–156, Jan. 2009.

[45] K. Chin, K. Lin, Y. Wei, T. Tseng, and Y. Yang, "Compact Dual-Band Branch-Line and Rat-Race Couplers With Stepped-Impedance-Stub Lines," *IEEE Trans. Microw. Theory Techn.*, vol. 58, no. 5, pp. 1213–1221, May 2010.

[46] H. Kim, B. Lee, and M. Park, "Dual-Band Branch-Line Coupler With Port Extensions," *IEEE Trans. Microw. Theory Techn.*, vol. 58, no. 3, pp. 651–655, Mar. 2010.

[47] H. Ren, J. Shao, M. Zhou, B. Arigong, J. Ding, and H. Zhang, "Design of dual-band transmission line with flexible phase shifts and its applications," *Electron. Lett.*, vol. 51, no. 3, pp. 261–262, 2015.

[48] M. H. Seko and F. S. Correra, "Dual-band branch-line coupler with shorted stepped-impedance stubs arranged in a Π-shaped topology," *Microwave Opt. Technol. Lett.*, vol. 0, no. 0, Jan. 2019.

[49] L. Wu, Z. Sun, H. Yilmaz, and M. Berroth, "A dual-frequency wilkinson power divider," *IEEE Trans. Microw. Theory Techn.*, vol. 54, no. 1, pp. 278–284, Jan. 2006.

[50] J. Gong, K. Gao, and C. Liang, "Synthesis of a miniaturised wireless local area network dual-band microstrip Wilkinson power divider through a general three-step optimisation process," *Antennas Propagation IET Microwaves*, vol. 9, no. 12, pp. 1274–1278, 2015.

[51] M. A. Maktoomi and M. S. Hashmi, "A Performance Enhanced Port Extended Dual-Band Wilkinson Power Divider," *IEEE Access*, vol. 5, pp. 11 832–11 840, 2017.

[52] N. Gao, G. Wu, and Q. Tang, "Design of a novel compact dual-band wilkinson power divider with wide frequency ratio," *IEEE Microwave and Wireless Components Letters*, vol. 24, no. 2, pp. 81–83, Feb. 2014.

[53] C. Chang, Y. Wei, and K. Chin, "Design of dual-band 90/+90 transmission lines for miniaturized dual-band 1:4 rat-race couplers," in *Proc. IEEE MTT-S Int. Microwave Symp. (IMS)*, Jun. 2017, pp. 1289–1292.

[54] K.-. M. Cheng and Fai-Leung Wong, "A novel rat race coupler design for dual-band applications," *IEEE Microwave and Wireless Components Letters*, vol. 15, no. 8, pp. 521–523, Aug. 2005.

[55] R. Gómez-García, R. Loeches-Sánchez, D. Psychogiou, and D. Peroulis, "Single/multi-band Wilkinson-type power dividers with embedded transversal filtering sections and application to channelized filters," *IEEE Trans. Circuits Syst. I*, vol. 62, no. 6, pp. 1518–1527, Jun. 2015.

[56] L. Piazzon, P. Saad, P. Colantonio, F. Giannini, K. Andersson, and C. Fager, "Branch-Line Coupler Design Operating in Four Arbitrary Frequencies," *IEEE Microw. Wireless Compon. Lett.*, vol. 22, no. 2, pp. 67–69, Feb. 2012.

[57] H. Hashemi and A. Hajimiri, "Concurrent multiband low-noise amplifiers-theory, design, and applications," *IEEE Trans. Microw. Theory Techn.*, vol. 50, no. 1, pp. 288–301, Jan. 2002.

[58] N. Nallam and S. Chatterjee, "Multi-Band Frequency Transformations, Matching Networks and Amplifiers," *IEEE Trans. Circuits Syst. I*, vol. 60, no. 6, pp. 1635–1647, Jun. 2013.

[59] ——, "Design of concurrent multi-band matching networks," in *Proc. IEEE Int. Symp. of Circuits and Systems (ISCAS)*, May 2011, pp. 201–204.

[60] I. Lin, M. DeVincentis, C. Caloz, and T. Itoh, "Arbitrary dual-band components using composite right/left-handed transmission lines," *IEEE Trans. Microw. Theory Techn.*, vol. 52, no. 4, pp. 1142–1149, Apr. 2004.

[61] G. V. Eleftheriades, "A Generalized Negative-Refractive-Index Transmission-Line (NRI amp;ndash;TL) Metamaterial for Dual-Band and Quad-Band Applications," *IEEE Microw. Wireless Compon. Lett.*, vol. 17, no. 6, pp. 415–417, Jun. 2007.

[62] J. Bonache, G. Siso, M. Gil, Iniesta, J. Garcia-Rincon, and F. Martin, "Application of Composite Right/Left Handed (CRLH) Transmission Lines based on Complementary Split Ring Resonators (CSRRs) to the Design of Dual-Band Microwave Components," *IEEE Microw. Wireless Compon. Lett.*, vol. 18, no. 8, pp. 524–526, Aug. 2008.

[63] M. Bemani and S. Nikmehr, "Dual-Band N-Way Series Power Divider Using CRLH-TL Metamaterials With Application in Feeding Dual-Band Linear Broadside Array Antenna With Reduced Beam Squinting," *IEEE Trans. Circuits Syst. I*, vol. 60, no. 12, pp. 3239–3246, Dec. 2013.

[64] S.-. Mao, M.-. Wu, and Y.-. Chueh, "Design of composite right/left-handed coplanar-waveguide bandpass and dual-passband filters," *IEEE Transactions on Microwave Theory and Techniques*, vol. 54, no. 9, pp. 3543–3549, Sep. 2006.

[65] A. Genc and R. Baktur, "Dual- and triple-band wilkinson power dividers based on composite right- and left-handed transmission lines," *Packaging and Manufacturing Technology IEEE Transactions on Components*, vol. 1, no. 3, pp. 327–334, Mar. 2011.

[66] C.-. Chen, C. Y. D. Sim, and Y.-. Wu, "Miniaturised dual-band rat-race coupler with harmonic suppression using synthetic transmission line," *Electronics Letters*, vol. 52, no. 21, pp. 1784–1786, 2016.

[67] J.-S. Hong, *Microstrip Filters for RF / Microwave Applications*. John Wiley & Sons, Jan. 2011, google-Books-ID: Z4sZCf97j_0C.

[68] R. Islam and G. V. Eleftheriades, "A compact highly-selective filter inspired by Negative-Refractive-Index Transmission Lines," in *Proc. IEEE MTT-S Int. Microwave Symp. Digest*, Jun. 2008, pp. 895–898.

[69] ——, "Elliptic-type bandpass filter and bandstop notch filter inspired by metamaterial NRI-TL topology," *Electron. Lett.*, vol. 44, no. 25, pp. 1470–1472, Dec. 2008.

[70] ——, "Compact Negative-Refractive-Index Transmission-Line (NRI-TL) coupler, filter and diplexer," in *Proc. IEEE Antennas and Propagation Society Int. Symp*, Jun. 2007, pp. 4957–4960.

[71] M. Gil, J. Bonache, J. Garcia-Garcia, J. Martel, and F. Martin, "Composite Right/Left-Handed Metamaterial Transmission Lines Based on Complementary Split-Rings Resonators and Their Applications to Very Wideband and Compact Filter Design," *IEEE Trans. Microw. Theory Techn.*, vol. 55, no. 6, pp. 1296–1304, Jun. 2007.

[72] S. Y. Huang and Y. H. Lee, "Tapered dual-plane compact electromagnetic bandgap microstrip filter structures," *IEEE Trans. Microw. Theory Techn.*, vol. 53, no. 9, pp. 2656–2664, Sep. 2005.

[73] I. Reines, S. Park, and G. M. Rebeiz, "Compact Low-Loss Tunable$X$-Band Bandstop Filter With Miniature RF-MEMS Switches," *IEEE Trans. Microw. Theory Techn.*, vol. 58, no. 7, pp. 1887–1895, Jul. 2010.

[74] S. Jeong and J. Lee, "Frequency- and Bandwidth-Tunable Bandstop Filter Containing Variable Coupling Between Transmission Line and Resonator," *IEEE Trans. Microw. Theory Techn.*, vol. 66, no. 2, pp. 943–953, Feb. 2018.

[75] A. Ebrahimi, T. Baum, J. Scott, and K. Ghorbani, "Continuously Tunable Dual-Mode Bandstop Filter," *IEEE Microw. Wireless Compon. Lett.*, vol. 28, no. 5, pp. 419–421, May 2018.

[76] J. Cai, Y. Yang, W. Qin, and J. Chen, "Wideband Tunable Differential Bandstop Filter Based on Double-Sided Parallel-Strip Line," *IEEE Trans. Compon. Packag. Technol.*, vol. 8, no. 10, pp. 1815–1822, Oct. 2018.

[77] H. Deng, L. Sun, F. Liu, Y. Xue, and T. Xu, "Compact Tunable Balanced Bandpass Filter With Constant Bandwidth Based on Magnetically Coupled Resonators," *IEEE Microw. Wireless Compon. Lett.*, pp. 1–3, 2019.

[78] R. J. Cameron, C. M. Kudsia, and R. R. Mansour, *Microwave Filters for Communication Systems: Fundamentals, Design, and Applications.* Wiley, 2018, ch.

Tunable Filters, pp. 731–783. [Online]. Available: https://ieeexplore.ieee.orghttps://ieeexplore.ieee.org/document/8341915

[79] M. A. El-Tanani and G. M. Rebeiz, "Corrugated Microstrip Coupled Lines for Constant Absolute Bandwidth Tunable Filters," *IEEE Trans. Microw. Theory Techn.*, vol. 58, no. 4, pp. 956–963, Apr. 2010.

[80] N. Zahirovic, S. Fouladi, R. R. Mansour, and M. Yu, "Tunable suspended substrate stripline filters with constant bandwidth," in *Proc. IEEE MTT-S Int. Microwave Symp*, Jun. 2011, pp. 1–4.

[81] Y. C. Li and Q. Xue, "Tunable Balanced Bandpass Filter With Constant Bandwidth and High Common-Mode Suppression," *IEEE Trans. Microw. Theory Techn.*, vol. 59, no. 10, pp. 2452–2460, Oct. 2011.

[82] L. Gao, X. Y. Zhang, and Q. Xue, "Compact Tunable Filtering Power Divider With Constant Absolute Bandwidth," *IEEE Trans. Microw. Theory Techn.*, vol. 63, no. 10, pp. 3505–3513, Oct. 2015.

[83] C. Tang and W. Chen, "A Compact Tunable Notch Filter With Wide Constant Absolute Bandwidth," *IEEE Microw. Wireless Compon. Lett.*, vol. 25, no. 3, pp. 151–153, Mar. 2015.

[84] G. Basavarajappa and R. R. Mansour, "Design Methodology of a Tunable Waveguide Filter With a Constant Absolute Bandwidth Using a Single Tuning Element," *IEEE Trans. Microw. Theory Techn.*, vol. 66, no. 12, pp. 5632–5639, Dec. 2018.

[85] S. Nam, B. Lee, C. Kwak, and J. Lee, "A New Class of K-Band High-Q Frequency-Tunable Circular Cavity Filter," *IEEE Trans. Microw. Theory Techn.*, vol. 66, no. 3, pp. 1228–1237, Mar. 2018.

[86] M. D. Hickle and D. Peroulis, "Tunable Constant-Bandwidth Substrate-Integrated Bandstop Filters," *IEEE Trans. Microw. Theory Techn.*, vol. 66, no. 1, pp. 157–169, Jan. 2018.

[87] N. Kumar and Y. K. Singh, "Compact constant bandwidth tunable wideband bpf with second harmonic suppression," *IEEE Microwave and Wireless Components Letters*, vol. 26, no. 11, pp. 870–872, Nov. 2016.

[88] H. Kim, S. Ho, M. Choi, A. B. Kozyrev, and D. W. van der Weide, "Combined Left- and Right-Handed Tunable Transmission Lines With Tunable Passband and 0 ° Phase Shift," *IEEE Trans. Microw. Theory Techn.*, vol. 54, no. 12, pp. 4178–4184, Dec. 2006.

[89] I. Gil, J. Bonache, J. Garcia-Garcia, and F. Martin, "Tunable metamaterial transmission lines based on varactor-loaded split-ring resonators," *IEEE Trans. Microw. Theory Techn.*, vol. 54, no. 6, pp. 2665–2674, Jun. 2006.

[90] H. Jia and R. R. Mansour, "Millimeter-Wave Ultra Wideband Multilayer Superconducting Filter," *IEEE Trans. Appl. Supercond.*, vol. 29, no. 5, pp. 1–5, Aug. 2019.

[91] J. K. A. Everard and K. K. M. Cheng, "High performance direct coupled bandpass filters on coplanar waveguide," *IEEE Trans. Microw. Theory Techn.*, vol. 41, no. 9, pp. 1568–1573, Sep. 1993.

[92] D. M. Pozar, *Microwave Engineering*, 3rd ed. Hoboken, New Jersey, USA: John Wiley & Sons, Inc., 2005.

[93] J. Abdulnour, "Passive Intermodulation and Peak Instantaneous Power: the Importance of Test Techniques for Optimized Antenna Design and Performance," May 2016. [Online]. Available: https://comprodcom.com/wp-content/uploads/2016/05/Comprod_PIM_PIP_White_Paper.pdf

[94] G. Deng, T. Xia, S. Jing, J. Yang, H. Lu, and Z. Yin, "A Tunable Metamaterial Absorber Based on Liquid Crystal Intended for F Frequency Band," *IEEE Antennas Wireless Propag. Lett.*, vol. 16, pp. 2062–2065, 2017.

[95] A. L. Borja, J. Carbonell, J. D. Martinez, V. E. Boria, and D. Lippens, "A Controllable Bandwidth Filter Using Varactor-Loaded Metamaterial-Inspired Transmission Lines," *IEEE Antennas Wireless Propag. Lett.*, vol. 10, pp. 1575–1578, 2011.

[96] L. Kurra, M. P. Abegaonkar, A. Basu, and S. K. Koul, "Switchable and tunable notch in ultra-wideband filter using electromagnetic bandgap structure," *IEEE Microwave and Wireless Components Letters*, vol. 24, no. 12, pp. 839–841, Dec. 2014.

[97] R. Chadha and K. C. Gupta, "Compensation of Discontinuities in Planar Transmission Lines," *IEEE Trans. Microw. Theory Techn.*, vol. 30, no. 12, pp. 2151–2156, Dec. 1982.

[98] "Framework for the Use of Certain Non-broadcasting Applications in the Television Broadcasting Bands Below 698 MHz," https://www.ic.gc.ca/eic/site/smt-gst.nsf/vwapj/TVWhiteSpace-October2012.pdf/$file/TVWhiteSpace-October2012.pdf, Oct. 2012, accessed: Sept. 17, 2019.

[99] P. Laforge, R. R. Mansour, and G. A. Morin, "Tunable filters with a constant bandwidth," in *Proc. 10th Int. Symp. Antenna Technology and Applied Electromagnetics and URSI Conf*, Jul. 2004, pp. 1–4.

[100] "Overview of materials for Acrylonitrile Butadiene Styrene (ABS), Extruded," http://www.matweb.com/search/DataSheet.aspx?MatGUID=3a8afcddac864d4b8f58d40570d2e5aa&ckck=1, accessed: Sept. 17, 2019.

Appendix A

MTM-EBG Equivalent Circuit Parametric Results

A summary of the parametric results of this appendix are provided in Table 2.1. The studies performed here done on both MTM-EBG layouts, which are shown in Figs. 2.2 and 2.4. Other than the parameter indicated in the results, all other parameters were identical to those provided in Table A.1. These studies are meant to serve as a guide as to how to design and tune the response of the MTM-EBG. Preliminary studies were performed on individual parameters of the MTM-EBG.

CPW Stripline

The first parameter to be examined is the CPW stripline (s), and the results are provided in Figs. A.1(a) and A.1(b). It should be immediately apparent that depending on which configuration of the MTM-EBG is used, a change in s has a different effect. When the capacitor is placed in the CPW ground conductors, as it is in Fig. 2.2, an increase in s will

Table A.1: Base parameters used in the parametric studies.

s	g	W	d	C	L	h	ϵ_r
1.0 mm	0.4 mm	3.8 mm	12 mm	0.35 pF	0.2 nH	1.524 mm	3.0

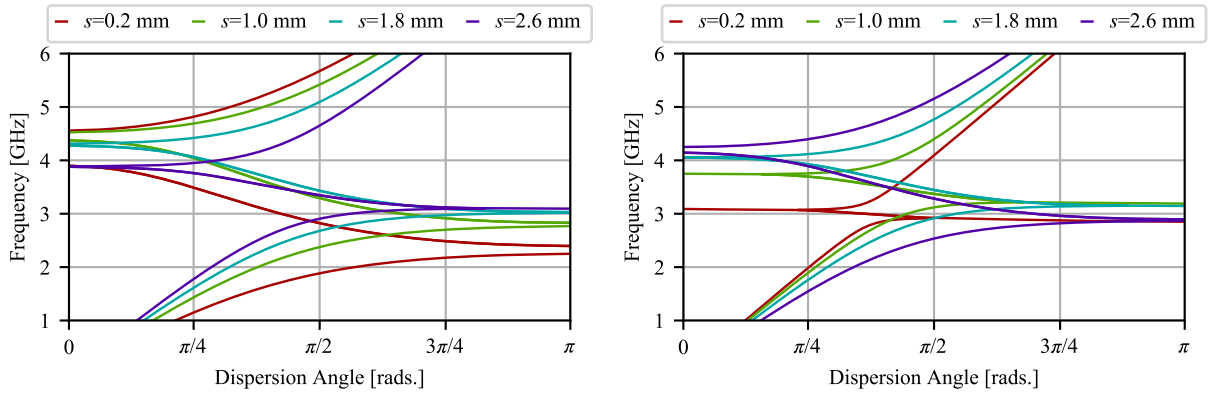

(a) (b)

Figure A.1: Effect of varying the CPW stripline (s) of an MTM-EBG with a layout of a) Fig. 2.2 and b) Fig. 2.4.

reduce the size of the bandgap and cause the two 90° frequencies to shift closer together. If the capacitor is placed in the CPW stripline, the exact opposite trend can be observed. In fact, as s approaches the total width W the MTM-EBG with a CPW stripline capacitor will have a larger bandgap. This represents a practical limit on the realizable bandgaps for a given MTM-EBG layout.

CPW gap

Changing the CPW gap (g) has distinctly different effect on the dispersion of both configurations of MTM-EBGs. These results are provided in Figs. A.2(a) and A.2(b). When the capacitor is placed in the CPW ground conductors (Fig. 2.2), increases in g generally reduce the size of the bandgap and shift the center frequency down. It does this by largely affecting the upper 90° phase point and minimally affecting the lower phase. The same is generally true when the capacitor is in the CPW stripline (Fig. 2.4); however, the lower frequency is generally more strongly affected.

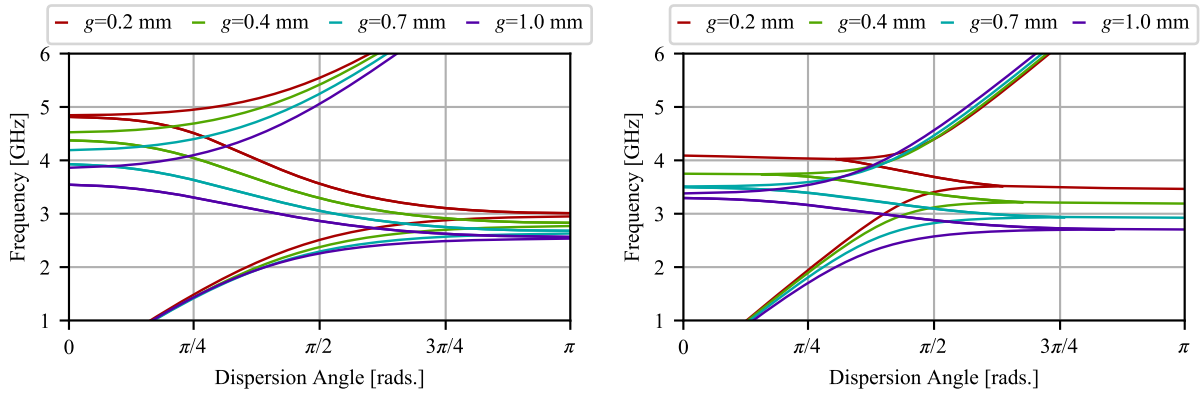

(a) (b)

Figure A.2: Effect of varying the CPW gap (g) of an MTM-EBG with a layout of a) Fig. 2.2 and b) Fig. 2.4.

Total Width

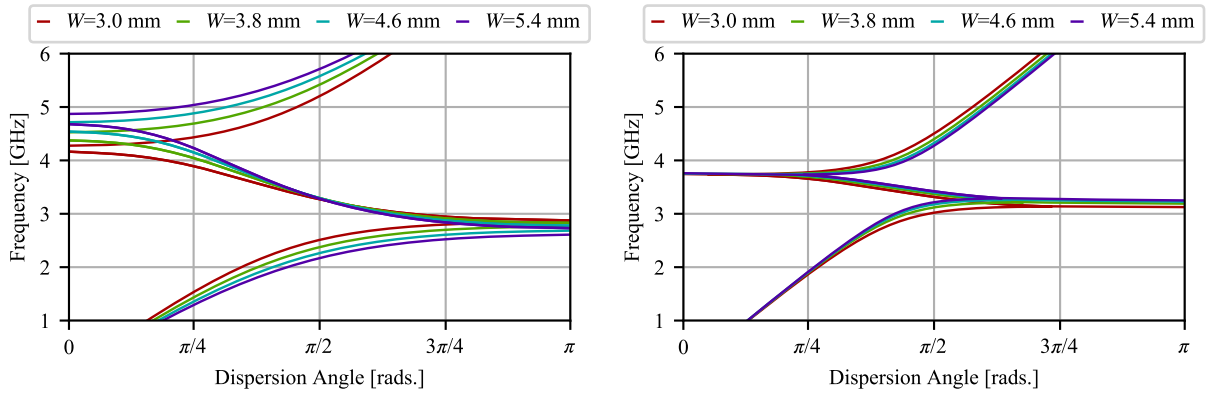

(a) (b)

Figure A.3: Effect of varying the width (W) of an MTM-EBG with a layout of a) Fig. 2.2 and b) Fig. 2.4.

The effect of changing the total width of the MTM-EBG is sensitive the to position of the capacitor, similar to the CPW stripline. When the capacitor is placed in the CPW ground conductors, as it has been done in Fig. 2.2, increasing the width of the MTM-EBG causes the bandgap to widen and subsequently shifts the two 90° operating frequencies apart. The opposite is true when the capacitance is placed in the CPW stripline, as it has been done in Fig. 2.2.

Unit Cell Length

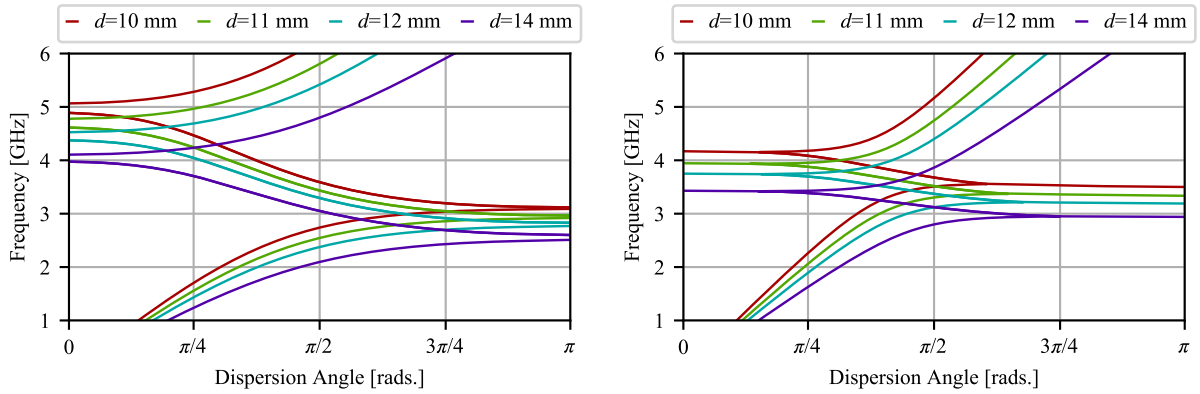

(a) (b)

Figure A.4: Effect of varying the length (d) of an MTM-EBG with a layout of a) Fig. 2.2 and b) Fig. 2.4.

The effect of the unit cell length d is more or less independent of the position of the capacitor, as shown in Figs. A.4(a) and A.4(b). In each MTM-EBG configuration, increasing d causes the bandgap and both 90° frequencies to shift downwards at approximately the same rate.

Series Capacitance

While changing the series capacitance C affects the bandgap and 90° frequencies in a similar manner to that of the length d, there are some notable differences in the response. As shown in Fig. A.5(a), when the capacitance is placed in the CPW ground conductors increasing this capacitance will cause the bandgap to downshift and decrease in width while largely affecting only the upper 90° frequency. The same behavior can be observed when the capacitance is in the CPW stripline, as shown in Fig. A.5(b), but changes in C affect both 90° frequencies.

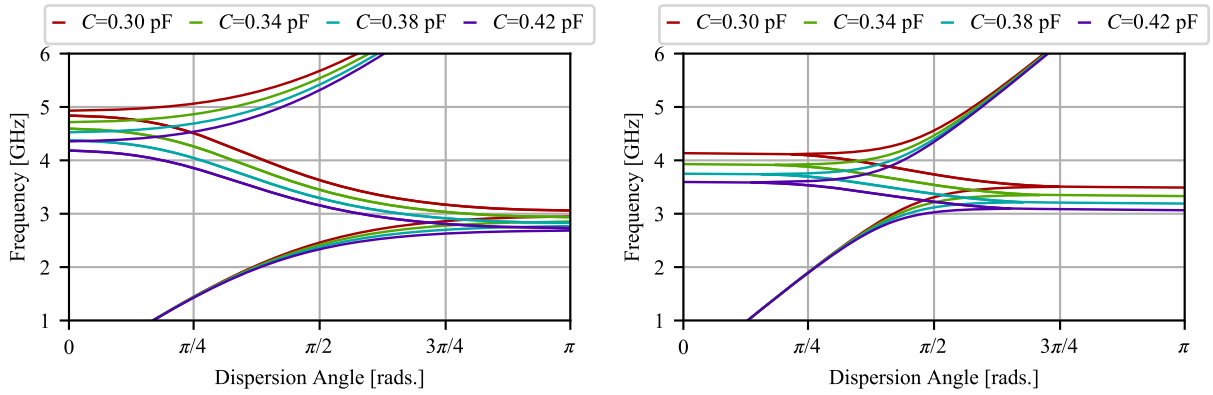

(a) (b)

Figure A.5: Effect of varying the capacitance (C) of an MTM-EBG with a layout of a) Fig. 2.2 and b) Fig. 2.4.

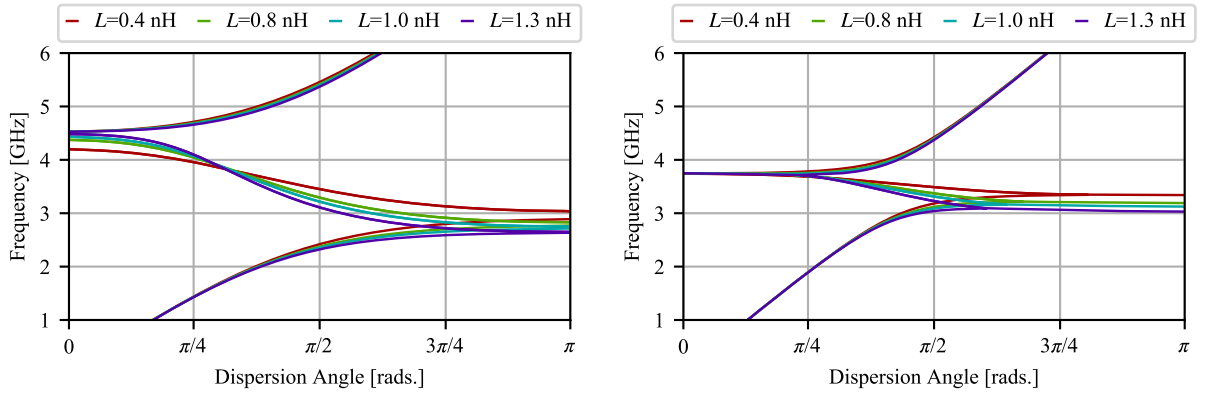

(a) (b)

Figure A.6: Effect of varying the inductance (L) of an MTM-EBG with a layout of a) Fig. 2.2 and b) Fig. 2.4.

Shunt Inductance

The shunt inductance has a negligible effect on the performance of both configurations of MTM-EBGs as shown in Figs. A.6(a) and A.6(a). Depending on whether the capacitance is in the CPW grounds or stripline, the bandedge which is affected changes.

Relative Permittivity and Substrate Height

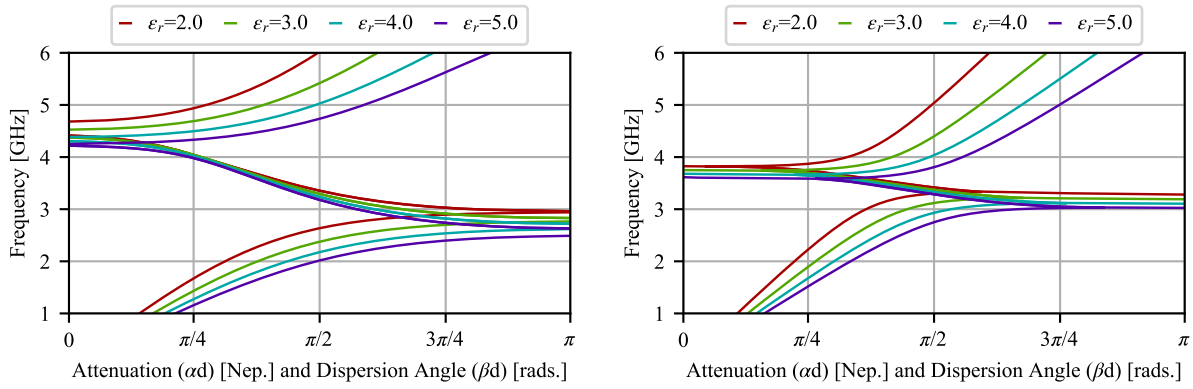

(a) (b)

Figure A.7: Effect of varying the CPW host permittivity (ϵ_r) of an MTM-EBG with a layout of a) Fig. 2.2 and b) Fig. 2.4.

As shown in Figs. A.7(a) and A.7(b), the permittivity of the MTM-EBGs host medium has an nearly identical effect on both MTM-EBG configurations. In both designs, increasing ϵ_r shifts the bandgap down; however, depending on the position of the capacitor, the width of the bandgap will either remain constant or increase. Conversely, as shown in Figs. A.8(a) and A.8(b), the height of the dielectric substrate has almost no effect on the performance outside of a slight narrowing of the bandgap for increasing thickness.

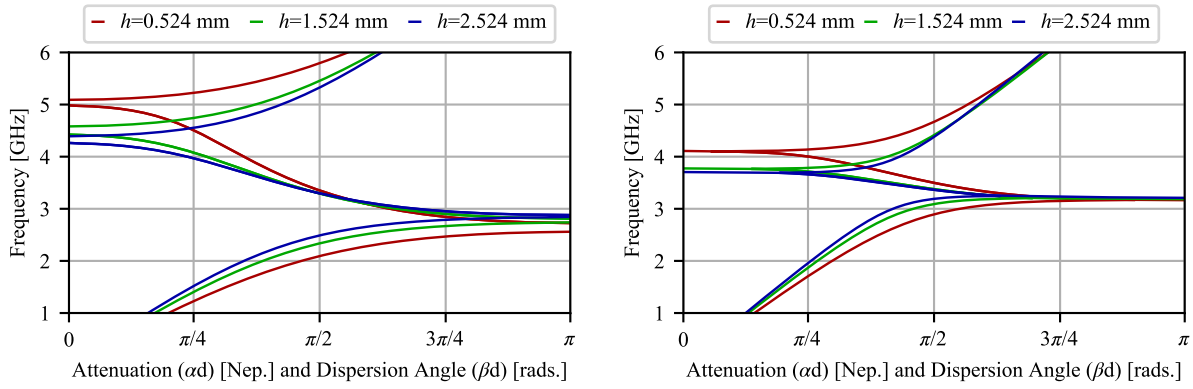

(a) (b)

Figure A.8: Effect of varying the CPW host thickness (h) of an MTM-EBG with a layout of a) Fig. 2.2 and b) Fig. 2.4.

Appendix B

Analytical equations to determine the necessary MTM-EBG loading

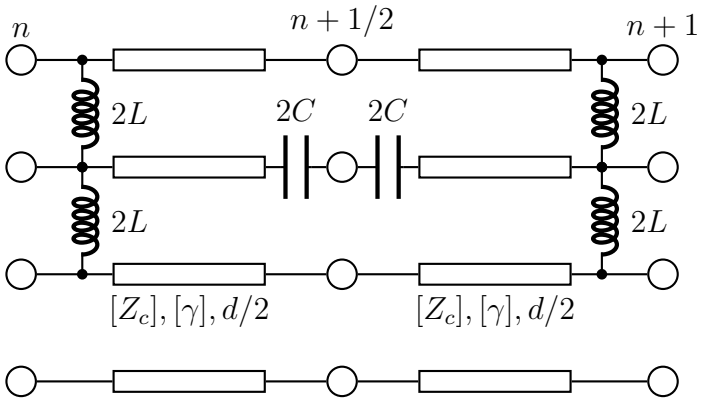

Figure B.1: Equivalent Circuit Model used to determine expressions for the cut-off frequencies of the MTM-EBG.

The MTM-EBG is typically analyzed purely on the basis of the equivalent circuit diagram. This is largely a result of the complexity of the underlying MTL host medium. However, there has been work done in the past which successfully derived quasi-closed form expressions for the cut-off frequencies of an MTM-EBG. Specifically, in [18], expressions for the cut-off frequencies of a shielded Sievenpiper mushroom are derived. The relevant frequencies are indicated on Fig. B.2 and represent some of the $\Gamma-$ ($\beta d = 0$) and X$-$ ($\beta d = \pi$) points of the MTM-EBG. Two additional frequencies are indicated on Fig. B.2 (f_{c1} and f_{c2}) but these generally do not overlap with f_1 and f_2; the overlap observed here is purely coincidental and breaks down with increasing inductance.

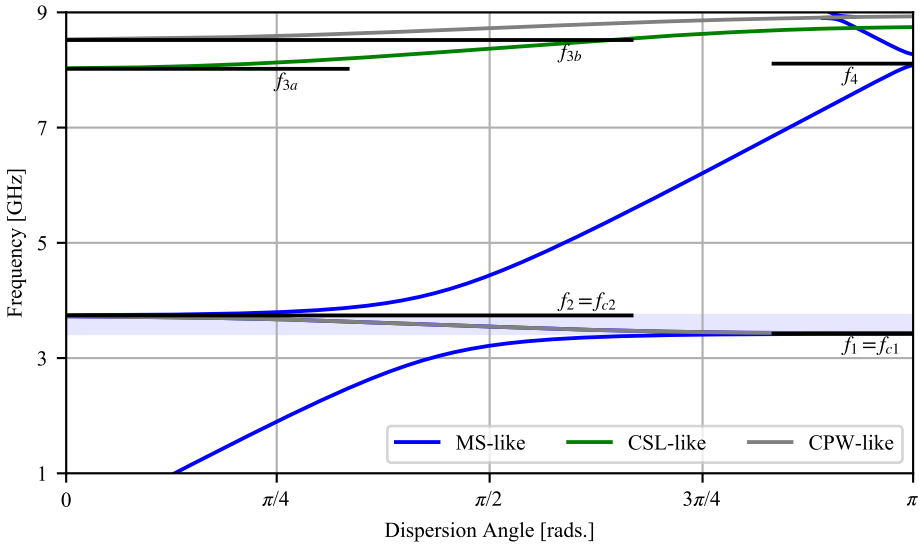

Figure B.2: Dispersion diagram for a unit cell with dimensions: s=1.0 mm, g=0.4 mm, W=3.8 mm, d=12 mm, C=0.38 pF, L=0.1 nH, ϵ_r=3, and h=1.524 mm. The relevant X- and Γ-frequencies are labelled as f_1 and f_2, which have values of 3.422 and 3.744 GHz respectively.

Shown in Fig. B.3 is a summary of these conditions from [18]. Each condition indicates a situation where each output port is terminated in either a short circuit or open circuit. This is further restricted by specifying a termination at the unit cell half-point, thereby representing either a full wavelength or half-wavelength resonance condition. Each of the resulting four conditions [(B.1a), (B.1b), (B.1c), and (B.1d)] can be calculated by evaluating the determinant of each of the block matrices of the half-cell chain matrix ($[A_h]$, $[B_h]$, $[C_h]$ and $[D_h]$) of the MTM-EBG. Prior to finishing this derivation and analyzing the resulting expressions, it is not possible to determine which of the four cases is related to each frequency. As such, they will be distinguished by either an f_X, which is either f_1 or f_4, or an f_Γ, which is either f_2 or f_3.

$$\det|[A]| = 0 \tag{B.1a}$$

Boundary Conditions		Formula	Non-Zero Variables	phase shift / frequency
$\mathbf{V}_n = \mathbf{V}_{n+1} = \mathbf{0}$ $\mathbf{I}_{n+\frac{1}{2}} = \mathbf{0}$	$\Rightarrow$	$\det(\mathbf{A}_h) = 0$	$\mathbf{A}_h\mathbf{V}_{n+\frac{1}{2}} = \mathbf{0}$ $\mathbf{I}_n = \mathbf{C}_h\mathbf{V}_{n+\frac{1}{2}}$ $\mathbf{I}_{n+1} = -\mathbf{I}_n$	$(\beta d)_x = \pi$ (f_1 or f_4)
$\mathbf{V}_n = \mathbf{V}_{n+1} = \mathbf{0}$ $\mathbf{V}_{n+\frac{1}{2}} = \mathbf{0}$	$\Rightarrow$	$\det(\mathbf{B}_h) = 0$	$\mathbf{B}_h\mathbf{I}_{n+\frac{1}{2}} = \mathbf{0}$ $\mathbf{I}_n = \mathbf{D}_h\mathbf{I}_{n+\frac{1}{2}}$ $\mathbf{I}_{n+1} = \mathbf{I}_n$	$(\beta d)_x = 0$ (f_2 or f_3)
$\mathbf{I}_n = \mathbf{I}_{n+1} = \mathbf{0}$ $\mathbf{I}_{n+\frac{1}{2}} = \mathbf{0}$	$\Rightarrow$	$\det(\mathbf{C}_h) = 0$	$\mathbf{C}_h\mathbf{V}_{n+\frac{1}{2}} = \mathbf{0}$ $\mathbf{V}_n = \mathbf{A}_h\mathbf{V}_{n+\frac{1}{2}}$ $\mathbf{V}_{n+1} = \mathbf{V}_n$	$(\beta d)_x = 0$ (f_3 or f_2)
$\mathbf{I}_n = \mathbf{I}_{n+1} = \mathbf{0}$ $\mathbf{V}_{n+\frac{1}{2}} = \mathbf{0}$	$\Rightarrow$	$\det(\mathbf{D}_h) = 0$	$\mathbf{D}_h\mathbf{I}_{n+\frac{1}{2}} = \mathbf{0}$ $\mathbf{V}_n = \mathbf{B}_h\mathbf{I}_{n+\frac{1}{2}}$ $\mathbf{V}_{n+1} = -\mathbf{V}_n$	$(\beta d)_x = \pi$ (f_4 or f_1)

Figure B.3: Resonant conditions for the cut-off frequencies of a symmetric MTM unit cell. Taken from [18].

$$\det|[B_h]| = 0 \tag{B.1b}$$

$$\det|[C_h]| = 0 \tag{B.1c}$$

$$\det|[D_h]| = 0 \tag{B.1d}$$

As will be demonstrated in this chapter, it is not possible to re-organize the above equations to directly determine the cut-off frequencies that would result from a given loading. Instead, it will be shown that given a desired edge frequency and host geometry, the above conditions may be used to determine the necessary loading values. The subscript k is used in the following derivation to specify that the matrix has been evaluated at frequency f_k, where $k \in \{1, 2, 3, 4\}$.

B.1 Chain Matrix Derivation

Applying the analysis of [36] requires the individual components of the MTM-EBG to first be modelled as chain matrices. This first requires a mechanism of modelling the properties of the underlying MTL host medium. Similar to two-conductor TLs, this is done by determing

the RLGC matrix parameters that describe the MTL host medium. For simple geometries, analytical expressions may be available; however, for more complex geometries such as the host of the MTM-EBG (CBCPW), numerical solutions may be preferred.

The connecting lengths of unloaded MTL host medium are well modelled in [12] and, in the voltage domain, are defined as (B.2), where $[\gamma]_k$ represents the terminal domain propagation matrix of the host medium at f_k. $[Z_c]$ represents the terminal domain characteristic impedance matrix and, generally, is frequency independent:

$$[T]_k = \begin{bmatrix} \cosh\left([\gamma]_k l\right) & \sinh\left([\gamma]_k l\right)[Z_c] \\ [Z_c]^{-1}\sinh\left([\gamma]_k l\right) & [Z_c]^{-1}\cosh\left([\gamma]_k l\right)[Z_c] \end{bmatrix} = \begin{bmatrix} [A]_k & [B]_k \\ [C]_k & [D]_k \end{bmatrix} \tag{B.2}$$

A similar expression can be derived for the series capacitor and shunt inductor elements. They are shown for the series and shunt elements in (B.3) and (B.4), respectively.

$$[T_C]_k = \begin{bmatrix} \hat{1} & Z_k[Z'_{se}] \\ \hat{0} & \hat{1} \end{bmatrix} \tag{B.3}$$

$$[T_L]_k = \begin{bmatrix} \hat{1} & \hat{0} \\ Y_k[Y'_{sh}] & \hat{1} \end{bmatrix} \tag{B.4}$$

$[Z'_{se}]$ and $[Y'_{sh}]$ have a very specific form that is defined based on how the reactive elements are connected to the conductors of the MTL host medium. In (B.3), $[Z'_{se}]$ depends on the

position of the capacitor. For the case where the capacitor is in the CPW stripline, which is the case examined here and is shown in Fig. 2.4, results in $[Z'_{se}]$ of (B.5):

$$[Z'_{se}] = \begin{bmatrix} 0 & 0 & 0 \\ 0 & 1 & 0 \\ 0 & 0 & 0 \end{bmatrix} \tag{B.5}$$

For the MTM-EBG where the inductors are only placed between the upper conductors (Fig. 2.2 and 2.4), the $[Y'_{sh}]$ always has the form:

$$[Y'_{sh}] = \begin{bmatrix} 1 & -1 & 0 \\ -1 & 2 & -1 \\ 0 & -1 & 1 \end{bmatrix} \tag{B.6}$$

(B.2), (B.3) and (B.4) can then be cascaded to form the half unit cell chain matrix as shown in (B.7).

$$\begin{aligned} [T_h]_k = [T_L]_k[T]_k[T_C]_k &= \begin{bmatrix} [A]_k & Z_k[A]_k[Z'_{se}] + [B]_k \\ Y_k[Y'_{sh}][A]_k + [C]_k & \left(Y_k[Y'_{sh}][A]_k + [C]_k\right) Z_k[Z'_{se}] + Y_k[Y'_{sh}][B]_k + [D]_k \end{bmatrix} \\ &= \begin{bmatrix} [A_h]_k & [B_h]_k \\ [C_h]_k & [D_h]_k \end{bmatrix} \end{aligned} \tag{B.7}$$

B.2 Derivation of the expressions

Case 1: $\det[A_h]_{1,4} = 0$

The first, and easiest, case to examine is that defined in Equation (B.1a). Since $[A_h]_{1,4}$ is equal to $[A]_{1,4}$, this has a well defined form and is practical to directly evaluate the determinant. This is shown in Equation (B.8):

$$\begin{aligned}\det[A]_{1,4} &= \det\left(\cosh\left([\gamma]_{1,4}l\right)\right) = \det\frac{T_v(e^{[\gamma_d]_{1,4}l} + e^{-[\gamma_d]_{1,4}l})T_v^{-1}}{2} \\ &= \det T_v \det\frac{(e^{[\gamma_d]_{1,4}l} + e^{-[\gamma_d]_{1,4}l})}{2}\frac{1}{\det T_v} = \det\left(e^{[\gamma_d]_{1,4}l} + e^{-[\gamma_d]_{1,4}l}\right) = 0 \end{aligned} \quad \text{(B.8)}$$

This can further be expanded into a polynomial expression for solutions of γ_i, which can then be evaluated to determine the corresponding f. Evaluating this expression finds that solutions must occur when $\gamma_i l = \pi/2$. Since the periodicity of the unit cell is $d = 2l$, this solution corresponds to situations where the total cell length is one half-wavelength and appear to represent frequency f_4 on Fig. B.2.

Determinant Properties

The remaining cases do not reduce as concisely as (B.8) due to the fact that, generally, $\det|A + B| \neq \det|A| + \det|B|$. It is possible however to re-arrange the remaining cases into a form where the loading values may be calculated from a desired cut-off frequency and

known host medium. In order to do this, two properties of determinants are employed: the first states that if row/column i/j of a given matrix can be expressed as a sum of different row/columns u and v, the determinant can be calculated as:

$$\begin{aligned}\det|G| &= \det\begin{bmatrix}\bar{G}_1 & \dots & \bar{G}_m & \dots & \bar{G}_n\end{bmatrix} \\ &= \det\begin{bmatrix}\bar{G}_1 & \dots & \bar{v}+\bar{u} & \dots & \bar{G}_n\end{bmatrix} \\ &= \det\begin{bmatrix}\bar{G}_1 & \dots & \bar{v} & \dots & \bar{G}_n\end{bmatrix} + \det\begin{bmatrix}\bar{G}_1 & \dots & \bar{u} & \dots & \bar{G}_n\end{bmatrix}\end{aligned} \tag{B.9a}$$

The second property relates to the effect of a scaling factor on a given row. If a single row/column is multiplied by a scaling factor (k), the resulting determinant is equal to:

$$\begin{aligned}\det|G| &= \det\begin{bmatrix}\bar{G}_1 & \dots & k\bar{G}_m & \dots & \bar{G}_n\end{bmatrix} \\ &= k\det\begin{bmatrix}\bar{G}_1 & \dots & \bar{G}_m & \dots & \bar{G}_n\end{bmatrix}\end{aligned} \tag{B.10a}$$

If m rows/columns of the matrix are scaled by the same factor, it instead multiples the determinant by a factor of k^m. These two properties are used extensively in the remaining cases to separate and isolate the loading in order to determine expressions for this loading as a function of the swapped transmission matrices.

Case 2: $\det[B_h]_{2,3} = 0$

As we are assuming the capacitor was placed in the CPW stripline, which causes $[Z'_{se}]$ to look like (B.3), additional simplifications can be made to (B.1b). The product of $[Z'_{se}]$ and another matrix results in matrix that contains only a single **non-zero** column vector, which correspond to conductors with the capacitor. As a result of this, the determinant of (B.1b) can be simplified to B.11, where $\bar{b}_{1,2,3}$ are the column vectors of $[B]_{2,3}$, which is evaluated at $f_{2,3}$:

$$\begin{aligned}
\det[B_h]_{2,3} &= \det\left(Z_{2,3}[A]_{2,3}[Z'_{se}] + [B]_{2,3}\right) \\
&= \det\begin{bmatrix} \bar{b}_1 & \bar{b}_2 + Z_{2,3}\bar{a}_2 & \bar{b}_3 \end{bmatrix} \\
&= Z_{2,3}\det\begin{bmatrix} \bar{b}_1 & \bar{a}_2 & \bar{b}_3 \end{bmatrix} + \det[B]_{2,3} = 0 \qquad \text{(B.11)} \\
\therefore Z_{2,3} &= -\frac{\det[B]_{2,3}}{\det\begin{bmatrix} \bar{b}_1 & \bar{a}_2 & \bar{b}_3 \end{bmatrix}} \qquad \text{(B.12)}
\end{aligned}$$

While $Z_{2,3}$ is generally complex, the real part is primarily due to numerical errors. As such, it is ignored when finding the loading capacitance C in (B.13):

$$C = -\frac{1}{4\pi f_{2,3}\mathrm{Im}(Z_{2,3})} \qquad \text{(B.13)}$$

Case 3: $\det[C_h]_{2,3} = 0$

Similar expressions for each of the remaining cases can be determined here using an identical analysis; however, they result in substantially more complicated expressions than what is provided in (B.13). The solution to (B.1c) is shown in (B.16), $\bar{c}_{1,2,3}$ are the column vectors of $[C]_{2,3}$, which is evaluated again at $f_{2,3}$:

$$\begin{aligned}
\det[C_h]_{2,3} &= \det\left(Y_{2,3}[Y'_{sh}][A]_{2,3} + [C]_{2,3}\right) \\
[Y'_{sh}][A]_{2,3} &= \begin{bmatrix} \bar{\delta}_1 & \bar{\delta}_2 & \bar{\delta}_3 \end{bmatrix} \qquad \text{(B.14a)} \\
\therefore \det[C_h]_{2,3} &= \det\begin{bmatrix} \bar{c}_1 + Y_{2,3}\bar{\delta}_1 & \bar{c}_2 + Y_{2,3}\bar{\delta}_2 & \bar{c}_3 + Y_{2,3}\bar{\delta}_3 \end{bmatrix} \qquad \text{(B.14b)} \\
&= \det[C]_{2,3} + \det\begin{bmatrix} \bar{c}_1 & \bar{c}_2 & Y_{2,3}\bar{\delta}_3 \end{bmatrix} + \det\begin{bmatrix} \bar{c}_1 & Y_{2,3}\bar{\delta}_2 & \bar{c}_3 \end{bmatrix} + \det\begin{bmatrix} Y_{2,3}\bar{\delta}_1 & \bar{c}_2 & \bar{c}_3 \end{bmatrix} \\
&\quad + \det\begin{bmatrix} \bar{c}_1 & Y_{2,3}\bar{\delta}_2 & Y_{2,3}\bar{\delta}_3 \end{bmatrix} + \det\begin{bmatrix} Y_{2,3}\bar{\delta}_1 & \bar{c}_2 & Y_{2,3}\bar{\delta}_3 \end{bmatrix} + \det\begin{bmatrix} Y_{2,3}\bar{\delta}_1 & Y_{2,3}\bar{\delta}_2 & \bar{c}_3 \end{bmatrix} \\
&\quad + \cancelto{0}{\det[Y_{sh}][A]} \\
&= \det[C] + \left(\det\begin{bmatrix} \bar{c}_1 & \bar{c}_2 & \bar{\delta}_3 \end{bmatrix} + \det\begin{bmatrix} \bar{c}_1 & \bar{\delta}_2 & \bar{c}_3 \end{bmatrix} + \det\begin{bmatrix} \bar{\delta}_1 & \bar{c}_2 & \bar{c}_3 \end{bmatrix}\right) Y_{2,3} \\
&\quad + \left(\det\begin{bmatrix} \bar{c}_1 & \bar{\delta}_2 & \bar{\delta}_3 \end{bmatrix} + \det\begin{bmatrix} \bar{\delta}_1 & \bar{c}_2 & \bar{\delta}_3 \end{bmatrix} + \det\begin{bmatrix} \bar{\delta}_1 & \bar{\delta}_2 & \bar{c}_3 \end{bmatrix}\right) Y_{2,3}^2 \\
&= l_1 Y_{2,3}^2 + m_1 Y_{2,3} + n_1 = 0 \qquad \text{(B.14c)}
\end{aligned}$$

$$\therefore Y_{2,3}^{(\pm)} = \frac{-m_1 \pm \sqrt{m_1^2 + 4l_1 n_1}}{2l_1} \qquad \text{(B.15)}$$

Similar to $Z_{2,3}$ in (B.12), $Y_{2,3}^{(\pm)}$ is a complex number with an overwhelmingly large imaginary

portion. The inductance can then be calculated as:

$$L^{(\pm)} = -\frac{1}{4\pi f_{2,3}\mathrm{Im}(Y_{2,3}^{\pm})} \tag{B.16}$$

As is apparent in (B.15), there are two possible solutions. In Fig. B.2 there are two high frequency Γ-points indicated (f_{3a} and f_{3b}). As such, each of the solutions to (B.15) corresponds to the loading inductance required to place **either** f_{3a} or f_{3b} at the specified location. Initial evaluation of this function indicate that it has two realizable (i.e. positive) and large L values. This suggests that f_2, which is the upper cut-off frequency of the actual bandgap, is related to (B.13).

Case 4: $\det[D_h]_1 = 0$

Since we have determined that f_4 is defined by solutions to (B.1a), solutions to (B.1d) are prescribed by f_1, so we specify this frequency in all matrices. To find these solutions is more arduous than either of the previous cases. This derivation is started by defining the following matrix products as a set of column vectors, similar to the previous cases:

$$[Y_s'h][A]_1 = \begin{bmatrix} \bar{\delta'}_1 & \bar{\delta'}_2 & \bar{\delta'}_3 \end{bmatrix} \tag{B.17a}$$

$$[Y_{sh}'][B]_1 = \begin{bmatrix} \bar{\mu}_1 & \bar{\mu}_2 & \bar{\mu}_3 \end{bmatrix} \tag{B.17b}$$

(B.1d) can now be further re-arranged as follows, where $\bar{d}_{1,2,3}$ are the column vectors of $[D]_1$, $\bar{c'}_2$ is the 2nd column vector of $[C]_1$, and $\bar{\Delta} = Y_1\bar{\mu}_2 + Z_1(Y_1\bar{\delta'}_2 + \bar{c'}_2)$:

$$\begin{aligned}
\det[D_h]_1 &= \begin{bmatrix} \bar{d}_1 + Y_1\bar{\mu}_1 & \bar{d}_2 + \bar{\Delta} & \bar{d}_3 + Y_1\bar{\mu}_3 \end{bmatrix} \\
&= \det[D]_1 + Y_1\det\begin{bmatrix} \bar{d}_1 & \bar{d}_2 & \bar{\mu}_3 \end{bmatrix} + Y_1\det\begin{bmatrix} \bar{\mu}_1 & \bar{d}_2 & \bar{d}_3 \end{bmatrix} + Y_1^2\det\begin{bmatrix} \bar{\mu}_1 & \bar{d}_2 & \bar{\mu}_3 \end{bmatrix} \\
&\quad + \det\begin{bmatrix} \bar{d}_1 & \bar{\Delta} & \bar{d}_3 \end{bmatrix} + Y_1\det\begin{bmatrix} \bar{d}_1 & \bar{\Delta} & \bar{\mu}_3 \end{bmatrix} + Y_1\det\begin{bmatrix} \bar{\mu}_1 & \bar{\Delta} & \bar{d}_3 \end{bmatrix} \\
&\quad + Y_1^2\det\begin{bmatrix} \bar{\mu}_1 & \bar{\Delta} & \bar{\mu}_3 \end{bmatrix} \\
&= \det[D]_1 + Y_1\det\begin{bmatrix} \bar{d}_1 & \bar{d}_2 & \bar{\mu}_3 \end{bmatrix} + Y_1\det\begin{bmatrix} \bar{\mu}_1 & \bar{d}_2 & \bar{d}_3 \end{bmatrix} + Y_1^2\det\begin{bmatrix} \bar{\mu}_1 & \bar{d}_2 & \bar{\mu}_3 \end{bmatrix} \\
&\quad + \Delta_{LC}
\end{aligned} \tag{B.18a}$$

The expansion of Δ_{LC} incorporates both the series and shunt loading, and expands into:

$$\begin{aligned}
\Delta_{LC} &= Y_1\det\begin{bmatrix} \bar{d}_1 & \bar{\mu}_2 & \bar{d}_3 \end{bmatrix} + Y_1^2\det\begin{bmatrix} \bar{d}_1 & \bar{\mu}_2 & \bar{\mu}_3 \end{bmatrix} + Y_1^2\det\begin{bmatrix} \bar{\mu}_1 & \bar{\mu}_2 & \bar{d}_3 \end{bmatrix} \\
&\quad + Z_1\det\begin{bmatrix} \bar{d}_1 & \bar{c'}_2 & \bar{d}_3 \end{bmatrix} + Y_1Z_1\det\begin{bmatrix} \bar{d}_1 & \bar{c'}_2 & \bar{\mu}_3 \end{bmatrix} + Y_1Z_1\det\begin{bmatrix} \bar{d}_1 & \bar{\delta'}_2 & \bar{d}_3 \end{bmatrix} \\
&\quad + Y_1Z_1\det\begin{bmatrix} \bar{\mu}_1 & \bar{c'}_2 & \bar{d}_3 \end{bmatrix} + Y_1^2Z_1\det\begin{bmatrix} \bar{\mu}_1 & \bar{\delta'}_2 & \bar{d}_3 \end{bmatrix} + Y_1^2Z_1\det\begin{bmatrix} \bar{d}_1 & \bar{\delta'}_2 & \bar{\mu}_3 \end{bmatrix} \\
&\quad + Y_1^2Z_1\det\begin{bmatrix} \bar{\mu}_1 & \bar{c'}_2 & \bar{\mu}_3 \end{bmatrix}
\end{aligned} \tag{B.19}$$

Substituting (B.19) into (B.18a), and re-arranging results in (B.20a):

$$\det[D_h]_1 = l_2 Y_1^2 + m_2 Y_1 + n_2 + Z_1(l_2' Y_1^2 + m_2' Y_1 + n_2') = 0 \tag{B.20a}$$

where :

$$l_2 = \det\begin{bmatrix} \bar{d}_1 & \bar{\mu}_2 & \bar{\mu}_3 \end{bmatrix} + \det\begin{bmatrix} \bar{\mu}_1 & \bar{d}_2 & \bar{\mu}_3 \end{bmatrix} + \det\begin{bmatrix} \bar{\mu}_1 & \bar{\mu}_2 & \bar{d}_3 \end{bmatrix} \tag{B.20b}$$

$$m_2 = \det\begin{bmatrix} \bar{\mu}_1 & \bar{d}_2 & \bar{d}_3 \end{bmatrix} + \det\begin{bmatrix} \bar{d}_1 & \bar{\mu}_2 & \bar{d}_3 \end{bmatrix} + \det\begin{bmatrix} \bar{d}_1 & \bar{d}_2 & \bar{\mu}_3 \end{bmatrix} \tag{B.20c}$$

$$n_2 = \det[D]_1 \tag{B.20d}$$

$$l_2' = \det\begin{bmatrix} \bar{\mu}_1 & \bar{\delta'}_2 & \bar{d}_3 \end{bmatrix} + \det\begin{bmatrix} \bar{d}_1 & \bar{\delta'}_2 & \bar{\mu}_3 \end{bmatrix} + \det\begin{bmatrix} \bar{\mu}_1 & \bar{c}_2 & \bar{\mu}_3 \end{bmatrix} \tag{B.20e}$$

$$m_2' = \det\begin{bmatrix} \bar{\mu}_1 & \bar{c}_2 & \bar{d}_3 \end{bmatrix} + \det\begin{bmatrix} \bar{d}_1 & \bar{c'}_2 & \bar{\mu}_3 \end{bmatrix} + \det\begin{bmatrix} \bar{d}_1 & \bar{\delta'}_2 & \bar{d}_3 \end{bmatrix} \tag{B.20f}$$

$$n_2' = \det\begin{bmatrix} \bar{d}_1 & \bar{c'}_2 & \bar{d}_3 \end{bmatrix} \tag{B.20g}$$

Since this function is dependent on both Y_1 and Z_1, it requires information on either C (B.13) or L (B.16). This offers some flexibility in the design, and depending on the application, may incorporate a much larger inductance. In addition, it is apparent that all of these expressions are transcendental in nature, and cannot be used to calculate the resulting frequencies for a given reactive loading scheme. They can, however, be numerically inverted to evaluate the frequencies that would result from a specified reactive loading.

Alternate Loading Schemes

The analysis performed here requires a uniform loading on each inductor element. Without this uniformity, it becomes much more difficult to evaluate the necessary loading. The underlying loading matrix ($[Z_{se}']$ or $[Y_{sh}']$) can be modified if an asymmetric loading distribution

is desired, but this is outside the scope of this work. In addition to a asymmetric loading, an arbitrary loading matrix can be incorporated at each reactive region. To analyze the effect of such a matrix, the analysis of Section B.10 is more appropriate as it can be more easily modified for an abitrary load matrix.

The same process can be applied to the analysis of Section B.10 in the case where series capacitors are placed in both ground arms of the CPW medium. This does, however, result in a quadratic expression for (B.12) with two possible values for C. The solutions correspond to low frequency Γ-points of the CSL-like and CPW-like modes, which overlap when the capacitor is placed in the CPW stripline. In the case where series capacitors are attached to **each** conductor of the CPW, (B.12) will be a third order polynomial with three possible solutions. Two of these are again related to the low frequency Γ-points of the CSL-like and CPW-like modes, while the third is related to the cut-off frequency of the MS-like mode. This configuration has been discussed in [3].

B.3 Procedure for determining the loading values

The abovementioned equations, while powerful, may be non-intuitive to an unfamiliar designer of the MTM-EBG in how to actually design the necessary reactive loading. Therefore, a design procedure that is applicable to a fully printed MTM-EBG is provided here.

Step #1 **Determine the host medium RLGC parameters:** As mentioned earlier in this Appendix, the complexity of the host medium of the MTM-EBG makes it more practical to numerically calculate the underlying host medium.

Step #2 **Selecting f_X and f_Γ:** To a reasonable degree, the bandgap edge frequencies are well approximated by f_X and f_Γ. As such, a desired center frequency and bandgap can be used to calculate f_X and f_Γ.

Step #3 **Calculating the capacitance:** The capacitance is calculated first from (B.12) and (B.13), under the condition that $f_{2,3} = f_\Gamma$. (B.15) could be used to calculate L under the same frequency condition, but requires additional evaluation to ensure that the bandgap is properly defined and generally requires much larger inductance than can be realized with a single ribboon inductor.

Step #4 **Calculating the inductance:** First, it should be recognized that $f_X = f_1$, implying that the inductance can be calculated from (B.20a). The capacitance calculated in Step #3 is used here to calculate L by first calculating the reactance of C at f_X as:

$$Z_X = \frac{1}{4j\pi f_X C} \tag{B.21}$$

This can then be substituted into (B.20a) to solve for the admittance of the inductance $Y_X^{(\pm)}$ as follows:

$$Y_X^{(\pm)} = \frac{-(m_2 + Z_X m_2') \pm \sqrt{(m_2 + Z_X m_2')^2 - 4(l_2 + Z_X l_2')(n_2 + Z_X n_2')}}{2(l_2 + Z_X l_2')} \tag{B.22}$$

The coefficients l_2, l_2', m_2, m_2', n_2 and n_2' are defined earlier, where the individual matrices are again calculated about f_X. From (B.22), it is clear that there are two possible solutions. Generally, however, only $Y_X^{(-)}$ represents a valid solution as $Y_X^{(+)}$ typically requires a negative inductance.

$$L = -\frac{1}{4\pi f_X \mathrm{Im}\left(Y_X^{(-)}\right)} \tag{B.23}$$

Appendix C

Studies on the poor passband performance of a four cell MTM-EBG-based filter

In Chapter 2, Section 2.3.2 it was shown that when four identical unit cells were cascaded, the location of the return loss minimas in the passband were strongly related to the total structure rather than a property of the individual unit cells. To further validate this claim consider the four cell case shown in Fig. C.1(a); this is the same configuration that was discussed in Chapter 2, Section 2.3.2. As the length of the unit cells are changed, the position of the reflection zeros (star markers) changes as well; this is shown in Fig. C.1(b). Comparing the phase at these points in Fig C.1(c), it is clear that far from the bandgap the minima correspond to half-wavelength resonances of the *total structural length*, rather than a periodic effects introduced by the dispersion of the MTM-EBG.

Near the bandgap, however, they do not follow such a rule and these minima typically indicate the presence of a substantial mismatch. This limits the applicability of the MTM-EBG as a constituent filter element. To determine the source of this mismatch, surface current profiles of the MTM-EBG were extracted from HFSS at the locations of the square markers in Fig. C.1(b). The resulting profiles are shown in Figs. C.2(a) and C.2(b). It is clear that this current distribution could not arise from a pure MS-like mode as the currents on the CPW ground conductors are contradirected from the currents on the CPW stripline,

suggesting that some portion of this mismatch is due to a contribution from the CPW-like mode. Consider the dispersion diagram corresponding to this unit cell which is shown in Fig. C.3. Very near the edges of the bandgap, where these mismatched frequencies occur, the CPW-like field components are only very weakly attenuated. As such, in the case where there are only a finite number of unit cells it is possible that the CPW-like mode would propagate weakly propagate through the filter. This supports the notion that the source of this mismatch is related to this secondary mode; it cannot be mode-matched to improve this mismatch without sacrificing performance of the MS-like mode.

C.1 Parametric Studies

To resolve this mismatch inspiration was taken from conventional filter theory. For an optimally flat fourth order filter, the loading elements are not identical [92]; they are "mirrored"

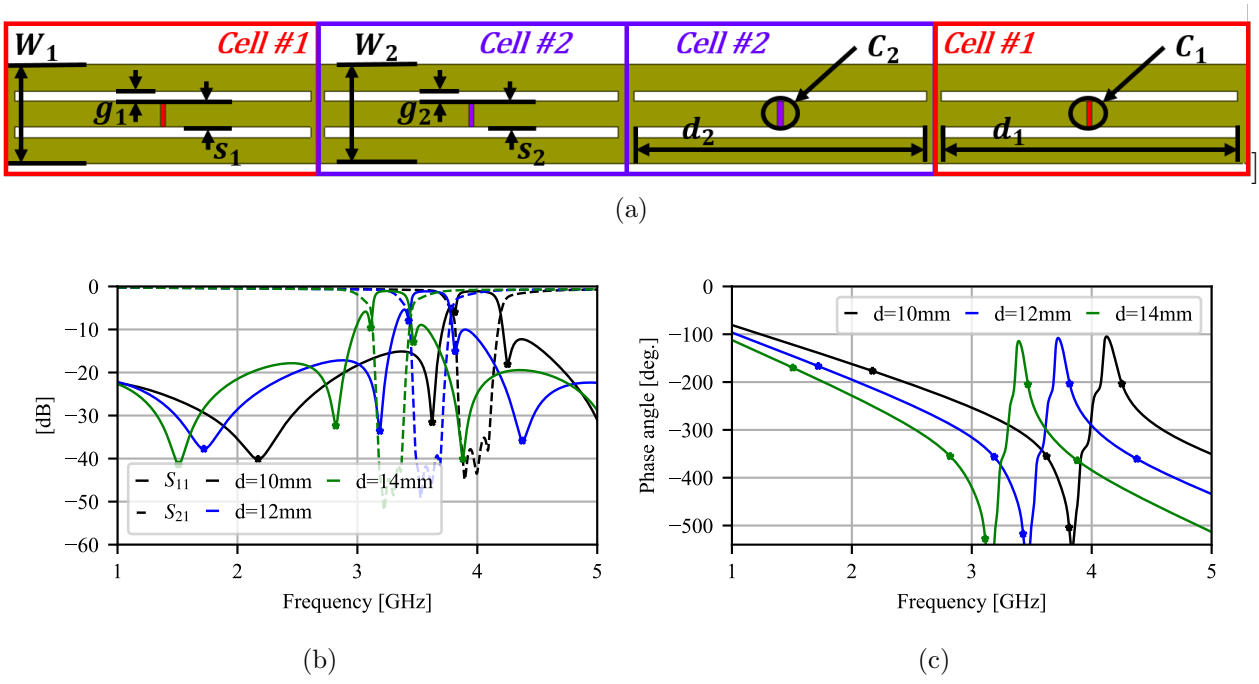

Figure C.1: a) Four unit cell layout with discrete lumped capacitors where the inner and outer unit cells are permitted to be different. b) Magnitude response for **symmetrically** varying the lengths of the unit cells and c) de-embedded transmission phase of the four unit cells. The markers indicate the location of the reflection zeros.

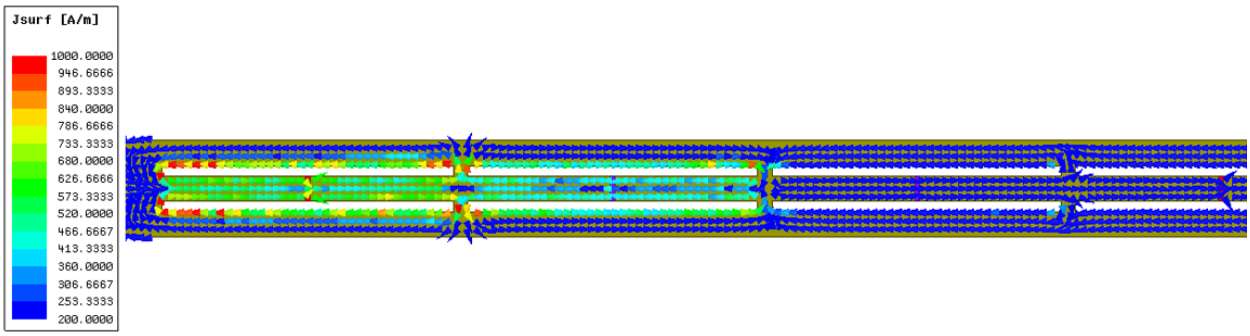

(a)

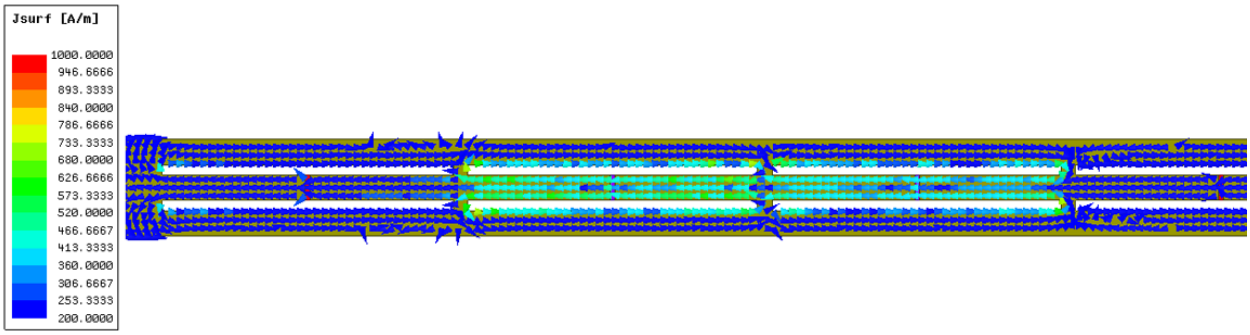

(b)

Figure C.2: Surface current vector plots showing the current distribution at: a) 3.44 GHz and b) 3.81 GHz.

Table C.1: Base parameters used to examine the filter properties.

s_1 / s_2	g_1 / g_2	W_1 / W_2	d_1 / d_2	C_1 / C_2	w_i	h	ϵ_r
1.0 mm	0.4 mm	3.8 mm	12 mm	0.35 pF	0.5 mm	1.524 mm	3.0

in such a way that the outer elements differ from the inner elements. The MTM-EBG is not modelled in the same way as a conventional filter so a prototype filter is not used as a starting point, but the effect of similar asymmetry is practical to examine here. Parametric studies were performed on the various parameters of the four cell MTM-EBG shown in Fig. C.1(a). Since these unit cells are designed on the same substrate, the effect of asymmetric permittivity and thickness was not examined. Furthermore, since the inductors on the edges were effectively shorted due to the MS TL input and output lines, the effect of asymmetric inductance was not examined. The base parameters for each unit cell are outlined in Table C.1.

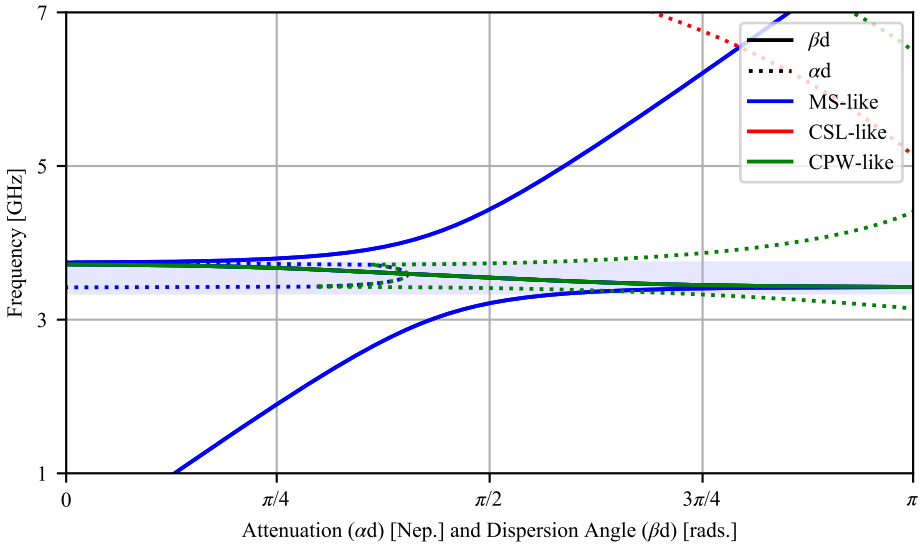

Figure C.3: Dispersion diagram of an MTM-EBG with the capacitor in the CPW stripline.

CPW Stripline width

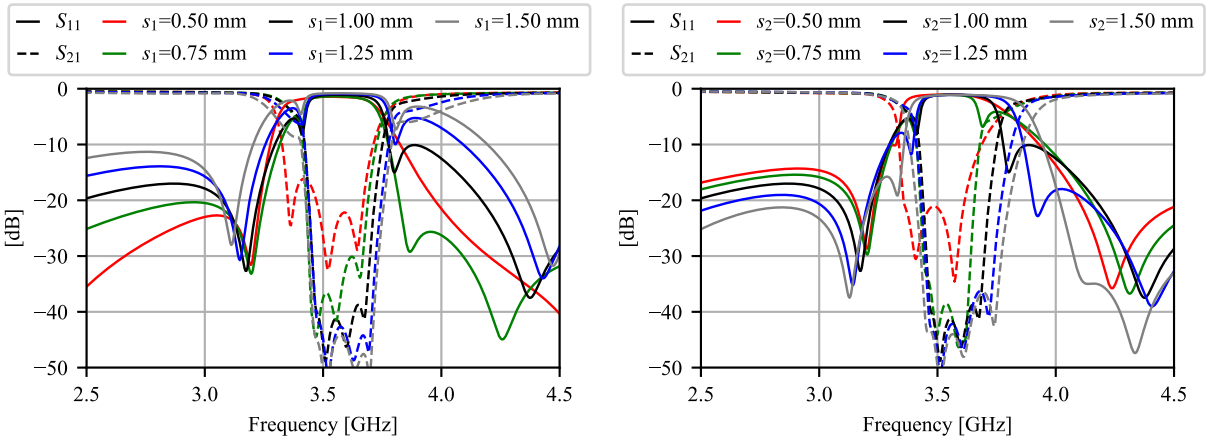

(a) (b)

Figure C.4: Effect of asymmetrically varying the CPW stripline width s for: a) Cell #1 and b) Cell #2.

The first parametric examined was the effect of the CPW stripline widths of cell #1 (s_1) and #2 (s_2)respectively; these results are provided in Figs. C.4(a) and C.4(a). Changing only s_1 has a pronounced effect on the overall passband performance of the filter and improves the total passband for smaller values of s_1. However, these changes do not affect the location of

the minimas near the bandgap and has a relavitely minor effect on their levels. Similarly, the bandwidth is generally weakly affected by increasing s_1; a large decrease in s_1 compared to s_2, however, will increase the rejection band. Changing only s_2, however, shifts the location of these minima as well as there levels. An increase in s_2 increases the return loss on the lower edge of the rejection band, while decreasing it on the upper edge; the opposite is true as well. The bandwidth increases by a small margin for increasing s_2 but this is expected based on the parametric studies in Appendix A.

CPW gap width

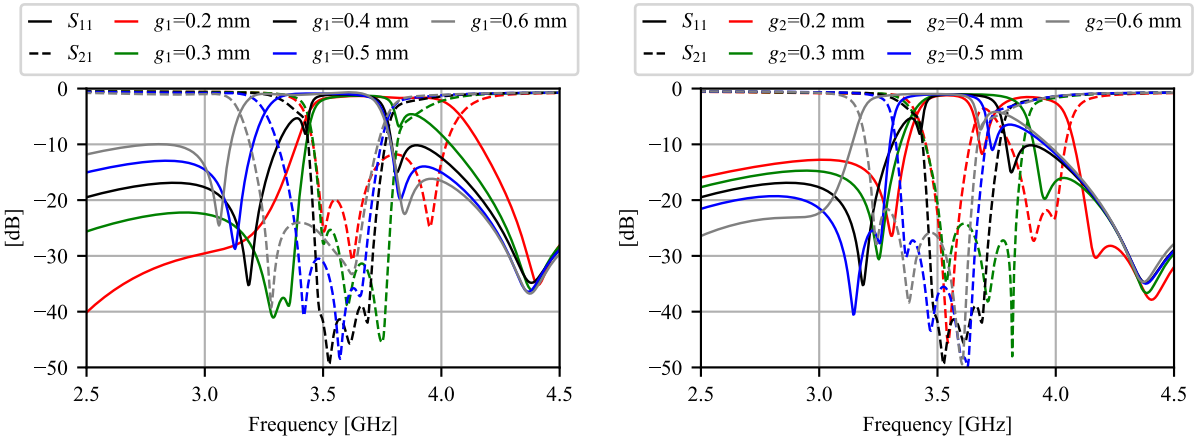

(a) (b)

Figure C.5: Effect of asymmetrically varying the CPW gap width g for: a) Cell #1 and b) Cell #2.

The effect of the CPW gap width g_1 and g_2 were examined next and are provided in Figs. C.5(a) and C.5(b). Increasing g_1 increases the return loss of the upper band-edge, but causes the entire band to shift down in frequency and degrades the performance below the rejection band. Changes in g_2 are more pronounced as any divergence from the nominal values can cause the rejection band to split into multiple smaller bands. This is largely attributed to the fact that changes in the gap width g have a relatively strong effect on the

center frequency of the rejection band. Such a sensitivity was not as pronounced for changes in g_1 because the outer cells are best viewed as individual unit cells whose magnitudes are expected to differ from the predicted dispersion.

CPW total width

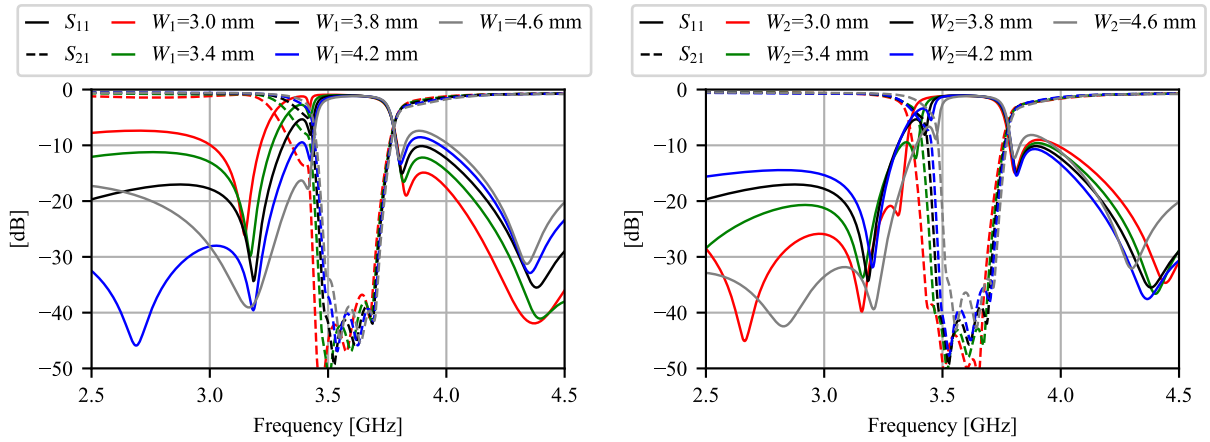

(a) (b)

Figure C.6: Effect of asymmetrically varying the CPW width W for: a) Cell #1 and b) Cell #2.

Changes in both W_1 and W_2 have relatively minor effects on the performance near the rejection band, but have a more pronounced effect on the general passband; these results are shown in Figs. C.6(a) and C.6(b). Increasing W_1 generally increases the return loss of the passband below the rejection band while increasing it above. Increasing W_2, however, has almost no effect on the passband above the rejection band. It does have a more pronounced effect on the passband return loss near the lower edge of the rejection band.

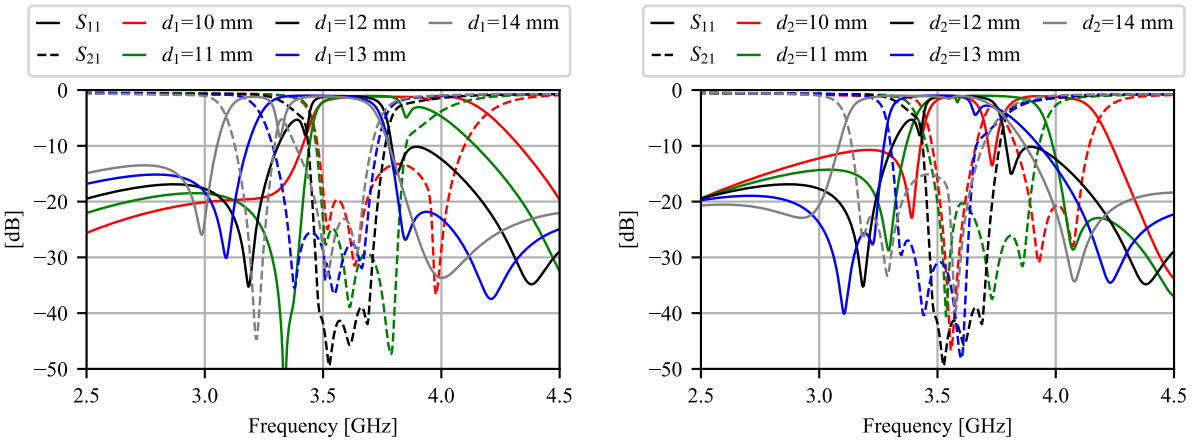

(a) (b)

Figure C.7: Effect of asymmetrically varying the unit cell length d for: a) Cell #1 and b) Cell #2.

Unit Cell Length

Based on the parametric studies provided in Figs. C.7(a) and C.7(b), the length d of the unit cell is an unreliable parameter to change to attempt to improve the passband performance. Even slight changes in either d_1 and d_2 can introduce significant changes in both the rejection band and the passband.

Series Capacitance

While both the capacitance C and the length d alter the center frequency of the bandgap, changes in capacitance are far more beneficial to the passband response of a finite cascade. As demonstrated in Figs. C.8(a) and C.8(b), small changes in the capacitance can have a substantial effect on the performance of the filter. If C_1 is increased, the return loss on the lower band-edge will decrease and it will increase on the upper band-edge. Changes in C_1 have a slight effect on the overall bandwidth, but don't drastically affect the location of the

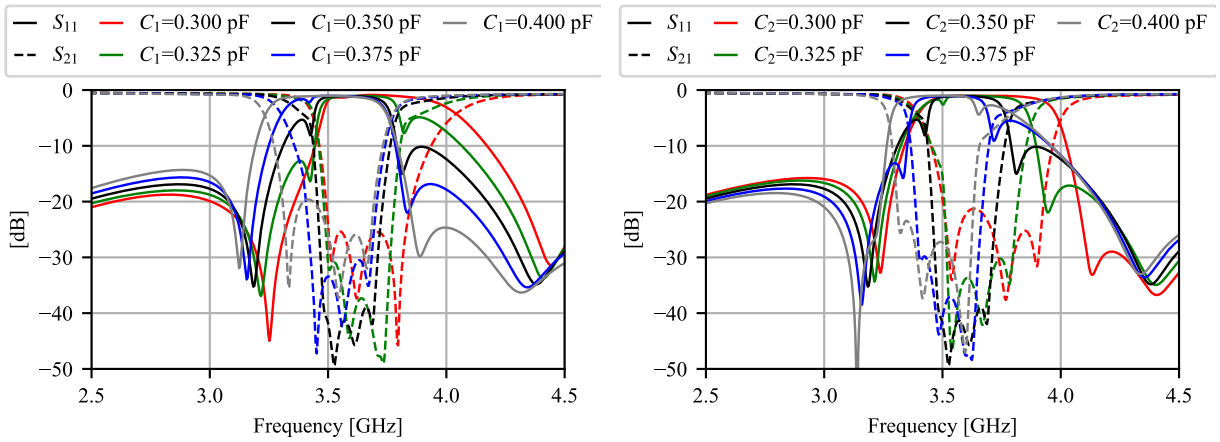

(a) (b)

Figure C.8: Effect of asymmetrically varying the unit cell capacitance C for: a) Cell #1 and b) Cell #2.

minima closest to the bandgap. However, changes in C_2 have a more pronounced effect on the locations of these minima and the size of the bandgap. Increasing C_2 has the return loss of the lower band-edge to decrease, but also causes the minima to be down-shifted. It has a more pronounced effect on the upper band-edge, and increasing C_2 causes the return loss of the upper band-edge to increase; a similar downshift of the minima can be observed.